

Two-Dimensional Infrared Vibrational Echo Spectroscopy Measurements of the  
Structural Dynamics Occurring in Conducting Polymer Thin Films

A DISSERTATION  
SUBMITTED TO THE FACULTY OF THE GRADUATE SCHOOL  
OF THE UNIVERSITY OF MINNESOTA  
BY

Audrey Ann Eigner

IN PARTIAL FULFILLMENT OF THE REQUIREMENTS  
FOR THE DEGREE OF  
DOCTOR OF PHILOSOPHY

Professor Aaron M. Massari, Advisor

September 2011

© Audrey Ann Eigner 2011

## Acknowledgements

Acknowledgments for the individual works presented in this thesis are given at the end of each chapter. Here, I thank the people who have helped me reach the end of graduate school. First, I would like to thank the most important people in my life who always have and always will support me; my family and friends. In particular, I thank my parents, my sister, the extended Eigner family, the Lindstedts, the Palmburgs, and the Biddles. Second, I would like to say thank you to all of my teachers. From grade school I would like to say thanks to Mrs. Rifken (kindergarten) for inspiring me to love learning, Mrs. Benson (4<sup>th</sup> grade) for being able to calm me as an anxious child, Mr. Souer (7<sup>th</sup> grade science) for always choosing me to participate in extracurricular science events, Mr. Anderson (HS physics) for being the best physics teacher this world has ever seen, and Mr. Bergentine (HS chemistry) for giving me my first lessons in chemistry. From my time as an undergraduate I would like to recognize the entire University of Wisconsin – Eau Claire Chemistry Department for having an exceptional and respected chemistry program. Special thanks are given to Professor Allan Gengenbach for recommending me for summer research, and a huge thanks to Professor James Phillips for being the best advisor and mentor anyone could ever ask for. Finally, many thanks are given to my graduate school advisor Professor Aaron Massari. When I started we had an empty laser lab and now we have a full lab with four exceptional graduate students, one brilliant postdoc, numerous undergraduates, several publications, and one cover article. We did great.

**Dedication**

To my parents, Alan and Ellen, and my sister Jeanne.

## **Abstract**

The research presented in this thesis is concerned with the elucidation of the origin of structural dynamics and their relationship to charge mobility in conducting polymer systems. In the past thirty years, research in the field of electrically conducting polymers has grown immensely. Interest in such polymers is due mainly to their unique semiconducting properties and thus their potential application in plastic electronics. While it is known that the charge transport of such polymers is linked to their molecular structure, very little is known about the relationship between charge transport and structural dynamics. In particular, this work has focused on the conducting polymers poly(3-hexylthiophene) (P3HT) and polyaniline (PANI). Samples of each polymer were studied using two-dimensional infrared vibrational echo spectroscopy (2D-IR VES), as well as one-dimensional infrared, UV-visible, and fluorescence spectroscopies. Additional characterizations of the polymers were performed, and included transmission electron microscopy (TEM), hole-mobility and resistance measurements. The vibrational echo technique was especially well suited for this study because it removed inhomogeneous broadening and allowed for the monitoring of the time evolution of molecular structure on the picosecond time scale. Viewed together, the studies presented in this work have begun to correlate specific structural dynamics with changes in the film conductivities.

	iv
<b>Table of Contents</b>	
<b>ACKNOWLEDGEMENTS</b>	<b>i</b>
<b>DEDICATION</b>	<b>ii</b>
<b>ABSTRACT</b>	<b>iii</b>
<b>TABLE OF CONTENTS</b>	<b>iv</b>
<b>LIST OF TABLES</b>	<b>ix</b>
<b>LIST OF FIGURES</b>	<b>x</b>
<b>LIST OF ABBREVIATION</b>	<b>xiv</b>
<b>1. Introduction .....</b>	<b>1</b>
1.1. Research Motivation .....	2
1.2. Charge Transport in Organic Semiconductors .....	4
1.2.1. Variables that Affect Charge Mobility .....	4
1.2.2. Charge Mobility and Thermal Motions .....	7
1.3. Two-Dimensional Infrared Vibrational Echo Spectroscopy .....	11
1.3.1. Brief History and Applications .....	11
1.3.2. Origin of the Vibrational Echo .....	14
1.3.3. Analysis of Homodyne Detected Vibrational Echo Decays .....	17
1.3.4. Experimental Setup of 2D-IR VES .....	22
1.4. Thesis Synopsis .....	25
<b>2. Infrared Spectroscopic Signatures of Phase Segregation in P3HT- Porphyrin Blends .....</b>	<b>27</b>
2.1. Chapter Summary.....	28
2.2. Introduction .....	29

	v
2.3. Experimental .....	31
2.3.1. Materials .....	31
2.3.2. FTIR of Porphyrins in Solution .....	31
2.3.3. FTIR of RuOEP Concentration in P3HT Films .....	31
2.3.4. FTIR of P3OT and P3DDT blends with RuOEP observed over time	32
2.3.5. FTIR Annealing Studies of P3HT-RuOEP blended films .....	33
2.3.6. UV-visible spectroscopy of annealed and unannealed P3HT-RuOEP films .....	33
2.3.7. TEM of annealed and unannealed P3HT-RuOEP .....	34
2.3.8. Fluorescence Spectroscopy of P3HT-RuOEP films .....	34
2.3.9. FTIR of P3HT-RuOEP with pyridine .....	34
2.4. Results and Discussion .....	35
2.4.1. Porphyrin Aggregation in Solution and Thin Films .....	35
2.4.2. Evolution of Blended Films Observed Over Time .....	37
2.4.3. FTIR of Solvent Annealed P3HT RuOEP Films .....	39
2.4.4. UVvis of Solvent Annealed P3HT RuOEP Films .....	46
2.4.5. TEM of Solvent Annealed P3HT RuOEP Films .....	48
2.4.6. Fluorescence Spectra of Solvent Annealed P3HT and RuOEP:P3HT blends .....	50
2.4.7. Model for Phase Segregation in Solvent Annealed P3HT RuOEP Films .....	53
2.5. Conclusions .....	59
<b>3. 2D-IR Studies of Annealing-Induced Changes to Structural Dynamics in     Organic Semiconductor Thin Films .....</b>	<b>61</b>

	vi
3.1. Chapter Summary .....	62
3.2. Introduction .....	63
3.3. Experimental .....	65
3.3.1. Materials .....	65
3.3.2. Thin Film Preparation .....	65
3.3.3. Field-effect Mobility Measurements .....	66
3.3.4. 2D-IR VES .....	67
3.3.5. Pump-Probe Spectra .....	69
3.4. Results and Discussion .....	70
3.4.1. Characterization of Annealed States .....	70
3.4.2. Mobility of Annealed States .....	73
3.4.3. 2D-IR VES of Unannealed and Half-Annealed States .....	76
3.4.4. Pump-Probe Spectra of RuOEP in Different Solvents .....	81
3.4.5. Frequency-Frequency Correlation Function .....	82
3.4.6. Evaluation of FFCF Fits .....	87
3.4.7. Rationalization for Observed Vibrational Dynamics and Mobility	90
3.5. Conclusions .....	91
<b>4. Ground-State Structural Dynamics in Doped and Undoped Polyaniline     Films Probed by 2D-IR Vibrational Echo Spectroscopy .....</b>	<b>93</b>
4.1. Chapter Summary.....	94
4.2. Introduction .....	95
4.3. Experimental .....	97
4.3.1. Materials .....	97



	vii
4.3.2. Preparation of undoped PANI-EB films .....	97
4.3.3. Preparation of DNNSA doped PANI-ES films .....	97
4.3.4. Preparation of CSA doped PANI-ES films .....	98
4.3.5. 2D-IR VES .....	98
4.4. Results and Discussion .....	99
4.4.1. UV-vis of PANI-EB and PANI-ES with and without RuOEP .....	99
4.4.2. FTIR of PANI-EB and PANI-ES doped with CSA and DNNSA .....	101
4.4.3. 2D-IR VES of PANI-EB and PANI-ES doped with CSA and DNNSA .....	104
4.4.4. Description of FFCF Parameters .....	110
4.4.5. Collective Interpretation of Results .....	112
4.5. Conclusions .....	117
<b>5. Static and Dynamic Structural Memory in Polyaniline Thin Films .....</b>	<b>119</b>
5.1. Chapter Summary.....	120
5.2. Introduction .....	121
5.3. Experimental .....	124
5.3.1. Materials .....	124
5.3.2. Preparation of PANI-ES films doped with CSA .....	124
5.3.3. Dedoping of PANI-ES films to PANI-EB with NH <sub>3</sub> gas .....	125
5.3.4. Recovering PANI-ES films .....	125
5.3.5. Resistance Measurements .....	125
5.3.6. Linear Spectroscopy .....	126
5.3.7. 2D-IR VES .....	126

	viii
5.4. Results and Discussion .....	126
5.4.1. UV-vis of thin films during treatment cycle .....	126
5.4.2. FTIR of thin films during treatment cycle .....	129
5.4.3. 2D-IR VES of thin films during treatment cycle .....	134
5.4.4. Transient grating measurements .....	143
5.4.5. Description of FFCF parameters .....	145
5.4.6. Characterization of resistances during treatment cycle .....	150
5.4.7. Collective interpretation of results .....	151
5.5. Conclusions .....	152
<b>Bibliography .....</b>	<b>154</b>

**List of Tables**

2.1. Gaussian parameters determined to fit FTIR spectra of annealed films	42
3.1. FFCF parameters used to fit 2D-IR VES data of P3HT:RuOEP films at two unique annealed states	84
4.1. FFCF parameters used to fit 2D-IR VES data of PANI-EB and PANI-ES films doped with CSA and DNNSA	111
5.1. FFCF parameters used to fit 2D-IR VES data of PANI-ES films doped with CSA throughout a treatment cycle with ammonia gas	147

**List of Figures**

1.1. Double sided Feynman diagrams for non-linear third order experiments	18
1.2. Schematic diagram of the 2D-IR VES optics setup	23
2.1. FTIR Spectra of the CO symmetric stretching vibration for RuTPP and RuOEP in unfiltered and filtered solutions	36
2.2. FTIR Spectra of RuOEP in blended films of RuOEP:P3HT with different weight ratios	37
2.3. FTIR Spectra of RuOEP in (A) P3HT, (B) P3OT and (C) P3DDT observed over time	38
2.4. Successive FTIR spectra for a 1:10 weight ratio RuOEP:P3HT film during annealing in saturated chloroform vapor	40
2.5. Fitted FTIR spectra overlaid with actual data from Figure 2.4.	43
2.6. (A) Calculated spectra of a 1:10 RuOEP:P3HT blended sample determined by fitting the spectra in Figure 2.4. (B) Integrated absorbances for the components of the spectra of Figure 2.4 as function of annealing time	45
2.7. (A) UV-visible spectra of the Soret region of RuOEP in a 1:10 RuOEP:P3HT film for unannealed, half annealed, fully annealed. (B) FTIR spectra of CO stretching region for the samples analyzed in Figure 2.7A. (C) Full range absorption spectra of a 1:10 RuOEP:P3HT film with progressive annealing in solvent vapors	47
2.8. TEM images of (A) a P3HT film unannealed, (B) a P3HT film annealed, (C) a 1:50 RuOEP:P3HT film unannealed, (D) a 1:50 RuOEP:P3HT film annealed, (E) a 1:10 RuOEP:P3HT film unannealed, (F) a 1:10 RuOEP:P3HT film annealed, (G) a 1:5 RuOEP:P3HT film unannealed, and (H) a 1:5 RuOEP:P3HT film annealed	49
2.9. Normalized and baselined FTIR spectra of a 1 to 50 RuOEP to P3HT film before and after solvent vapor annealing for one hour	50
2.10. (A) Fluorescence spectra of a P3HT film and a 1:10 weight ratio RuOEP:P3HT blended film at three annealing stages. (B) Normalized fluorescence spectra from Figure 2.9A	52
2.11. Energy diagram showing splitting of excited states as a result of dipole coupling for (A) parallel and (B) head-to-tail interaction	53

2.12. Schematic diagram showing the proposed arrangement of RuOEP molecules leading to observed spectral changes during annealing in solvent vapors	54
2.13. (A) FTIR showing the CO symmetric stretching region and (B) UV-visible spectra showing the Soret band region of a RuOEP:P3HT film compared with a RuOEP:P3HT film with pyridine binding of the porphyrin	56
2.14. FTIR Spectra of a 1:10 weight ratio RuOEP:P3HT film with a 1:7 mole ratio RuOEP: pyridine annealed in chloroform vapors	58
3.1. Baselined FTIR spectra of the CO symmetric stretching mode on RuOEP embedded into P3HT thin films at the unannealed, half annealed and fully annealed stages	70
3.2. TEM images of (A) unannealed, (B) half annealed and (C) fully annealed RuOEP:P3HT films during the solvent vapor annealing process. Also shown, to the left of each image, are the corresponding FTIR spectra taken from these same films	72
3.3. Field-effect hole mobilities extracted in the linear regime for FETs prepared with pure P3HT and RuOEP:P3HT blends	73
3.4. Spectrally resolved 2D-IR VES decays collected for RuOEP:P3HT blends in the (A) unannealed at $1931\text{ cm}^{-1}$ and (B) half annealed state at $1925\text{ cm}^{-1}$	80
3.5. Pump-probe spectra of RuOEP dissolved in thiophene, 3-hexylthiophene and hexanes	81
3.6. Full 1D- and 2D-IR VES data sets for unannealed RuOEP:P3HT	85
3.7. Full 1D- and 2D-IR VES data sets for half annealed RuOEP:P3HT	86
3.8. Calculated change to the goodness of fit (monitored as the percent change in the total residuals squared) for the half annealed RuOEP:P3HT sample	88
4.1. Molecular Structures for PANI-EB, PANI-ES, and dopants	96
4.2. UV-visible spectra of RuOEP in PANI-EB, PANI-ES doped with CSA, and PANI-ES doped with DNNSA. The spectrum for a RuOEP film spin-coated from chloroform is shown as a reference (3). Vertically offset by 0.55 (dashed lines) are the spectra for the three PANI samples without RuOEP for comparison, same color scheme	100

4.3. (A) Baselined and normalized FTIR spectra of the ruthenium-bound CO symmetric stretching vibration in PANI-EB, PANI-ES doped with CSA, and PANI-ES doped with DNNSA. (B) The full range of FTIR spectra for these three materials	103
4.4. Vibrational echo decays collected at $T_w = 0.5$ ps and $T_w = 10$ ps for (A) PANI-EB measured at $1925\text{ cm}^{-1}$ , (B) PANI-ES doped with DNNSA measured at $1935\text{ cm}^{-1}$ and (C) PANI-ES doped with CSA measured at $1925\text{ cm}^{-1}$	105
4.5. Full 1D- and 2D-IR VES data sets for RuOEP in PANI-EB	107
4.6. Full 1D- and 2D-IR VES data sets for RuOEP in PANI-ES doped with DNNSA	108
4.7. Full 1D- and 2D-IR VES data sets for RuOEP in PANI-ES doped with CSA	109
4.8. Structural models of (A) PANI-EB and (B) PANI-ES	113
5.1. Protonation cycle of CSA-doped emeraldine PANI	127
5.2. UV-visible spectra of as-cast CSA-doped PANI-ES, PANI-EB dedoped with $\text{NH}_3$ gas, and recovered PANI-ES	128
5.3. (A) Full scale FTIR spectra of as-cast PANI-ES, $\text{NH}_3$ -dedoped PANI-EB, and recovered PANI-ES. (B) Same spectra as in (A) but focused on the C=C vibrational frequencies, and (C) the RuOEP-bound CO (baselined and normalized)	131
5.4. Full 1D- and 2D-IR VES data sets for RuOEP in as-cast PANI-ES	136
5.5. Full 1D- and 2D-IR VES data sets for RuOEP in PANI-EB	137
5.6. Full 1D- and 2D-IR VES data sets for RuOEP in recovered PANI-ES	138
5.7. Spectrally-resolved vibrational echo decays collected for as-cast PANI-ES, PANI-EB, and recovered PANI-ES measured at the CO vibration center frequencies of $1925$ , $1933$ , and $1940\text{ cm}^{-1}$ , respectively, and at (A) $T_w = 0.5$ ps and (B) $T_w = 10$ ps	139
5.8. 2D-IR VES data at $T_w = 0.5$ (A) and $7.5$ ps (B) from control studies showing vibrational echo decays for samples treated with ambient air and humid then dry air	140
5.9. Vibrational echo peak shifts extracted from the vibrational echo decays for	

	xiii
as-cast PANI-ES, NH <sub>3</sub> -dedoped PANI-EB, and recovered PANI-ES measured at 1925, 1933, and 1940 cm <sup>-1</sup> , respectively	143
5.10. Normalized transient grating decays for the CO vibration in as-cast PANI- ES, NH <sub>3</sub> -dedoped PANI-ES, and recovered PANI-ES measured at the center FTIR frequencies of 1925, 1933, and 1940 cm <sup>-1</sup> , respectively	145
5.11. Two-point probe sample resistances measured for as-cast PANI-ES, NH <sub>3</sub> - dedoped PANI-EB, and recovered PANI-ES	151

**List of Abbreviations**

<b>2D-IR VES</b>	two-dimensional infrared vibrational echo spectroscopy
<b>2D-NMR</b>	two-dimensional nuclear magnetic resonance
<b>CSA</b>	camphor sulfonic acid
<b>DNNSA</b>	dinonylnaphthalene sulfonic acid
<b>FET</b>	field effect transistor
<b>FFCF</b>	frequency-frequency correlation function
<b>FID</b>	free induction decay
<b>FTIR</b>	Fourier transform infrared
<b>FWHM</b>	full-width half-max
<b>HMDS</b>	hexamethyldisilazane
<b>IR</b>	infrared
<b>NMP</b>	N-methylpyrrolidone
<b>OPA</b>	optical parametric amplification
<b>P3DDT</b>	poly(3-dodecylthiophene-2,5-diyl)
<b>P3HT</b>	poly(3-hexylthiophene-2,5-diyl)
<b>P3OT</b>	poly(3-octylthiophene-2,5-diyl)
<b>PANI</b>	polyaniline
<b>PANI-EB</b>	polyaniline – emeraldine base
<b>PANI-ES</b>	polyaniline – emeraldine salt
<b>PCBM</b>	[6,6]-phenyl-C <sub>61</sub> -butyric-acid-methyl-ester
<b>PPV</b>	poly(paraphenylenevinylene)
<b>RuOEP</b>	2,3,7,8,12,13,17,18-octaethyl-21 <i>H</i> ,23 <i>H</i> -porphine ruthenium(II)carbonyl
<b>RuTPP</b>	5,10,15,20-Tetraphenyl-21 <i>H</i> ,23 <i>H</i> -porphine ruthenium(II) carbonyl
<b>TEM</b>	transmission electron microscopy
<b>UV</b>	ultraviolet-visible
<b>VER</b>	vibrational energy relaxation



# **Chapter 1**

## **Introduction**

## 1.1. Research Motivation

Organic semiconductors are perhaps the most promising materials for advancing current electronic and opto-electronic technologies. With the potential to be light-weight and flexible substances that have properties which can be modified by synthetic modifications,<sup>1-3</sup> blending or doping,<sup>4-7</sup> organic semiconductors are ideal for many applications. Devices such as field effect transistors,<sup>8,9</sup> chemical sensors,<sup>10-12</sup> light emitting diodes<sup>13,14</sup> and solar cells<sup>15-18</sup> are just some of the technologies that incorporate these materials. Besides their novel chemical properties, interest in using organic semiconductors in electronic applications has been driven by the fact that amorphous and semi-crystalline organics are more easily processed than currently used silicon-based materials.<sup>19-21</sup> Unlike inorganic semiconductors, which are held together by networks of covalent bonds, organic semiconductors are composed of individual molecules bound together by much weaker van der Waals forces. As such, many organic semiconductors can be processed at low temperature conditions and with solution phase procedures like spin-casting, dip-coating, and inkjet printing.<sup>19,20</sup>

Among organic semiconductors, polymers have been found to be remarkably successful in terms of processing, but their charge mobilities are much smaller than those required for device applications.<sup>22-24</sup> While some polymeric materials have obtained charge mobilities as high as  $0.5 \text{ cm}^2\text{V}^{-1}\text{s}^{-1}$ , the mobilities of these materials seldom exceed this value.<sup>22-24</sup> Many studies have shown that charge mobilities can be improved substantially with synthetic modifications and post-processing treatments that enhance packing and orbital overlaps,<sup>1-3</sup> however these reports are lacking in that they consider only the stationary arrangement of molecules and disregard the dynamic aspect

of the molecular structures. Even in solid-state films at room temperature, molecular structures twist, buckle, and wag as a result of thermally induced fluctuations. Some recent publications have predicted that molecular motions occurring on time scales similar to charge hopping events could have a significant effect on charge mobilities.<sup>25-31</sup> The femtosecond to picosecond time regime, which corresponds to low frequency vibrations in the 1-400  $\text{cm}^{-1}$  range, are especially important because they coincide with the approximate charge hopping times found in many amorphous and semicrystalline materials.<sup>32-36</sup>

Thus far, the characterization of ultrafast motions in organic systems has been minimal due to the lack of experimental methods with the ability to measure these motions.<sup>37,38</sup> In the early 1990s however, technological developments of laser systems allowed a coherent IR-pulse sequence, which measures the evolution of vibrational states, to be applied to large molecules.<sup>39</sup> This technique is called two-dimensional infrared vibrational echo spectroscopy (2D-IR VES). Similar to two-dimensional nuclear magnetic resonance (2D-NMR), and identical to photon echo experiments (though performed at IR wavelengths), the 2D-IR VES technique uses a coherent pulse sequence to remove inhomogeneous broadening and provide dynamical information that steady-state absorption and fluorescence measurements cannot.<sup>39,40</sup> In addition, because the technique utilizes the IR region of the electromagnetic spectrum, the molecular dynamics can be measured for systems in their electronic ground states with negligible perturbation of their molecular structures.<sup>40-42</sup> The technique itself is performed by probing and observing an IR-active vibrational mode that is either intrinsic to the system of interest,<sup>42-48</sup> or is added to the system with the addition of an

extrinsic molecule.<sup>49-54</sup> In this work, the latter approach was employed, because the polymer systems examined did not provide a sufficiently strong IR-active mode to generate a measurable vibrational echo.

In total, the research presented in this thesis has been performed in an attempt to determine how molecular motions in conducting polymer films correlate with conducting ability. As such, the work has focused on the use of the 2D-IR VES technique to measure the molecular dynamics occurring in thin, solid-state polymer films. The work also incorporated Fourier transform infrared (FTIR), ultraviolet-visible (UV-vis), and fluorescence spectroscopies, as well as transmission electron microscopy (TEM), hole-mobility and resistance measurements. In the next two sections of this chapter (sections 1.2. and 1.3.), information pertaining to charge transport in organic systems as it relates to molecular dynamics and background information on the 2D-IR VES technique are provided. The final section of this chapter (1.4.) gives an outline of what can be found in the remaining chapters of this thesis.

## **1.2. Charge Transport in Organic Semiconductors**

### **1.2.1. Variables that Affect Charge Mobility**

The charge transport properties of a material depend on the electronic structures of each individual molecule in the material and the couplings between these molecules.<sup>8,20,55,56</sup> Together, the electronic structures and couplings determine the potential energy landscape of a material. In order for charge transport to occur, charge carriers must be able to navigate the energy landscape in a material efficiently without being trapped or scattered.<sup>56</sup> Therefore, any variable that can modify the energy landscape, or can provide charge carriers with sufficient energy to overcome barriers

associated with the energy landscape, is capable of influencing charge mobility. As such, there are many different internal and external variables that may affect charge transport properties, including molecular packing,<sup>57-59</sup> disorder,<sup>56</sup> external temperature,<sup>60,61</sup> and charge carrier density.<sup>62</sup>

Charge transport is sensitive to the molecular packing in a material on small length scales (between individual molecules) and on large length scales (across many molecules).<sup>63</sup> On small length scales, molecular packing can be improved with synthetic modifications, or post-processing treatments, that promote higher orbital overlaps. For instance, the charge mobility of regioregular P3HT is several orders of magnitude larger than that of regiorandom P3HT due to an increased ability to align adjacent polymer chains.<sup>64,65</sup> Similarly, increasing the length of side chains on poly(alkylthiophenes), which has been found to improve solubility, increases the interchain spacing resulting in a decrease in mobility.<sup>66</sup> On a larger scale, many organic semi-conducting materials form crystalline and amorphous regions. For high molecular weight P3HT films, the formation of crystalline regions has been found to be less than that in lower molecular weight P3HT films.<sup>67</sup> Interestingly, the higher molecular weight films were found to have larger mobilities, which has been attributed to long polymer chains being able to link the crystalline regions.<sup>68</sup> In Chapters 2 and 3, the effects of molecular packing are examined as blended films of P3HT are annealed in solvent vapors to enhance crystallinity within the film.

Disorder in organic materials can also contribute to the resulting charge transport properties.<sup>56</sup> There are two types of disorder that have been described, diagonal disorder and off-diagonal disorder. Diagonal disorder describes the variations in the

energy levels of individual molecules in a material (site energies). This type of disorder can be caused by torsional defects and polarization effects, which cause a distribution of torsional angles or dipole moments that lead to finite areas with different energies.<sup>56</sup> In contrast, off-diagonal disorder deals with the couplings between molecular units and the differing energies of these interactions. This type of disorder is caused by variations in the relative position of adjacent molecules and their orientations with respect to one another.<sup>56</sup>

Some external factors, such as temperature, can also affect charge transport properties. For disordered organic semiconducting materials, including the ones observed in this thesis, charge hopping dominates the transport mechanism.<sup>8,56</sup> This results in disordered systems having mobilities that are thermally activated.<sup>35</sup> Thus, elevated temperatures lead to increased mobilities as a result of an increased ability of charge carriers to overcome barriers associated with the potential energy landscape of the material. Often, these dependences are fit to an Arrhenius-like law that has been found to reproduce the experimental data well; however there has been no theoretical justification for the use of this type of equation.<sup>56</sup> This is different from organic single crystals, which have mobilities that typically decrease with temperature and are fit well with a power law. In these systems, the temperature dependence is more like that of a system with band transport.

The effects of charge density on charge mobility in organic systems have also been studied. Blom and coworkers have measured the charge mobility for the polymer poly(paraphenylenevinylene) (PPV), and have reported that the mobility in a transistor configuration (high charge density) was  $10^{-4} \text{ cm}^2\text{V}^{-1}\text{s}^{-1}$ , while the mobility in a diode

configuration (low charge density) was  $10^{-7} \text{ cm}^2\text{V}^{-1}\text{s}^{-1}$ .<sup>62</sup> Thus, they found that higher charge densities lead to improved efficiencies. Their explanation for this result considers how charges interact with traps in a material. Every charge carrier is affected by traps at low charge densities, while at higher charge densities only a portion of charge carriers are affected by traps. This occurs because the traps become filled and subsequent charge carriers are able to travel through an essentially trap-free energy landscape.<sup>56,62</sup>

These four examples are just a few of the ways in which charge mobility is affected by internal and external factors. Some additional factors that affect charge mobility include the use of an electric field,<sup>69,70</sup> the presence of chemical impurities,<sup>71,72</sup> the application of external pressure,<sup>73-75</sup> and differences in molecular weight.<sup>67</sup> Understanding how all of these variables work together to determine the charge transport characteristics of a given material is thus an extremely difficult task; however, the potential benefits of these materials are great. In this thesis, the work has focused on understanding how just one variable, molecular dynamics, affects charge mobility. The next two sections will describe how molecular dynamics relate to charge mobility, and why they are potentially very important to the continued improvement of charge mobilities of polymeric materials.

### **1.2.2. Charge Transport and Thermal Motions**

As alluded to in the previous section, charge transport is characterized by the relationship between energies associated with individual molecules and the couplings between different molecular units. These interactions are termed electronic interactions, and they make up half of the interactions that are important to the characterization of

charge transport. The second type of interaction that must be considered in order to characterize charge transport is electron-phonon interactions, also sometimes referred to as electron-vibration interactions.<sup>8,56</sup> These interactions couple charge-displacements to molecular vibrations and have been suggested to be as important, if not more important, than electronic interactions in organic systems.<sup>27,56</sup> For inorganic systems, the contribution of electron-phonon interactions to charge transport is very small and is often neglected.<sup>56</sup> This can be explained by considering the nature of molecular bonds in inorganic versus organic systems. In an inorganic system the bonding between atoms is mainly covalent, where as in an organic system the bonding also consists of many weak van der Waals interactions. This causes the coupling between electronic sites to be more uniform in inorganic systems than it is in organic systems. The larger fluctuation of this coupling in organic materials is due in part to the relatively disordered nature of molecules in organic compared to inorganic systems, but has also been proposed to be a result of thermally activated motions.<sup>35</sup>

To understand how thermal motions modulate the electron-phonon couplings and influence charge transport, it is useful to consider the electronic Hamiltonian that is commonly referenced for charge transport (equation 1.1).<sup>56</sup>

$$H_e = \sum_m \varepsilon_m a_m^\dagger a_m + \sum_{mn} t_{mn} a_m^\dagger a_n \quad (1.1)$$

In this equation,  $a_m^\dagger$  and  $a_m$  are the creation and annihilation operators,  $\varepsilon_m$  is the electron site energy and  $t_{mn}$  is the transfer integral. Here, the modulation of the electron site energy is termed local electron-phonon coupling and the modulation of the transfer integral is termed non-local electron-phonon coupling.<sup>56</sup> Local electron-phonon



coupling describes the coupling of inter- and intra-molecular vibrations to electronic site energies, and results in the localization of charge carriers in the form of a polaron.<sup>76-</sup>

<sup>79</sup> Non-local electron-phonon coupling, on other hand, describes how the transfer integral is affected by the spacing and relative orientation of adjacent molecules.<sup>56</sup> Thus, the transfer integral, which is a measure of wavefunction overlap between two electronic sites, could introduce a time-dependence to carrier mobility as a result of thermal motions.

The total mobility of a system,  $\mu$ , can be expressed as the sum of the mobility originating from electron tunneling and electron hopping (equation 1.2), where the relative contribution of each component to the total mobility depends on the electron-phonon coupling in system.<sup>56,78,80,81</sup>

$$\mu = \mu_{\text{tunneling}} + \mu_{\text{hopping}} \quad (1.2)$$

For weak electron-phonon coupling, as in most inorganic systems, the component originating from tunneling dominates the equation at all temperatures and the mobility follows a power law ( $\mu \approx T^n$ ) that is typical of band-like conduction.<sup>82</sup> For systems with strong electron-phonon coupling, the total mobility behaves differently in different temperature ranges. At low temperatures, the mobility behaves similarly to a system with weak electron-phonon coupling, but as temperature is increased the mobility gradually switches to a regime where hopping dominates and the mobility becomes thermally activated. Finally, at extremely high temperatures, the mobility again begins to decrease with temperature as a result of sufficient thermal energy to dissociate the polaron.<sup>56</sup> Thus, for many organic semiconducting materials near room temperature, the mobility is dominated by hopping.

A commonly cited polaron model for the mobility originating from hopping is based on the Holstein molecular model, which considers both electronic and electron-phonon interactions. Under this model the charge mobility originating from hopping is given in equation 1.3.<sup>8,56</sup>

$$\mu_{\text{hopping}} = \frac{ea^2t^2}{k_B T \hbar \omega_o} \left[ \frac{\pi}{g^2 \operatorname{csc} h(\hbar \omega_o / 2k_B T)} \right]^{1/2} \exp \left[ -2g^2 \tanh \left( \frac{\hbar \omega_o}{4k_B T} \right) \right] \quad (1.3)$$

In this equation,  $e$  is the electronic charge,  $a$  is the typical hopping distance,  $t$  is the transfer intergral,  $k_B$  is Boltzmann's constant,  $T$  is temperature,  $\hbar$  is Plank's constant,  $\omega_o$  is the frequency, and  $g$  is the electron-phonon coupling constant. Here, the mobility becomes time-dependent when molecular dynamics are considered and the transfer integral fluctuates in time. Under these conditions, the potential energy landscape of a system becomes fluid-like as areas of high and low potential fluctuate and rearrange with time. The degree to which thermal motions cause variations in the transfer integral have only just begun to be interpreted.

Troisi and Orlandi have recently evaluated the significance of thermal motions' ability to modify electronic couplings that are relevant for charge transport.<sup>35,83</sup> They have used molecular dynamics simulations, with a one-dimension semiclassical model, to examine the effects of thermal motions on the transfer integral of pentacene and anthracene. They found that the fluctuations of the transfer integral were as large as their average values above 100 K, which implies that carrier transport is in fact dominated by thermal motions in these systems. Coropceanu and coworkers have also examined the time dependent effects of motions on charge transport.<sup>56</sup> This group estimated that a change in the intermolecular spacing between oligoacene derivatives

from 3.4 to 4.0 Å could cause the electronic couplings to vary by a factor of 3 to 4. Some additional studies have also corroborated the dependence of thermal motion and the transfer integral using resonance Raman spectroscopy and steady-state electronic absorption spectroscopy.<sup>84-87</sup> Thus, a story is beginning to develop which links molecular dynamics to charge carrier mobilities. As of yet, the direct measurement of the motions in organic systems has not been performed. This is the goal of the work presented in this thesis, to experimentally measure these dynamics that are seemingly linked to charge transport properties. As previously mentioned, this work has used 2D-IR VES in order to begin to complete this task. The next sections will provide a basis for the use of this technique.

## **1.3. 2D-Infrared Vibrational Echo Spectroscopy**

### **1.3.1. Brief History and Applications**

The use of coherent pulse sequences in scientific experiments was first reported in the 1950s.<sup>39,40</sup> It was at this time that the first NMR experiments were developed to study spin states.<sup>39</sup> Photon echo experiments were developed to study electronic states some ten years later, but vibrational echo experiments were not demonstrated to study vibrational states until much later.<sup>39</sup> In the early 1990s, advancements in optical parametric amplifiers and titanium sapphire lasers allowed vibrational echo measurements to be performed for the first time. Over the next twenty years, continued advancements in laser systems have allowed two-dimensional experiments to be used on a number of systems and with table-top laser systems that provide sub 60 fs infrared pulses.<sup>41</sup> As such, 2D-IR VES has become available to many researchers and has been used to examine a number of different chemical problems and molecular systems.

Over the years, many 2D-IR VES studies have examined the dynamics of water.<sup>41,46,88-96</sup> These studies have used the OH stretching frequency of water to probe hydrogen-bonding dynamics. Researchers have extracted frequency-frequency correlation functions from 2D-IR VES data to measure the evolution of the hydroxyl stretching frequency over time. These functions (which are discussed further in Section 1.3.3) have provided a quantitative view of the hydrogen-bond dynamics in water by following the evolution of the OH frequency over time. For example, Fayer and coworkers have found that the fastest dynamics of water confined to nanoscopic dimensions in reverse micelles are similar to those in bulk water, while the slowest dynamics in these systems are an order of magnitude slower than those found in bulk water.<sup>96</sup> While the fastest dynamics in water are thought to relate to local hydrogen-bond fluctuations, the slowest dynamics are thought to relate to global rearrangements of hydrogen-bond networks.<sup>96</sup> Thus, it was concluded that the confined space of the micelles would affect the slowest dynamics to a larger extent than the fastest dynamics.

Studies of metal carbonyls in solution have also been done by several research groups.<sup>48,97-99</sup> In the 1990s, Fayer and Rector performed a series of studies where they observed pure dephasing of the metal carbonyls  $\text{Rh}(\text{CO})_2\text{acac}$  and  $\text{W}(\text{CO})_6$  in liquid and glassy solvents.<sup>97,100</sup> These studies provided some of the first information about how dynamics in a system can lead to vibrational energy level fluctuations, and hence how vibrational modes can be used to obtain information about surrounding solvent dynamics. More recently, Tokmakoff and coworkers have studied the coupling and orientation of vibrational modes of  $\text{Rh}(\text{CO})_2(\text{C}_5\text{H}_7\text{O}_2)$ ,<sup>99</sup> and Kubarych and coworkers have used  $\text{Mn}_2(\text{CO})_{10}$  as a model system for development of 2D-IR spectra.<sup>48</sup> Thus,

metal carbonyl complexes have continually aided in the development of the 2D-IR techniques, which is due primarily to the fact the complexes having strong CO stretching modes with unique vibrational couplings.

Vibrational echo experiments have also been applied to many biological problems.<sup>40,49,101-104</sup> The technique has been particularly useful for understanding the structure, dynamics and function of proteins on picosecond and femtosecond time scales. In carbonmonoxy heme proteins, like myoglobin and hemoglobin, the CO vibration on the heme has been used as a probe for the structural fluctuations of the protein.<sup>103,105</sup> Zanni and coworkers have also used labeled isotopes to measure the dynamics of amide modes on peptides.<sup>44,106</sup> In this way, they were able to correlate dynamics to distinct portions of membranes and find that the extent of inhomogeneous broadening was dependent on the position of the amide group inside a membrane. Additionally, Hochstrasser and coworkers have studied the structure and dynamics of amyloid fibrils found in the brain tissue of persons with Alzheimer's disease.<sup>104</sup> These studies were useful in characterizing the nature of coupling between the amyloid fibrils and determining the distance between carbonyl modes on backbone of the fibril.

More recently, technological advancements have made it possible for the 2D-IR VES technique be developed for use with chemical exchange reactions including, the formation and dissociation of organic solute-solvent complexes,<sup>107,108</sup> proton transfer reactions,<sup>109</sup> and isomerizations.<sup>110</sup> Unlike the experiments presented in the following chapters of this thesis, which were performed using homodyne detection, chemical exchange studies require the use of heterodyne detection. After the vibrational echo is generated it can either be sent directly through a monochromator for collection

(homodyne) or it can be overlapped with another pulse and then sent for detection (heterodyne). The benefit of heterodyne collection is that it allows the phase information of the vibrational echo to be measured. The interference of the vibrational echo and this additional pulse (referred to as the local oscillator) are observed as a function of time, and are used to create a 2D-IR spectrum that has two frequency axis. One axis is obtained from scanning the vibrational echo signal in a monochromator, and the second axis is obtained from Fourier transform of the interference of the vibrational echo and the local oscillator. The creation of these images then allows one to observe bands that represent the association and dissociation of different chemical species on ultrafast time scales.

### **1.3.2. Origin of the Vibrational Echo**

A 2D-IR VES experiment uses a three-pulse excitation sequence, where the pulse center wavelength is tuned to the vibrational transition of interest, to generate a fourth pulse known as the vibrational echo. Before the excitation pulses interact with a sample, the collection of vibrational oscillators exists in their ground state. When the first pulse interacts with the sample, a sub-ensemble of these oscillators is put into a coherent superposition state of their ground and first excited states. In this superposition state the ground and first excited states are coupled and these oscillators emit. At first, all of the excited oscillators vibrate (or emit) in phase with one another as a macroscopic polarization, but over time this phase relationship is lost. This is because the oscillators vibrate at different frequencies due to the inhomogeneous distribution of their vibrational transition energies, and because of the random frequency fluctuations each oscillator experiences as a result of environmental

perturbations (explanation following). The overall decrease in the macroscopic polarization after the first pulse due to the collective loss of phase relationships and energy relaxation is referred to as the free induction decay (FID).<sup>40</sup> It is important to note that although the macroscopic polarization in the sample has decayed (FID), the microscopic polarizations (superposition states on individual molecules) persist for as long as the vibrational lifetime allows.

The environmental perturbations mentioned above can be explained by the vibrational Stark effect, which is observed when a vibrational frequency of an oscillator changes in the presence of an electric field.<sup>111</sup> Because each solvent or solute molecule can be associated with a small or large electric dipole due to partial charges on their atoms, local net electric fields are created throughout the sample. These local net electric fields are subject to change with the motion of the molecules and their dipoles. Thus, as the projection of the net electric field vector onto the transition dipole of the IR oscillator varies, the vibrational frequency of the oscillator changes through a time-dependent version of the Stark effect. In the proposed studies, the environmental fluctuations “sensed” by a given oscillator can be caused by the polymer backbone that it is attached to, or by a nearby polymer chain or residual solvent molecule.

After a time  $\tau$ , the second pulse interacts with the sample. This second pulse removes the coherent superposition state and generates a population in either the ground state or the first excited state. In the population state, the ground and first excited states of the oscillator are no longer coupled by an oscillating dipole moment and the oscillators do not emit coherently. The second pulse therefore stops the free induction decay by removing the connection between the ground and first excited states. In this

way, the phase information of the oscillators, generated by the first pulse, is stored until the third pulse interacts with the sample.<sup>112</sup> The time period between the second and third pulses is therefore called the time waiting period and is given the symbol  $T_w$ . During this period, the vibrational energy levels of the oscillators continue to change with the thermal fluctuations of their environment. Therefore, the phase relationships that were stored by the second pulse are not stored indefinitely, and the average frequency of a given ensemble of oscillators will wander during the  $T_w$  period, an effect referred to as spectral diffusion.<sup>40</sup> During this waiting period, spectral diffusion as well as the vibrational lifetime affects the intensity of the vibrational echo pulse.

When the third pulse interacts with the sample, the oscillators are excited into the phase conjugate of the original superposition state. This action begins a rephasing process, such that the oscillators vibrate (or emit) in phase with each other at a time approximately equal to  $\tau$ . At the point of maximum rephasing, a macroscopic polarization is regenerated and the vibrational echo pulse becomes measurable. This final evolution period after the third pulse is termed the  $t_3$  period, and the oscillators that have been placed in a new superposition state are once again sensitive to the random dephasing processes that erased the phase relationships during the  $\tau$  period. It is at this point that the inhomogeneity of the oscillators' frequencies has been removed, since the intensity of the vibrational echo was not affected by the distribution of frequencies. The intensity of the vibrational echo is, however, decreased by dephasing (during the  $\tau$  and  $t_{\text{echo}}$  periods), spectral diffusion (during the  $T_w$  period), and the vibrational lifetime (during all periods). The longer the collection of oscillators is exposed to the random environmental perturbations, the more their relative phases are affected, and the less



they are able to re-phase. The intensity of the vibrational echo pulse, therefore, decays as a function of both  $\tau$  and  $T_w$ . In a typical homodyne detected experiment,  $T_w$  is held fixed at several values while  $\tau$  is scanned to obtain a series of plots that show the growth and decay of the vibrational echo signal. These plots are referred to as vibrational echo decays. The following section will describe the evaluation of the vibrational echo decays and how they are used to extract the molecular dynamics of a chemical system.

### 1.3.3. Analysis of Homodyne Detected Vibrational Echo Decays

The quantifier that describes all spectroscopic dynamics is the frequency-frequency correlation function (FFCF),  $C(t)$ .<sup>113</sup> A commonly used functional form of the FFCF in 2D-IR fitting is a multi-exponential plus a constant:<sup>114,115</sup>

$$C(t) = \Delta_0^2 + \sum_{i=1}^n \Delta_i^2 e^{-\frac{t}{\tau_i}} \quad (1.4)$$

where  $\Delta_0$  represents the contribution from inhomogeneous and quasi-inhomogeneous broadening and  $\Delta_i$  is the magnitude of a frequency changing process that occurs with a time constant of  $\tau_i$ . This functional form enables the dynamics sampled to be categorized into several time scale components for comparison from sample to sample. The typical process of obtaining the FFCF from a series of vibrational echo decay curves (collected at several  $T_w$ s and several frequencies across the inhomogeneous lineshape) is to numerically calculate the echo decay from a starting FFCF, compare to the experimental decays, and iteratively vary the parameters of the FFCF to best reproduce the experimental data at all  $T_w$ s and all frequencies, plus the linear lineshape simultaneously.

Calculation of the vibrational echo decay from  $C(t)$  begins with the following equation for the lineshape function,  $g(t)$ .<sup>114,115</sup>

$$g(t) = \int_0^\tau dt' \int_0^{\tau'} dt'' C(t) \quad (1.5)$$

The lineshape function is in turn used to determine the third order response functions,  $R_n$ , which describe how an ensemble of oscillators behaves when subjected the varying quantum pathways probed with pulses of IR light in these experiments.

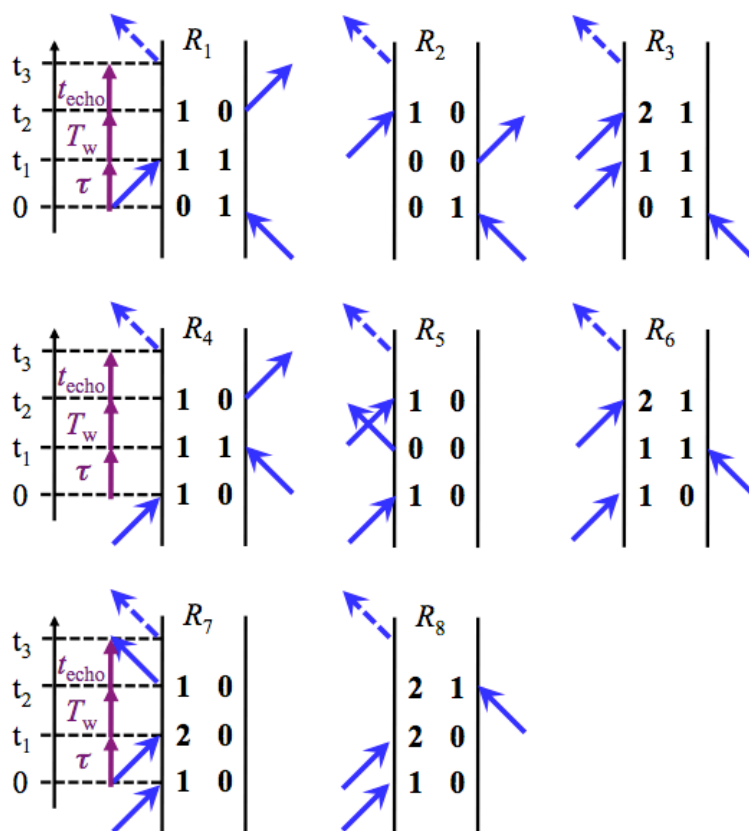


Figure 1.1: Double sided Feynman diagrams for non-linear third order experiments.

The relevant pathways can be summarized in condensed form by Feynman diagrams (Figure 1.1), which schematically represent the pathways of states that an ensemble of oscillators may take with each pulse interaction. For the three-pulse sequence used in this work, the first, second, and third pulses are ascribed the wavevectors,  $k_1$ ,  $k_2$ , and  $k_3$ , respectively. In the Feynman diagrams, a positive  $k$ -vector appears as an arrow pointing to the right, a negative  $k$ -vector is an arrow pointing to the left, an arrow into the system (raising a ket or bra in the density matrix) is an absorptive interaction with a pulse, and an arrow away from the system (lowering a ket or bra in a density matrix) is emissive. The eight diagrams shown represent the pathways that were used in the calculations to fit the data since they lead to signal generation in the phase-matched direction,  $k_s = -k_1 + k_2 + k_3$ . Of these eight diagrams, three represent rephasing pathways ( $R_1$ - $R_3$ ), corresponding to pulse orderings of  $-k_1, +k_2, +k_3$  and  $-k_1, +k_3, +k_2$  (note that the negative  $k$ -vector in these three diagrams is always the first interaction). In the rephasing diagrams, the third pulse prepares the phase conjugate of the original (or anharmonically shifted) coherence. The remaining five diagrams represent non-rephasing processes ( $R_4$ - $R_8$ ), where the third pulse prepares the original (or anharmonically shifted) coherence and continues the free induction decay initiated by the first interaction. The response functions  $R_4$ - $R_6$  correspond to the pulse orderings in which the negative  $k$ -vector is the second interaction ( $+k_2, -k_1, +k_3$  and  $+k_3, -k_1, +k_2$ ), and  $R_7$ - $R_8$  correspond to the orderings in which the  $-k_1$  is the final interaction ( $+k_3, +k_2, -k_1$  and  $+k_2, +k_3, -k_1$ ). In these equations (written out below),  $\mu$  is the transition dipole,  $\omega$  is the frequency of a vibrational transition, and  $\Delta$  is the vibrational anharmonicity. The absolute time variables ( $t_1, t_2, t_3$ ) are converted to the experimental time intervals

between the pulses ( $\tau$ ,  $T_w$ ,  $t_{echo}$ ), as shown graphically in border of the Feynman diagrams above:

$$\tau = t_1 \quad (1.6)$$

$$T_w = t_2 - t_1 \quad (1.7)$$

$$t_{echo} = t_3 - t_2 \quad (1.8)$$

The relevant response functions are:

$$R_1 = R_2 = |\mu_{10}|^4 e^{-i\omega(t_3-t_1)} e^{-g(t_1)+g(t_2)-g(t_3)-g(t_2+t_1)-g(t_3+t_2)+g(t_1+t_2+t_3)} \quad (1.9)$$

$$R_3 = -|\mu_{10}|^2 |\mu_{21}|^2 e^{-i[t_3(\omega_{10}-\Delta)-\omega_{10}t_1]} e^{-g(t_1)+g(t_2)-g(t_3)-g(t_2+t_1)-g(t_3+t_2)+g(t_3+t_2+t_1)} \quad (1.10)$$

$$R_4 = R_5 = |\mu_{10}|^4 e^{-i\omega_{10}(t_3-t_1)} e^{-g(t_1)-g(t_2)-g(t_3)+g(t_2+t_1)+g(t_3+t_2)-g(t_3+t_2+t_1)} \quad (1.11)$$

$$R_6 = -|\mu_{10}|^2 |\mu_{21}|^2 e^{-i[t_3(\omega_{10}-\Delta)+\omega_{10}t_1]} e^{-g(t_1)-g(t_2)-g(t_3)+g(t_2+t_1)+g(t_3+t_2)-g(t_3+t_2+t_1)} \quad (1.12)$$

$$R_7 = |\mu_{10}|^2 |\mu_{21}|^2 e^{-i\omega_{10}(t_3+2t_2+t_1)} e^{i\Delta t_2} e^{g(t_1)-g(t_2)+g(t_3)-g(t_2+t_1)-g(t_3+t_2)-g(t_3+t_2+t_1)} \quad (1.13)$$

$$R_8 = -|\mu_{10}|^2 |\mu_{21}|^2 e^{-i\omega_{10}(t_3+2t_2+t_1)} e^{i\Delta(t_3+t_2)} e^{g(t_1)-g(t_2)+g(t_3)-g(t_2+t_1)-g(t_3+t_2)-g(t_3+t_2+t_1)} \quad (1.14)$$

For fitting the data, the vibrational lifetimes,  $T_1$ , were treated as multiplicative terms to the response functions:

$$\exp\left(\frac{-\tau/2 + T_w + t_{echo}/2}{T_1}\right) \text{ for } R_1, R_2, R_4, R_5, R_7, \text{ \& } R_8 \quad (1.15)$$

$$\exp\left(\frac{-\tau/2 + T_w + 3t_{echo}/2}{T_1}\right) \text{ for } R_3 \text{ \& } R_6 \quad (1.16)$$

The third-order polarization,  $P^{(3)}(t)$ , which is induced in the material when subjected to the three pulse interactions is determined as:

$$P^{(3)}(t) = \int_0^\infty dt_3 \int_0^\infty dt_2 \int_0^\infty dt_1 \sum_1 R_1(\tau, T_w, t_{echo}) \cdot E_3(t - t_{echo}) e^{-i\omega(t - t_{echo})} \\ \times E_2(t - t_{echo} - T_w) e^{-i\omega(t - t_{echo} - T_w)} E_1^*(t - t_{echo} - T_w - \tau) e^{i\omega(t - t_{echo} - T_w - \tau)} \quad (1.17)$$

where  $E_1$ -  $E_3$  represent the electric field envelopes of the laser pulses.

Although the third order response is calculated as the sum of all eight response functions above for completeness, not all of the eight pathways contribute to the signals measured in this work. For time steps in the vibrational echo decays where  $\tau$  is negative and  $T_w$  is positive, only  $R_4$ - $R_6$  contributes to the net polarization. Likewise, when  $\tau$  and  $T_w$  are both positive only  $R_1$ - $R_3$  contributes, and  $R_7$  and  $R_8$  do not contribute to our calculated observables since  $T_w$  is always positive. Experimentally,  $R_7$  and  $R_8$  contribute only near  $\tau = T_w = 0$  when the excitation beams temporally overlap. All eight pathways must be considered to properly treat time-overlapping pulses where, depending on  $T_w$ , all eight diagrams may contribute to the measured signals. However, in practice, the convolution of the system response with the pulse envelopes is found to play a negligible role in the calculated echos, and delta functions were used in this work to simplify calculations (impulsive limit). Finally, the homodyne-detected integrated vibrational echo signal is calculated as:

$$S(T_w, \tau) = \int_0^\infty |P^{(3)}(T_w, \tau, t_{echo})|^2 dt \quad (1.18)$$

The calculated echo signals are then compared to the experimental signal and the parameters in  $C(t)$  are changed accordingly until a sufficient fit has been made. In

the fitting of the data in this work, the datasets were first aliased onto a mesh with data spacings of 0.2 ps. The  $T_1$ s were measured directly by setting  $\tau = 0$  and scanning  $T_w$  (transient grating technique). The vibrational anharmonicity was obtained by measuring the vibrational echo spectrum at  $\tau = T_w = 0.5$  ps and then fitting the 0-1 and 1-2 transitions to Gaussian functions. The vibrational echo decays at all spectrally resolved frequencies and all  $T_w$ s were fit simultaneously together with the baselined and normalized linear lineshape.

#### **1.3.4. Experimental Setup of Homodyne Detected 2D-IR VES**

The arrangement of optics used for the 2D-IR VES experiments in this work is shown in Figure 1.2 (a complete description of the experiment setup, including the generation of the mid-IR and beam properties, is provided in Section 3.3.4). Here, the initial beam starts as a red line on the left of the image. The paths of the pulses are represented as colored lines: the first pulse follows the blue line, the second pulse follows the purple line, and the third pulse follows the red line. The green line in this diagram shows the path of the “tracer”, which is a low power beam ( $\sim 1\%$  of the total power) that is used to locate and align the vibrational echo signal into the monochromator. As such, this beam is blocked during measurements. The pink line shows the path of the vibrational echo after it is generated at the sample (orange rectangle). With the removable mirror (black circle capped line) the vibrational echo can be directed to a single element detector or into a monochromator for data collection.

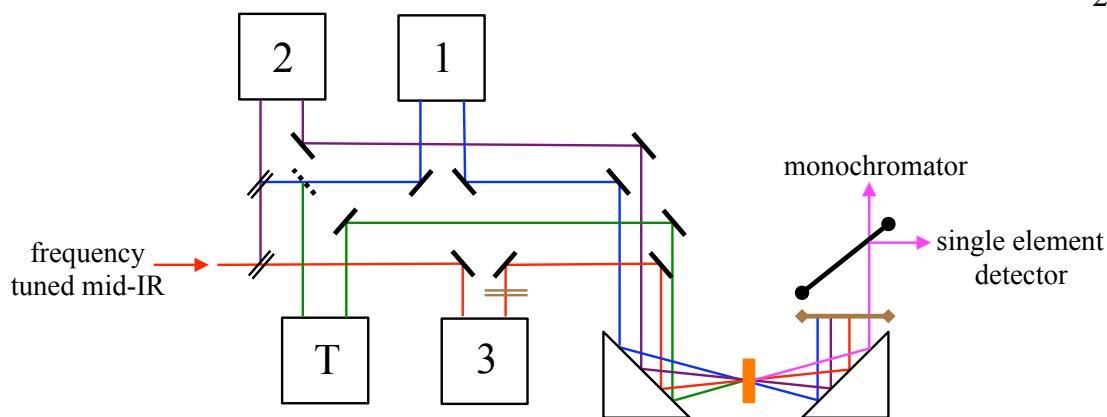


Figure 1.2: Schematic diagram of the 2D-IR VES optics setup. All optics are represented in black: double lines are beam-splitters, solid lines are mirrors, dotted lines are windows, squares are corner-cube mirrors, triangles are off-axis parabolic mirrors, and circle capped lines are removable mirrors. The brown double line designates a chopper, the brown square capped line designates an iris, and the orange rectangle designates the sample. All colored lines represent beam pathways: blue line = pulse 1, purple line = pulse 2, red line = pulse 3, green line = tracer, and pink line = vibrational echo.

The majority of the optics in this setup are 1 inch diameter gold mirrors, which are represented by short solid black lines. In addition, the setup includes two ZnSe beam splitters (double black lines), one ZnSe window (dotted black line), and four gold corner cube mirrors (black squares), and two off-axis parabolic gold mirrors (black triangles). The first beam splitter in the path of mid-IR light allows 33 % of the total power to pass through and reflects the remaining power towards the second beam splitter. The transmitted light becomes the third pulse (red line) in the pulse sequence, while the reflected light goes on to form the remaining pulses and the tracer. When the reflected light from the first beam splitter reaches the second beam splitter the beam power is divided in half: transmitting half of the total power to become the second pulse (purple line), and reflecting the remaining half of the power to become the first pulse and the tracer. The reflected light from the second beam splitter is then directed

towards a ZnSe window that transmits 95 % of the total power to become the first pulse (blue line) and reflects only 5 % of the power to be used as the tracer (green line). Thus, each of the pulses in the pulse sequence passes through exactly one 5 mm thick ZnSe optic and is approximately 33 % of the initial power.

All of the beam pathways, including the tracer, also incorporate a corner-cube mirror (black squares). The corner-cubes have two important features: first they are used to change the timings between pulses, and second, they are built such that the height of a beam may be changed. The corner-cubes of the first and second pulses (black boxes 1 and 2, respectively) are mounted on computer-controlled delay stages, which allow the  $\tau$  and  $T_w$  time periods to be changed during different experiments. In this experiment, it is also necessary to have certain beams at different heights in order to construct the BOXCARS geometry (refer to Section 3.3.4.) that is used to generate the vibrational echo signal in a phase-matched and spatially separated direction. For reference, the first pulse and the tracer are at a height of 4.5 inches, the second pulse is at a height of 5.5 inches, and the third pulse is at height of 3.5 inches after interacting with their respective corner-cubes. Once the three pulses are separated by height, they are arranged in a BOXCARS geometry and are directed into an off-axis parabolic mirror (black triangle) that focuses the beams onto the sample. After passing through the sample the vibrational echo is generated in the remaining corner of the square, where it can be directed to the monochromator for data collection.

For all experiments, including measurements of vibrational echo decays and transient grating measurements, it was necessary to overlap the beams used in the pulse sequence spatially and temporally. Spatial overlap was achieved by directing the beams



through a 100  $\mu\text{m}$  pinhole at the focal point of the three beams. To find a rough estimate of the temporal overlap (where  $\tau = T_w = 0$ , the zero-point), a  $\text{AgGaS}_2$  frequency-doubling crystal was placed at the focal point of the beams. Initially, beam 2 was blocked, leaving only beams 1 and 3 overlapped in the crystal. An iris and borofloat glass-filter were used to allow only doubled light in the phase-matched direction to pass through to an indium antimonate ( $\text{InSb}$ ) detector. An autocorrelation, which scanned the computer-controlled delay stage for beam 1, was performed to find the point where the signal was at its maximum and the two beams have the best temporal overlap. This point was then set on the computer and the delay stage for beam 1 was moved to this place. This procedure was then repeated for beams 2 and 3, by blocking beam 1 and scanning the delay stage for beam 2. To obtain a more precise definition of the zero-point, an additional procedure was used, which generated a non-resonant 3<sup>rd</sup> order signal produced from all three beams incident on a sample of carbon tetrachloride. Autocorrelations with the same beam combinations as those used with the  $\text{AgGaS}_2$  crystal procedure were performed iteratively until the three beams were within  $\pm 10$  fs of each other. Having set the zero-point with these initial procedures, the vibrational experiments were then performed with  $\tau$  and  $T_w$  values using this point as a reference.

## 1.4. Thesis Synopsis

The remaining chapters in this thesis are organized as follows. Chapter 2 examines the steady state properties of poly(3-alkylthiophene)/porphyrin blended films. This work employs the use of FTIR, UV-visible, and fluorescence spectroscopies, as well as TEM measurements to characterize films during a solvent annealing treatment,

which is known to improve film conductivities. While this chapter does not address the primary goals of this work, to examine the relationships between molecular dynamics and charge mobilities, it does provide substantial characterization of the blended films examined in later chapters. Chapter 3 builds on the work discussed in Chapter 2 by examining the 2D-IR VES molecular dynamics and field effect mobility measurements of blended poly(3-hexylthiophene) (P3HT) and ruthenium octaethyl porphyrin (RuOEP) films at different stages of the solvent annealing process first examined in Chapter 2. Thus, this chapter begins to characterize the molecular dynamics in conducting films in relation to charge mobilities by observing films with different intrinsic conducting abilities.

Chapter 4 continues along these lines considering another conducting polymer, polyaniline. In this chapter, the molecular dynamics of three unique polyaniline thin films with varying conductivities are measured. The work examines polyaniline in its emeraldine base form (PANI-EB, semiconducting), and its emeraldine salt (PANI-ES) form doped with dinonylnaphthalene sulfonic acid (DNNSA, conductive) and camphor sulfonic acid (CSA, highly conductive). Chapter 5 also examines polyaniline thin films, however, in this chapter, the static and dynamic structural changes that occur in polyaniline (PANI) thin films over the course of a single deprotonation and reprotonation cycle are presented. This chapter follows a PANI-ES film doped with CSA through a treatment cycle in which the film is dedoped with ammonia gas and is then redoped with a humid followed by dry air treatment. Thus, this chapter examines the static and dynamic memory effects in PANI thin films.

## Chapter 2

# Infrared Spectroscopic Signatures of Phase Segregation in P3HT-Porphyrin Blends

Reproduced in part with permission from:

Audrey A. Eigner, Patrick E. Konold, and Aaron M. Massari. Infrared Spectroscopic Signatures of Phase Segregation in P3HT-Porphyrin Blends. *Journal of Physical Chemistry B*. **2009**, 113, pp. 14549 – 14554.

Copyright, 2009 American Chemical Society.

## 2.1. Chapter Summary

This chapter examines the steady-state properties of porphyrin-polymer blended thin films. The porphyrins RuTPP and RuOEP were considered in conjunction with a series of poly(3-alkylthiophene) polymers including P3HT, P3OT, and P3DDT. RuTPP was observed to form aggregates in chloroform solution and was not considered further. RuOEP did not form aggregates in chloroform solution and was further examined in P3HT, P3OT, and P3DDT films. The FTIR spectrum of the ruthenium-bound CO symmetric stretching mode of RuOEP in P3OT and P3DDT films was observed to evolve dramatically within hours after casting, while the evolution of the CO mode in P3HT films was minimal over several days. Phase segregation of RuOEP and P3HT in thin films during a solvent annealing treatment was investigated with infrared, UV-visible, and fluorescence spectroscopies, as well as transmission electron microscopy (TEM). The FTIR spectrum of the ruthenium-bound CO symmetric stretching mode exhibited significant changes as these films were annealed in solvent vapors. The development of multiple inhomogeneously broadened microenvironments was observed, and UV-visible spectra and TEM supported a model of homogeneous porphyrin distribution throughout the P3HT films that gradually becomes more heterogeneous as the P3HT and RuOEP molecules phase segregate. A complete model for the phase segregation process experienced by the embedded RuOEP is proposed to explain the collective experimental observations.

## 2.2. Introduction

The optimization of morphology and phase segregation in blended organic films is crucial to a material's performance in semiconducting devices. The control of phase segregation has led to a wealth of self-assembled nano- and microscopic structures in multifunctional block copolymers.<sup>116-119</sup> Conversely, organic blends for bulk heterojunction solar cells remain poorly optimized, relying heavily on coincidental phase segregation to achieve electron and hole carrying domains with appropriate size dimensions and connectivity.<sup>16</sup> In some cases, efforts to manipulate phase morphologies have produced devices with enhanced properties. The aggregation of perylene derivatives during thermal annealing in fluorene copolymers and polystyrene blends, for example, resulted in higher charge mobilities and photovoltaic device efficiencies.<sup>120</sup> Similar behavior was observed in blends of perylenes and liquid crystalline molecules that self-assembled into nanoscopic n- and p-type domains to generate relatively high photocurrents.<sup>121,122</sup> On the other hand, examples in which material performance deteriorates due to phase separation can also be found in the literature. For instance, the thermal annealing of fullerene derivatives in polystyrene was reported to actually decrease charge mobility through the fullerene phase.<sup>17</sup> Understanding and controlling phase segregation is thus an important aspect of material optimization.

Some of the more commonly used polymers in organic blended films are poly(3-alkylthiophenes). The use of these polymers is due mainly to their ability to form ordered, semicrystalline domains with enhanced charge mobilities, but also to their exceptional processability. In bulk heterojunction photovoltaic cells, P3HT is often

blended with the fullerene derivative [6,6]-phenyl-C<sub>61</sub>-butyric-acid-methyl-ester (PCBM) and then thermally annealed to increase the crystallinity in the P3HT regions and drive phase segregation of the P3HT and PCBM molecules.<sup>16,18</sup> Consistent with the examples cited above, thermal processing of these blends initially enhances, but ultimately becomes detrimental to the efficiency of photovoltaic devices. This is perhaps due to a decrease in the electron mobilities in the fullerene domains,<sup>17</sup> or because the domain sizes have exceeded the exciton diffusion length.<sup>16,123</sup>

Owing to their strong light absorbing properties, porphyrins are a general class of organic molecules that have a long history in organic photovoltaics.<sup>124-127</sup> The visible absorption spectra of porphyrins are natural complements to that of P3HT, which has led to their inclusion in blended photoanodes with extended spectral responses.<sup>15,128</sup> Since porphyrins are hole transporting semiconductors, their blends with P3HT often constitute a hybrid p-type domain, although in some cases the porphyrin has been reported to serve as a charge transfer mediator between the P3HT and an n-type material.<sup>128</sup> While aggregation of porphyrins in solution is a well-documented phenomenon,<sup>129-131</sup> little has been reported about their phase segregation in blended organic thin films.

In this chapter, RuOEP and RuTPP are examined in blended films with P3HT, P3OT, and P3DDT. The phase segregation process in blended films of RuOEP and P3HT is investigated spectroscopically as the films are progressively annealed in solvent vapors. In the mid-IR, the ruthenium-bound carbonyl (CO) symmetric stretching mode on the RuOEP serves as a sensitive probe of the phase segregation progress, and provides insight into the molecular structures that exist within the

aggregates that form. The visible Soret absorption band of the RuOEP also provides a complementary, albeit less sensitive, probe of molecular aggregation. The segregated phases are directly observed using transmission electron microscopy (TEM), and a model is described that explains the collective experimental results.

## **2.3. Experimental**

### **2.3.1. Materials**

Electronic grade regioregular poly(3-hexylthiophene-2,5-diyl) (P3HT), electronic grade poly(3-octylthiophene-2,5-diyl) (P3OT), and electronic grade poly(3-dodecylthiophene-2,5-diyl) (P3DDT) were used as received from Rieke Metals Incorporated. 2,3,7,8,12,13,17,18-octaethyl-21*H*,23*H*-porphine ruthenium(II)carbonyl (RuOEP) and 5,10,15,20-Tetraphenyl-21*H*,23*H*-porphine ruthenium(II) carbonyl (RuTPP) were used as received from Sigma-Aldrich. All solvents were reagent grade and were used as received without further purification.

### **2.3.2. FTIR of Porphyrins in Solution**

Porphyrin-solvent solutions were made by dissolving 4 mg of RuOEP or RuTPP in 1 mL of chloroform. Two additional porphyrin-solvent solutions were made in the same manner, but were additionally filtered through a 0.45  $\mu\text{m}$  syringe filter. To record FTIR spectra, a 100  $\mu\text{L}$  aliquot of each solution was placed between two 1 inch diameter  $\text{CaF}_2$  windows, separated by a 50  $\mu\text{m}$  teflon spacer and held together with a small copper cell. FTIR spectra of each solution were taken with a ThermoElectron 6700 spectrometer using 2  $\text{cm}^{-1}$  resolution and 16 scans averaged.

### **2.3.3. FTIR of RuOEP Concentration in P3HT Films**

Thin films of P3HT and RuOEP were made with porphyrin to polymer mass

ratios of 1:5, 1:10, 1:25, 1:50, and 1:100. A stock solution of 6 mg of RuOEP in 300  $\mu\text{L}$  chloroform was prepared. Aliquots of the stock solution were then added to 12 mg of P3HT in a volume of chloroform such that the final volumes of the mixtures were 300  $\mu\text{L}$ . All solutions were heated to 40 to 45  $^{\circ}\text{C}$ , stirred for 10 min, and then filtered through a 0.45  $\mu\text{m}$  syringe filter to remove particulates. A 250  $\mu\text{L}$  aliquot of each solution was then dropped onto a  $\text{CaF}_2$  window and spin-coated at 400 rpm for 2 min. FTIR spectra were collected with a ThermoElectron 6700 spectrometer using 2  $\text{cm}^{-1}$  resolution, automatic atmospheric suppression, and 100 scans averaged. Baselined spectra were obtained by using the automatic baseline correct feature in Omnic (version 7.4). For the 1:100 sample an additional baseline procedure was used in which a polynomial was fit to the data outside of the area of interest and then subtracted from the spectrum.

#### **2.3.4. FTIR of P3OT and P3DDT blends with RuOEP observed over time**

To make a 1:20 mass ratio mixture, 4 mg of RuOEP and 80 mg of P3OT or P3DDT were measured out in a small vial. The porphyrin was measured first and the polymer was packed down slightly before adding 1.6 mL of chloroform. The solution was stirred with magnetic stir bar for approximately one hour at 45  $^{\circ}\text{C}$ . The solution was then filtered through a 0.45  $\mu\text{m}$  syringe filter and was left set for one hour before casting films. To make thin films, a 500  $\mu\text{L}$  portion of solution was dropped onto a 1 inch diameter  $\text{CaF}_2$  window and then spun at 400 rpm for 4 minutes. The FTIR spectra were recorded as in Section 2.3.2. immediately after casting, and then every several hours for a few days.



### **2.3.5. FTIR Annealing Studies of P3HT-RuOEP blended films**

To prepare a 1:10 mass ratio mixture, 3 mL of chloroform were added to 200 mg of P3HT and 20 mg of RuOEP in a small glass vial. The solutions were prepared as above allowing for an additional 5 minutes of stirring and using a 700  $\mu$ L aliquot of solution for spin-coating. The dried thin films were mounted vertically in an open copper sample cell and placed in a 32 oz polyethylene terephthalate jar, which had CaF<sub>2</sub> windows as its end caps. This allowed the FTIR spectra to be measured during the annealing process without having to move the sample. To begin the annealing processes a small reservoir of chloroform was placed in the jar with the sample and the lid was quickly secured. Spectra were taken once per minute for the first few minutes and then in larger increments as the annealing progress slowed. Only three scans were averaged for these measurements for expediency.

### **2.3.6. UV-visible spectroscopy of annealed and unannealed P3HT-RuOEP films**

Samples for UV-visible spectroscopy were prepared from diluted solutions of the FTIR studies above. Typically, 600  $\mu$ L of the concentrated solution were diluted with 1.5 mL of chloroform. The solutions were spin-coated, as before, onto CaF<sub>2</sub> windows. UV-visible absorption spectra were collected on a Perkin Elmer UV-visible spectrometer (Model Lambda-12). The Soret band was separated from the background absorbance of P3HT by subtracting a Gaussian fit of the data outside the area of interest and then subtracting it from the spectrum. The obtained spectra were then baselined by subtracting a polynomial fit to the data outside of the Soret region.

### **2.3.7. TEM of annealed and unannealed P3HT-RuOEP**

Transmission electron microscopy (TEM) was performed at the University of Minnesota Characterization Facility on a JEOL 1210 at 120 kV. Sample solutions were prepared as above for UV-visible spectroscopy and spin-coated onto glass microscope slides. After drying, the P3HT coated slides were scored and placed in a dish with Millipure water. Small sections of the films were allowed to float away from the surface of the glass and were captured onto 400 mesh, copper TEM grids (Ted Pella). The grids were allowed to dry for at least an hour before TEM measurements were performed.

### **2.3.8. Fluorescence Spectroscopy of P3HT-RuOEP films**

Thin films for fluorescence were made the same as films in Section 2.3.5. The fluorescence spectra of the samples were acquired using front face collection geometry and a SPEX Fluorolog 1680 0.2 m double spectrometer. The samples were excited with 390 and 510 nm light generated from a xenon lamp, which correspond to porphyrin and polymer peaks respectively. The excitation wavelength was held fixed while the emission wavelength was varied to collect the fluorescence of different wavelengths using a photomultiplier.

### **2.3.9. FTIR of P3HT-RuOEP with pyridine**

Solutions of P3HT and RuOEP in chloroform were made in the same manner as in Section 2.3.5. Pyridine was added to solution such that there was a 7:1 mol ratio of pyridine to RuOEP. Thin films were then cast and annealed in the same way as in Section 2.3.5.

## 2.4. Results and Discussion

### 2.4.1. Porphyrin Aggregation in Solution and Thin Films

The metal-bound CO vibration has been shown to have a large Stark coupling constant, which makes it a sensitive probe of the distribution of proximal chemical environments.<sup>132</sup> In this study, the distribution of CO stretching frequencies observed in the FTIR spectra corresponded to the different sub-environments that surround the individual vibrational modes. In a sample where the porphyrin is well dispersed among the polymer chains, this distribution reflects solvation of the vibrational mode by proximal P3HT chains. In contrast, if aggregates of porphyrin molecules are formed, this distribution will reflect solvation of the vibrational mode by proximal RuOEP molecules. Figure 2.1 shows the FTIR spectra of the CO symmetric stretching vibration for the porphyrins RuOEP and RuTPP dissolved in chloroform. Comparing the FTIR of the filtered and unfiltered solutions, the RuTPP in chloroform solution is changed by filtration, while the RuOEP in chloroform solution is unaffected by filtration. The CO transition in the unfiltered RuTPP solution FTIR has sharp peaks and shoulders, and is clearly composed of multiple lineshapes. In contrast, the CO transition of the filtered RuTPP solution FTIR is smooth and Gaussian shaped. This observation indicates that aggregates of RuTPP larger than the 0.45  $\mu\text{m}$  filter pores exist in the unfiltered solution. For RuOEP, the FTIR of the filtered and unfiltered solutions are practically identical and suggest no aggregation in solution. Due to this tendency, the polymer films examined in this work were subsequently only made using RuOEP.

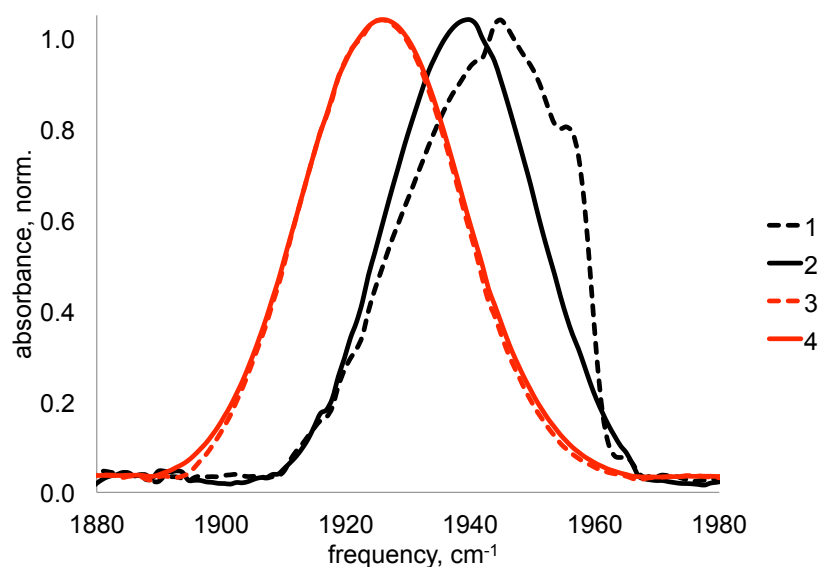


Figure 2.1: FTIR Spectra of the CO symmetric stretching vibration for (1) RuTPP unfiltered, (2) RuTPP filtered, (3) RuOEP unfiltered and (4) RuOEP filtered solutions.

In order to demonstrate the absence of pre-formed porphyrin aggregates in the blended films, a concentration study of the FTIR spectra for this stretching region was performed. Figure 2.2 shows the baselined and normalized FTIR spectra of the CO stretching region for the 1:5, 1:10, 1:25, 1:50, and 1:100 RuOEP to P3HT mass ratio films. The ruthenium-bound CO symmetric stretching mode is centered at  $1932\text{ cm}^{-1}$  in these unannealed RuOEP-P3HT films and has a spectral width of approximately  $18.5\text{ cm}^{-1}$  FWHM. The spectral shapes are nearly the same over a factor of 20 in concentration and the center frequencies do not change within the resolution of the instrument used. The slight broadening of the lower concentrations is likely the result of imperfect baselining, which affects the low concentrations more severely because the CO absorbances are very small compared to the background. Based on these results, there is likely no significant RuOEP aggregation in these unannealed films over this concentration range.

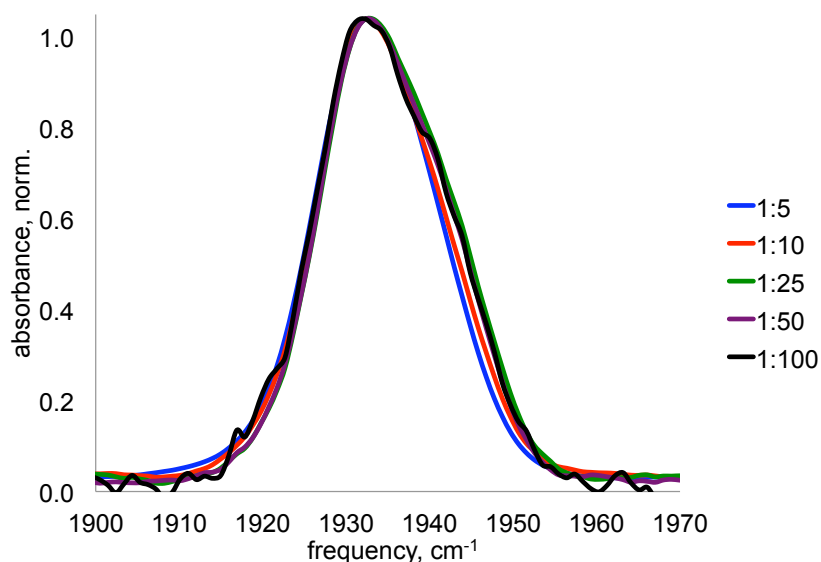


Figure 2.2: FTIR Spectra of RuOEP in blended films of RuOEP:P3HT with different mass ratios.

#### 2.4.2. Evolution of Blended Films Observed Over Time

Figure 2.3 shows the FTIR spectra of the ruthenium-bound CO of RuOEP in P3HT (A), P3OT (B), and P3DDT(C) films, as recorded over time. For each polymer type, the absorbance peak changes with time, however the evolution of the peak is more drastic in the P3OT and P3DDT films than in the P3HT film. Over the course of five days the CO peak in the P3HT films changes very little. Changes observed for P3OT and P3DDT, on the other hand, occur within 24 hours and are much more significant. In both cases, the peak was observed to split into two absorbances of approximately equal intensity initially, and then convert into a lineshape with several features of varying intensity. It should also be noted here that the FTIR spectra shown for the P3OT and P3DDT films are only one example of the types of changes observed for these films. The evolution of the CO peak in films of these two polymers was found to be inconsistent and unpredictable. In contrast, films made with RuOEP and P3HT were

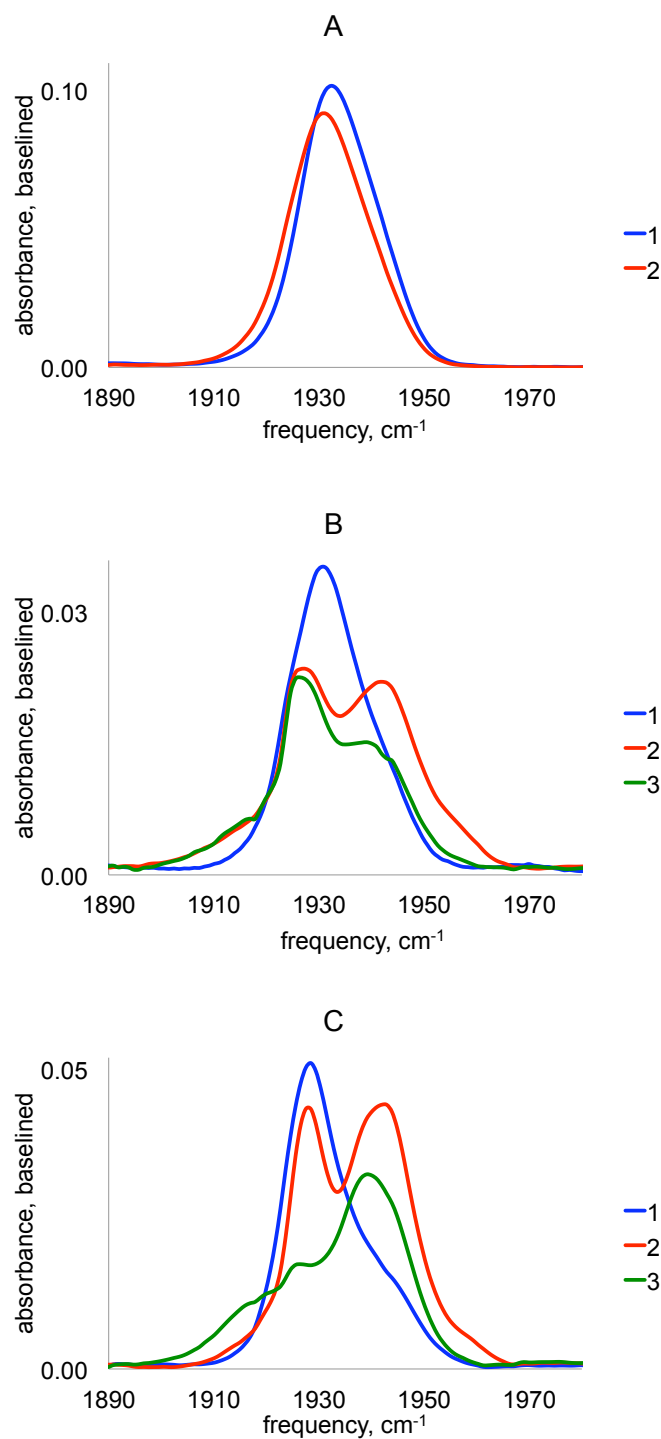


Figure 2.3: FTIR Spectra of RuOEP in (A) a 1:10 weight ratio with P3HT shortly after casting [1] and 5 days after casting [2]; (B) a 1:20 weight ratio with P3OT shortly after casting [1], 20 hours after casting [2] and 25 hours after casting [3]; and (C) a 1:20 weight ratio with P3DDT shortly after casting [1], 4 hours after casting [2] and 21 hours after casting [3].

found to be consistent in the extent and manner in which they evolved. For this reason, only films of RuOEP and P3HT were considered in further experiments.

#### **2.4.3. FTIR of Solvent Annealed P3HT RuOEP Films**

Upon exposure to solvent vapors, the CO absorbance undergoes dramatic changes in shape and frequency. During this annealing process, the solvent vapors penetrate the blended films and partially solvate the organic molecules, thereby increasing their structural mobility. This enables rearrangement and slow diffusion that can lead to phase segregation and increased packing efficiencies.<sup>18,133</sup> For clarity, the successive FTIR spectra during a single annealing run are separated into two subplots in Figure 2.4. Figure 2.4A shows that within the first two minutes of annealing, the CO stretching mode begins to red-shift, ultimately translating from  $1932\text{ cm}^{-1}$  to  $1927\text{ cm}^{-1}$  over the first 20 minutes. This shift is also accompanied by an increase in peak intensity and a decrease in peak width, indicating a decrease in the distribution of the chemical environments that exist around the CO ligand.

Figure 2.4B shows that at longer annealing times the changes in the films begin to slow, and the peak at  $1927\text{ cm}^{-1}$  splits into a broad, red-shifted band centered at  $1919\text{ cm}^{-1}$  and a weak blue-shifted band centered at  $1946\text{ cm}^{-1}$ . During this second spectral transition, an isosbestic point is found at  $1924\text{ cm}^{-1}$ , confirming that during this process there are two distributions whose amplitudes are interconverting without changes to their spectral lineshapes. It is peculiar to note that the spectrum after 70 minutes of solvent vapor annealing consists of broader absorption bands, and therefore an increase in the inhomogeneity of the chemical environments that encompass the ruthenium-bound CO oscillators. In comparison to the lineshape trend shown in Figure 2.4A, this

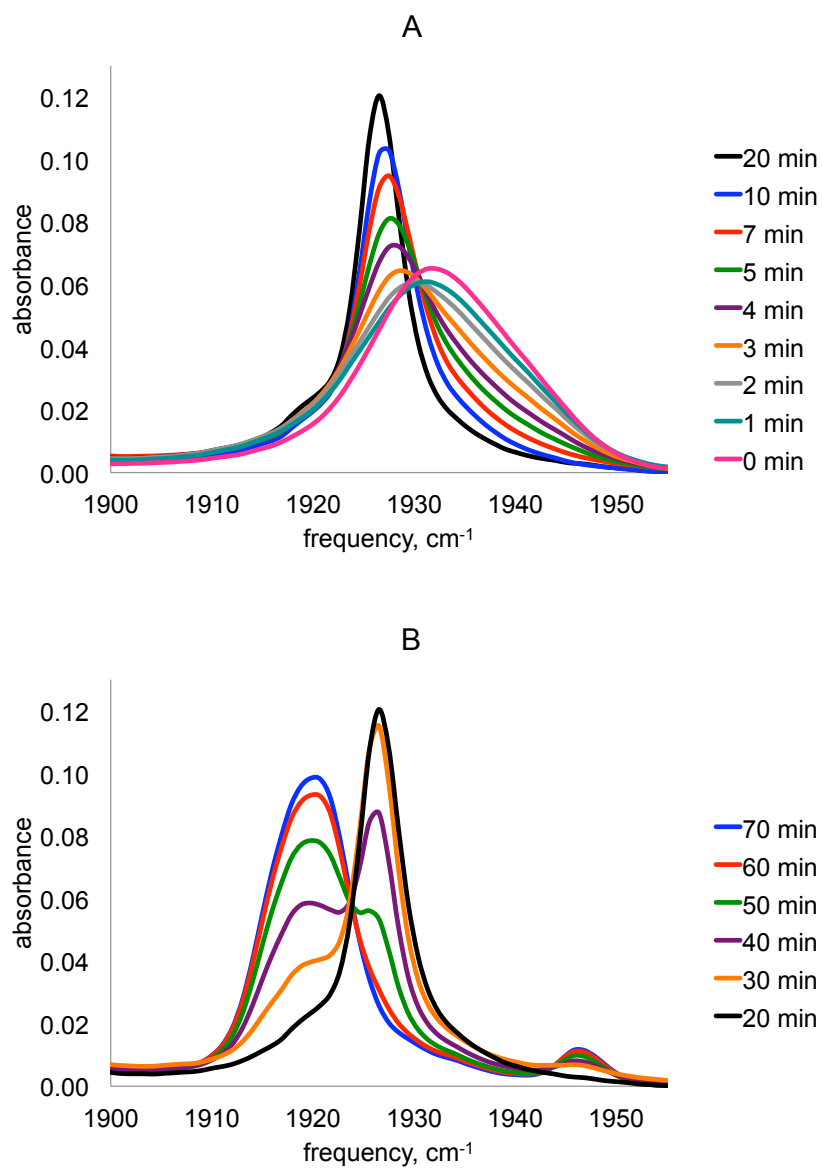


Figure 2.4: Successive FTIR spectra for a 1:10 weight ratio RuOEP:P3HT film during annealing in saturated chloroform vapor.



implies that the electrostatic surroundings in the vicinity of the CO initially become more homogeneous (0 – 20 minutes), and then undergo a subsequent disordering (20 – 70 minutes). The origins of this change are discussed below.

To quantify the FTIR results, the entire series of spectra was fit using three or four Gaussian lineshapes. This invoked a large number of parameters, however, most of the absorption bands are well separated from each other and their necessity in the fits is not ambiguous. In the interest of minimizing adjustable parameters, the center frequencies or linewidths for peaks whose amplitudes were below 10% of the maximum peak value were not varied. In such cases, the centers and widths were maintained at the values obtained for a previous fit in which their amplitude was above this threshold. The fit parameters are compiled in Table 2.1. The final fits at all annealing times are excellent and can be found overlaid with the data from Figure 2.4 in Figure 2.5. The fit parameters allow us to quantify the spectra of three distinct states (Figure 2.6A), which are referred to as unannealed, half-annealed, and fully-annealed in the proceeding paragraphs. These states have FTIR spectra that closely resemble the 0, 20, and 70 minute traces, respectively, in Figures 2.4.

Although the unannealed spectrum is indeed maximal at  $1932\text{ cm}^{-1}$ , it was found that its shape requires two Gaussians to account for asymmetry on the higher frequency side. This is also true of the 1:100 diluted sample spectrum in Figure 2.2. In this work, an explanation of this asymmetry is not sought, but rather a demonstration that this is the spectrum of the homogeneously distributed RuOEP in these blended films, and the components that describe its shape vary in a concerted fashion; as one state goes away, another appears. The half-annealed state is exceedingly narrow, and its shape is not fit

Table 2.1: Gaussian parameters determined to fit the spectra in Figures 2.4A and 2.4B. For each Gaussian curve there is an amplitude ( $a_i$ ), center frequency ( $x_i$ ) in  $\text{cm}^{-1}$ , and standard deviation ( $w_i$ ) in  $\text{cm}^{-1}$ .

variable	0 min.	1 min.	2 min.	3 min.	4 min.	5 min.	7 min.
$a_1$	0.042	0.042	0.034	0.042	0.037	0.032	0.028
$x_1$	1930.9	1930.8	1929.3	1931.2	1930.6	1930.2	1930.2
$w_1$	4.9	5.4	4.7	8.7	8.7	8.5	7.6
$a_2$	0.024	0.019	0.022	0.001	0.000	0.010	0.018
$x_2$	1939.9	1940.7	1938.5	1944.1	1939.8	1927.6	1927.4
$w_2$	5.4	5.3	6.1	1.8	6.3	4.1	3.5
$a_3$	0.015	0.014	0.018	0.021	0.034	0.037	0.047
$x_3$	1929.2	1927.1	1926.9	1928.3	1927.9	1927.7	1927.4
$w_3$	9.2	9.9	9.7	3.1	2.9	2.5	2.2
$a_4$	0.001	0.001	0.000	0.000	0.000	0.000	0.004
$x_4$	1919.0	1919.0	1919.0	1919.0	1919.0	1919.0	1919.0
$w_4$	4.0	4.0	4.0	4.0	4.0	4.0	4.0

Table 2.1: (Continued)

variable	10 min.	20 min.	30 min.	40 min.	50 min.	60 min.	70 min.
$a_1$	0.025	0.002	0.004	0.007	0.008	0.010	0.010
$x_1$	1930.2	1946.5	1946.5	1946.5	1946.5	1946.6	1946.7
$w_1$	6.6	2.3	2.3	2.3	2.3	2.3	2.2
$a_2$	0.029	0.031	0.026	0.020	0.014	0.016	0.012
$x_2$	1927.1	1926.6	1926.4	1926.4	1926.7	1923.7	1923.5
$w_2$	3.1	7.1	7.2	7.7	9.0	9.4	10.7
$a_3$	0.050	0.086	0.082	0.056	0.022	0.000	0.000
$x_3$	1927.1	1926.6	1926.4	1926.4	1926.7	1926.4	1926.4
$w_3$	1.9	1.8	1.7	1.7	1.6	1.6	13.9
$a_4$	0.007	0.001	0.019	0.044	0.069	0.080	0.089
$x_4$	1919.0	1919.0	1919.0	1919.2	1919.6	1919.5	1919.6
$w_4$	4.0	4.0	3.8	4.0	4.1	3.8	3.8

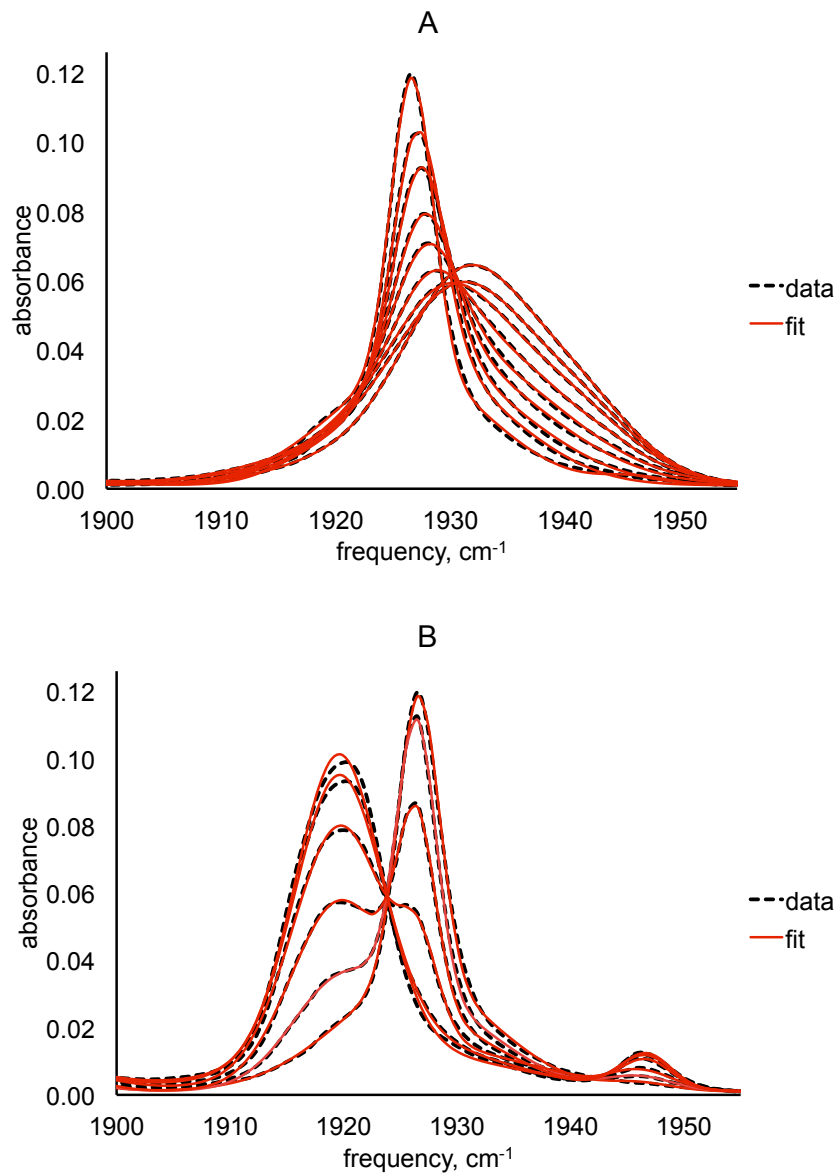


Figure 2.5: Fitted spectra overlaid with actual data from (A) Figure 2.4A and (B) Figure 2.4B.

well by a single Gaussian band. Although the shoulders on this lineshape suggest Lorentzian character, attempts to fit this spectrum with that functional form were not successful. The best fit was obtained as the sum of two Gaussians with coincident centers (see Table 2.1). Again, in the interest of decreasing independent parameters for these fits, the peak centers for these two components were forced to be coincident. While the one dimensional IR spectroscopy used in this work does not have the ability to determine the degree to which a lineshape is homogeneously broadened, it is conceivable that the lineshape is some combination of a predominantly homogeneous population (Lorentzian lineshape) with a smaller amplitude inhomogeneously broadened sub-population (i.e. a Voigt lineshape). This hypothesis was tested by using two-dimensional IR spectroscopy in the work described in Chapter 3 to determine the underlying homogeneous lineshape.<sup>134,135</sup> The bi-Gaussian peak at  $1927\text{ cm}^{-1}$  was characterized using the FWHM of the combined band lineshape. From three minutes annealed, when this spectral component begins to have a prominent amplitude, the FWHM decreases progressively from  $7.3$  to  $5.7\text{ cm}^{-1}$  by 20 minutes annealed (Figure 2.4A), and then remains constant as its amplitude decreases during the final spectra (Figure 2.4B). That the chemical environments around the CO ligand become progressively more homogeneous is suggestive of ordering of the transition dipoles within a molecular aggregate.<sup>136-138</sup>

The integrated absorbances of the components that create the spectra of the unannealed, half-annealed, and fully-annealed states are plotted as a function of annealing time in Figure 2.6B to illustrate the progressive changes that are reported by the ruthenium-bound CO oscillator. The contribution of the unannealed sample

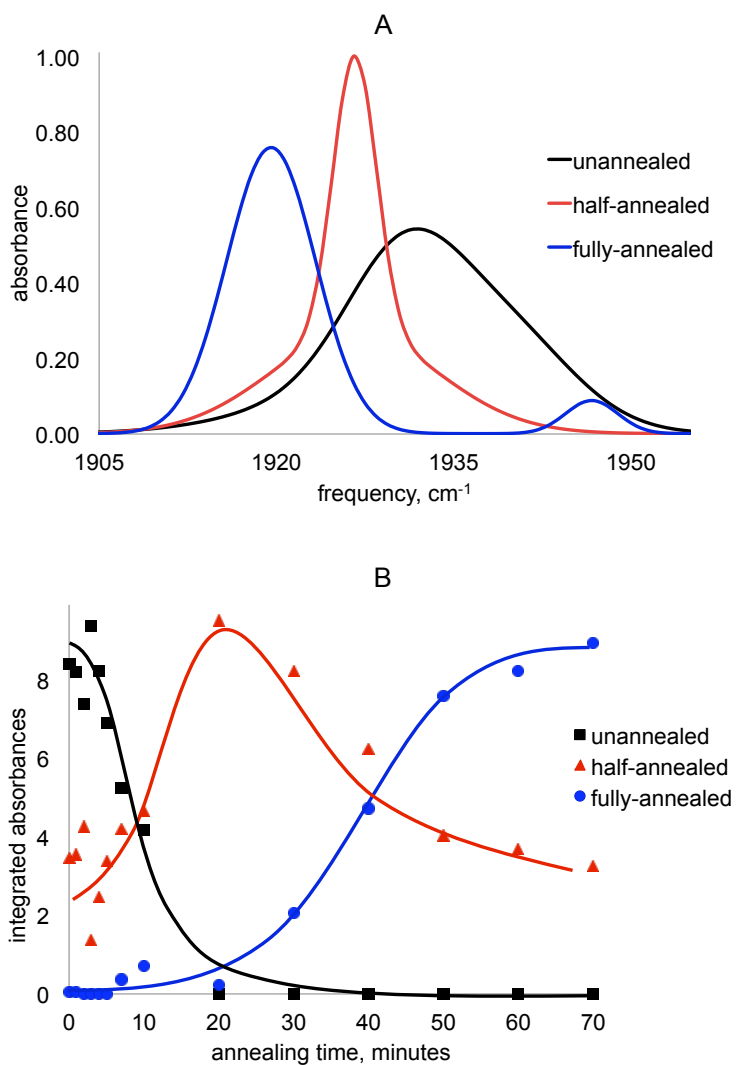


Figure 2.6: (A) Calculated spectra of a 1:10 RuOEP:P3HT blended sample determined by fitting the spectra in Figure 2.4. (B) Integrated absorbances for the components of the spectra of Figure 2.4 as function of annealing time.

spectrum (peak at  $1932\text{ cm}^{-1}$ ) to the overall IR spectrum continually decreases as the annealing time is increased, while the integrated intensity of the half-annealed sample (peak at  $1927\text{ cm}^{-1}$ ) increases until approximately 20 minutes before it begins to diminish. The integrated intensity of the fully-annealed sample spectrum (peaks at  $1919\text{ cm}^{-1}$  and  $1946\text{ cm}^{-1}$ ) steadily increase after 20 minutes while the half-annealed state decreases.

#### **2.4.4. UVvis of Solvent Annealed P3HT RuOEP Films**

To further understand the annealing effect on the RuOEP molecules in P3HT films, UV-visible spectroscopic measurements were performed on the absorption spectrum of the RuOEP Soret band at 390 nm, which has a transition dipole moment in the plane of the porphyrin macrocycle.<sup>139,140</sup> This absorption band is known to report on the aggregation state of porphyrins in solution.<sup>129-131</sup> Figure 2.7A shows the Soret region for the 1:10 RuOEP:P3HT films with the P3HT absorption removed at varying degrees of annealing. By collecting the FTIR spectra on these same samples (Figure 2.7B), the black, red, and blue UV-visible correlate spectra with the unannealed, half-annealed, and fully-annealed states, respectively. During the first spectral transition in the FTIR spectrum (Figure 2.4A), the Soret absorption band broadens from 25 nm to 38 nm (FWHM) without shifting in wavelength, indicating aggregation with random orientation of the in-plane transition dipoles. However, the second FTIR spectral transition is accompanied by a red-shifting of the peak maximum from 390 nm to 401 nm. The full UV-visible absorption spectra are shown in the Figure 2.7C, and show minimal changes to the P3HT absorbance during annealing.

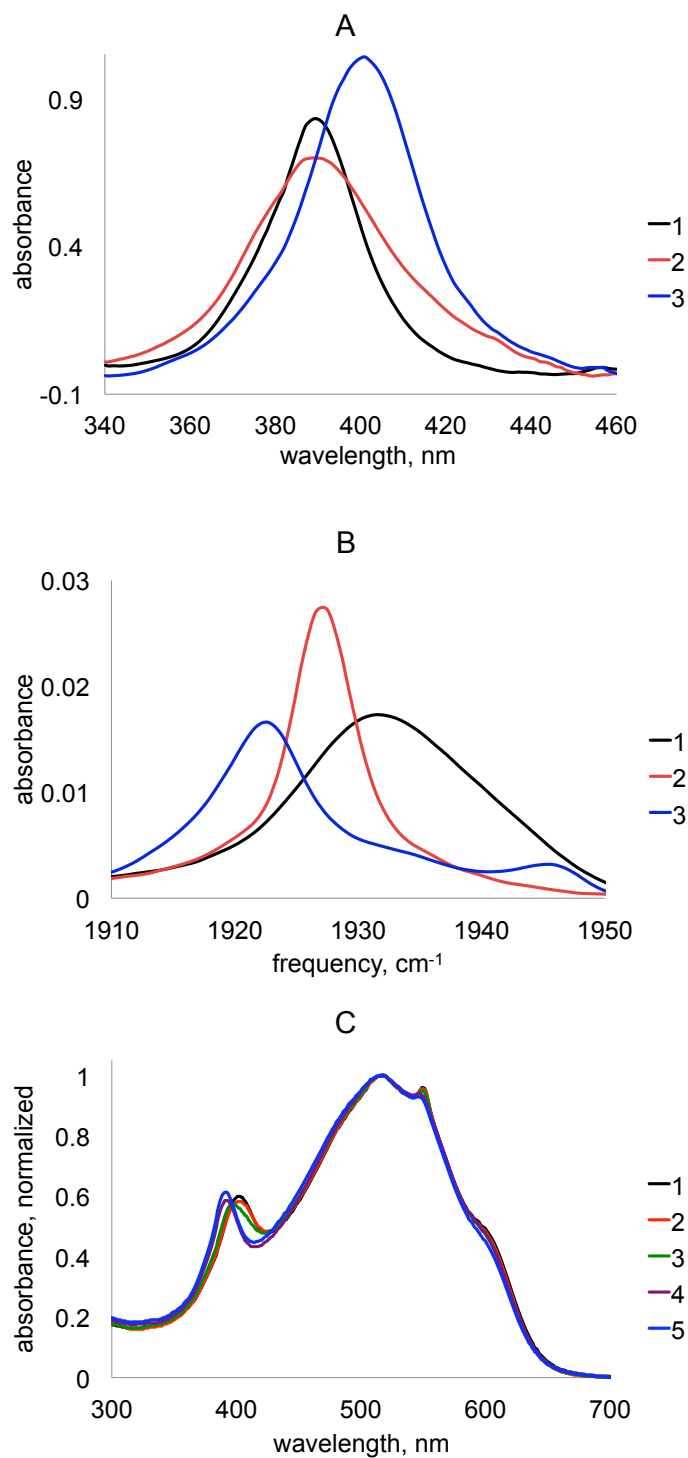


Figure 2.7: (A) UV-visible spectra of the Soret region of RuOEP in a 1:10 RuOEP:P3HT film for [1] unannealed, [2] half annealed, [3] fully annealed. (B) FTIR spectra of CO stretching region for the samples analyzed in Figure 2.7A. (C) Full range absorption spectra of a 1:10 RuOEP:P3HT film with progressive annealing in solvent vapors.

#### 2.4.5. TEM of Solvent Annealed P3HT RuOEP Films

To corroborate the IR and UV-visible spectral evidence of phase segregation and porphyrin aggregation, thin films of P3HT/RuOEP blends before and after annealing, and at different concentrations, were examined using TEM measurements. The ruthenium in the RuOEP is a strong electron scatterer, providing contrast in the TEM images for domains where there are local concentrations of RuOEP (i.e. RuOEP clusters appear dark). The TEM images of these films are shown in Figure 2.8. Prior to annealing, both high (1:10) and low (1:50) concentration films show little to no evidence of RuOEP aggregates on the length scale probed by these measurements (150 nm). This supports the earlier conclusion (see Figure 2.2) that the IR and UV-visible spectral data are reflective of the unaggregated RuOEP molecules that are solvated only by P3HT. After annealing, the 1:10 concentration of RuOEP in P3HT develops into a film with clusters of dark aggregates. This is consistent with the spectroscopic evidence of aggregation in Figures 2.4 and 2.7. It should also be noted that the 1:50 concentration film exhibits no cluster formation after annealing, and its FTIR spectra also show no shape changes with annealing (Figure 2.9). In the more concentrated samples (greater than 1:25 RuOEP:P3HT), however, the annealing process leads to phase segregation and porphyrin aggregate formation. Thus, there is a threshold concentration below which the isolated porphyrins cannot encounter an aggregating partner leading to the UV-visible and FTIR spectral changes.



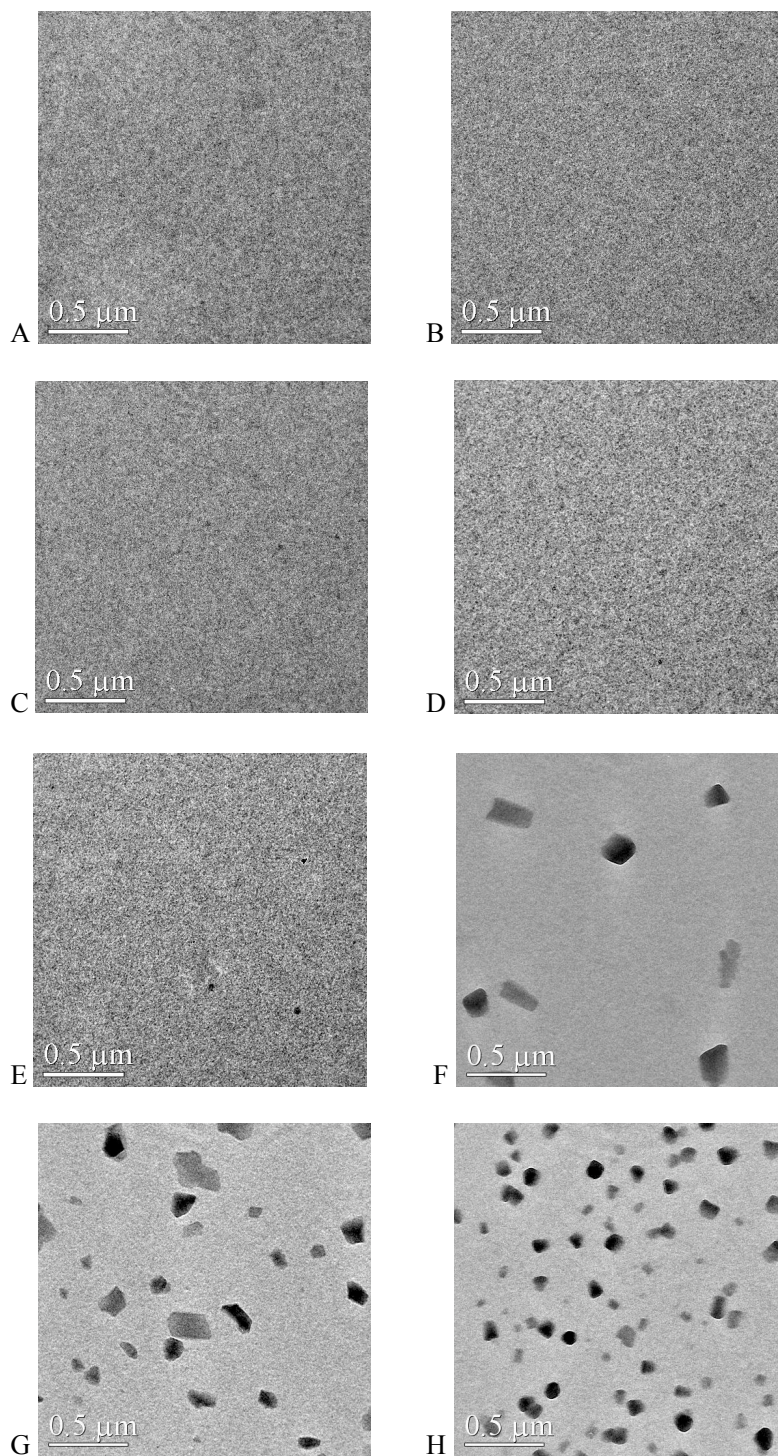


Figure 2.8: TEM images of (A) a P3HT film unannealed, (B) a P3HT film annealed, (C) a 1:50 RuOEP:P3HT film unannealed, (D) a 1:50 RuOEP:P3HT film annealed, (E) a 1:10 RuOEP:P3HT film unannealed, (F) a 1:10 RuOEP:P3HT film annealed, (G) a 1:5 RuOEP:P3HT film unannealed, and (H) a 1:5 RuOEP:P3HT film annealed.

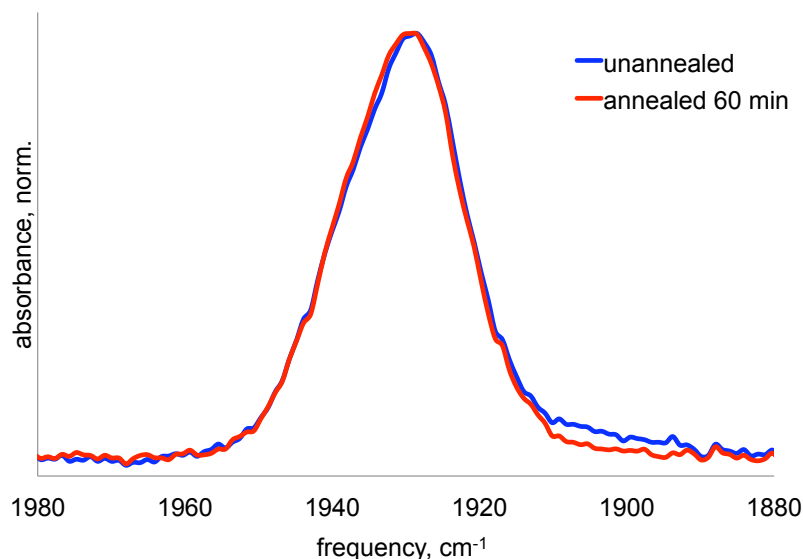


Figure 2.9: Normalized and baselined FTIR spectra of a 1 to 50 RuOEP to P3HT film before and after solvent vapor annealing for one hour.

#### 2.4.6. Fluorescence Spectra of Solvent Annealed P3HT and RuOEP:P3HT blends

From a photovoltaic device perspective, photoluminescence studies of these films indicate that the solvent annealing process results in fluorescence quenching with and without RuOEP (Figure 2.10). Xu and Holdcroft have examined P3HT films with vary degrees of regioregularity and have found that the fluorescence is more quenched in films with higher regioregularity.<sup>141</sup> They have attributed this observation to concentration quenching, which occurs when planar ground and excited state molecules align in close face-to-face proximity of one another.<sup>141</sup> This results in a nonradiative relaxation of the fluorescence as a result of the two species being able to share excitation energy. The effect is more prevalent in regioregular P3HT films than it is in regiorandom P3HT films due to the enhanced packing ability of polymer chains. Barbara and coworkers have additionally suggested that excitons in conjugated polymer

systems may be quenched through interactions with a polaron.<sup>142</sup> In this work, the progressive annealing of the P3HT films results in more ordered crystalline regions and a delocalization of the polaron. Thus, the more efficient nonradiative energy relaxation of the annealed film is most likely a result of a morphological change that brings the thiophene rings into closer proximity.

The 1:10 RuOEP samples also undergo quenching during annealing, and the spectral shapes are constant regardless of excitation wavelength (390 nm is the RuOEP peak and 510 nm is the P3HT peak). Here, the observed spectral trends may also result from the aggregation of porphyrin molecules, which has been shown in many cases to produce strong fluorescence quenching.<sup>143-145</sup> However, it is interesting that the fully annealed blends exhibit less quenching than the half annealed films. This may be a result of less electron and energy transfer between the RuOEP and the polymer chains due to phase segregation of large porphyrin aggregates. Upon normalization (Figure 2.9B), it is apparent that the spectral shapes of all unannealed samples, both with and without RuOEP, are identical, as are the spectral shapes of all of the annealed samples. Thus, it can be concluded that the fluorescence comes mostly from the P3HT, and there is little energy or electron transfer from RuOEP before or after annealing.

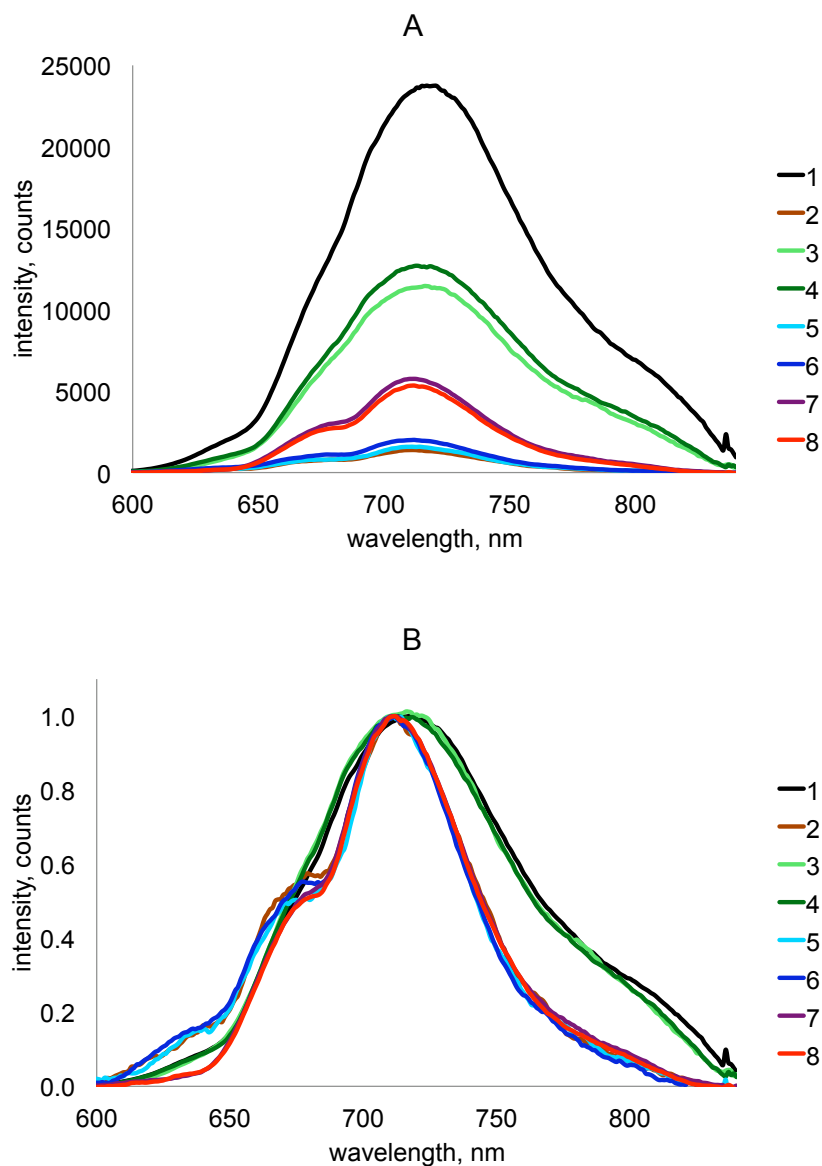


Figure 2.10: (A) Fluorescence spectra of a P3HT film and a 1:10 weight ratio RuOEP:P3HT blended film at three annealing stages. (B) Normalized fluorescence spectra from Figure 2.9A. Legends refer to the following: [1] P3HT unannealed, [2] P3HT solvent annealed 3 hours, [3] RuOEP:P3HT unannealed 390 ex, [4] RuOEP:P3HT unannealed 510 ex, [5] RuOEP:P3HT half annealed 390 ex, [6] RuOEP:P3HT half annealed 510 ex, [7] RuOEP:P3HT fully annealed 390 ex, and [8] RuOEP:P3HT fully annealed 510 ex. Spectral intensities have not been corrected for film absorption since all films had optical densities exceeding 2.

### 2.4.7. Model for Phase Segregation in Solvent Annealed P3HT RuOEP Films

Structural rearrangements into P3HT and RuOEP segregated phases induced by the solvent vapor annealing process are at the origin of the spectral shifts observed in the FTIR and UV-visible spectra above. These changes can be divided into two stages: 1) a red-shifting and narrowing of the CO absorption band with only a broadening of the Soret band, and 2) a splitting of the CO absorption into a broad red-shifted band and a weaker blue-shifted band with an 11 nm red-shift of the Soret band. The shifting of the electronic and vibrational transition energies in the RuOEP molecule can be partly explained by the excitonic coupling model.<sup>136-138</sup> According to this theory, dipolar coupling results in a splitting of an excited state energy level into a higher and a lower energy state, regardless of whether they are electronic or vibrational transitions (Figure 2.11). The net transition moment for these two states determines whether they are allowed or forbidden transitions from the electronic or vibrational ground states. As a result, excitonic coupling of parallel side-by-side transition dipoles leads to a blue-shift of the transition energy, head-to-tail coupling leads to a red-shift, and oblique coupling allows for some finite transition probability to both high and low energy states (band splitting).<sup>136-138</sup>

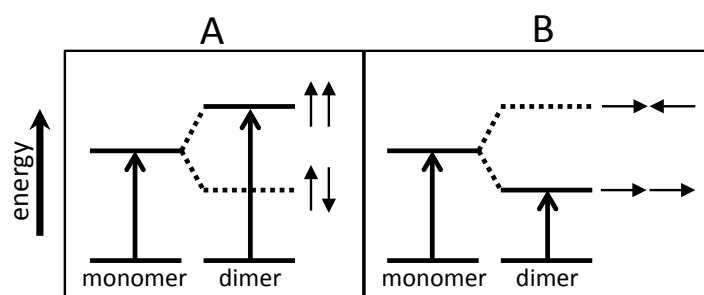


Figure 2.11: Energy diagram showing splitting of excited states as a result of dipole coupling for (A) parallel and (B) head-to-tail interaction.

The RuOEP molecule is unique in that it has two strong transition dipoles, the CO absorption in the mid-IR and the Soret absorption in the visible, which are roughly orthogonal to each other. The annealing process facilitates aggregation of RuOEP molecules that were not initially within a dipole-dipole coupling distance. This mobile phase behavior has been documented for PCBM and P3HT blends upon thermal and solvent annealing.<sup>16,18,133</sup> The red-shift of the ruthenium-bound CO stretch (Figure 2.4A) suggest a head-to-tail interaction of its transition dipoles during the first stage of the annealing process forming a linear vibrational exciton.<sup>104</sup> Concurrently, the Soret band broadening implies that the porphyrins are aggregating with random spatial relationships between the in-plane electronic transition moments. Figure 2.12A shows a hypothetical rendering of this type of arrangement. It is tempting to predict that the RuOEP molecules would aggregate in a face-to-face fashion, however, this would lead to a blue shift in the Soret absorption band, which is not observed. The narrowing of the CO absorption lineshape in Figure 2.4A is also characteristic of an exciton delocalized over several molecules in which a small number of transition energies are allowed and gain oscillator strength.<sup>104,146-148</sup>

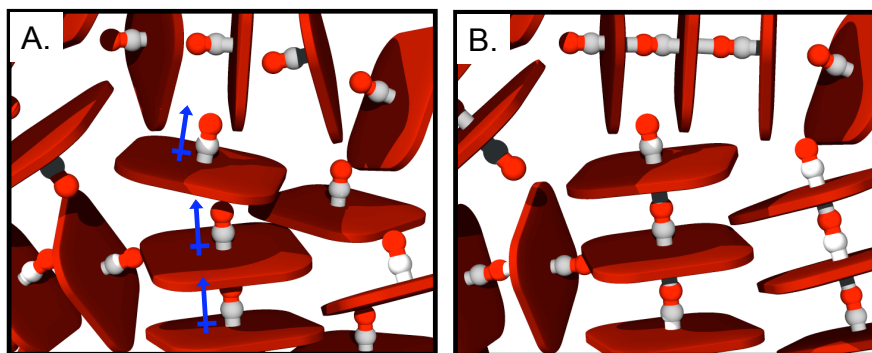


Figure 2.12: Schematic diagram showing the proposed arrangement of RuOEP molecules leading to observed spectral changes during annealing in solvent vapors.

The second stage of the annealing process is difficult to rationalize using the exciton model. Although oblique CO transition moments could lead to the spectral splitting observed in Figure 2.4B, the red-shift of the Soret band seems unlikely since it would imply the porphyrin macrocycles are ordered in a head-to-tail fashion yet remain separated by enough distance to avoid parallel dipole interactions. The broadening of the CO stretch during this stage is also not consistent with this model since it implies that the aggregates initially order in the dimension of the CO stretch and then subsequently disorder. We hypothesize an alternate explanation for these data that involves the formation of a bridging isocarbonyl ligand (Figure 2.12B). The sixth coordination site on the ruthenium will indeed bind an appropriate ligand, and, although the oxygen terminus of the CO is not a strong ligand, there is evidence in the literature for these types of bridges in solid state compounds.<sup>149-152</sup> This type of coordination results in quasi-1D aggregates of RuOEP in which the bridging CO ligands are red-shifted and the capping CO ligands are blue-shifted, consistent with the fully-annealed FTIR spectrum. Using the integrated areas of the split bands in this spectrum, assuming equal oscillator strengths in the two states, we can estimate that the ratio of interior to capping COs is 15:1, giving an average chain length of 16 RuOEPs. Binding of the sixth ligand also causes the red-shift that was observed in the Soret band upon fully-annealing (Figure 2.13B). Therefore, we believe that the spectral changes in the first stage of annealing are driven by excitonic coupling (Figure 2.4A), whereas the changes in the second stage (Figure 2.4B) occur when aggregation forces RuOEP molecules into ever closer proximity and a weak bridging coordination bond is formed.

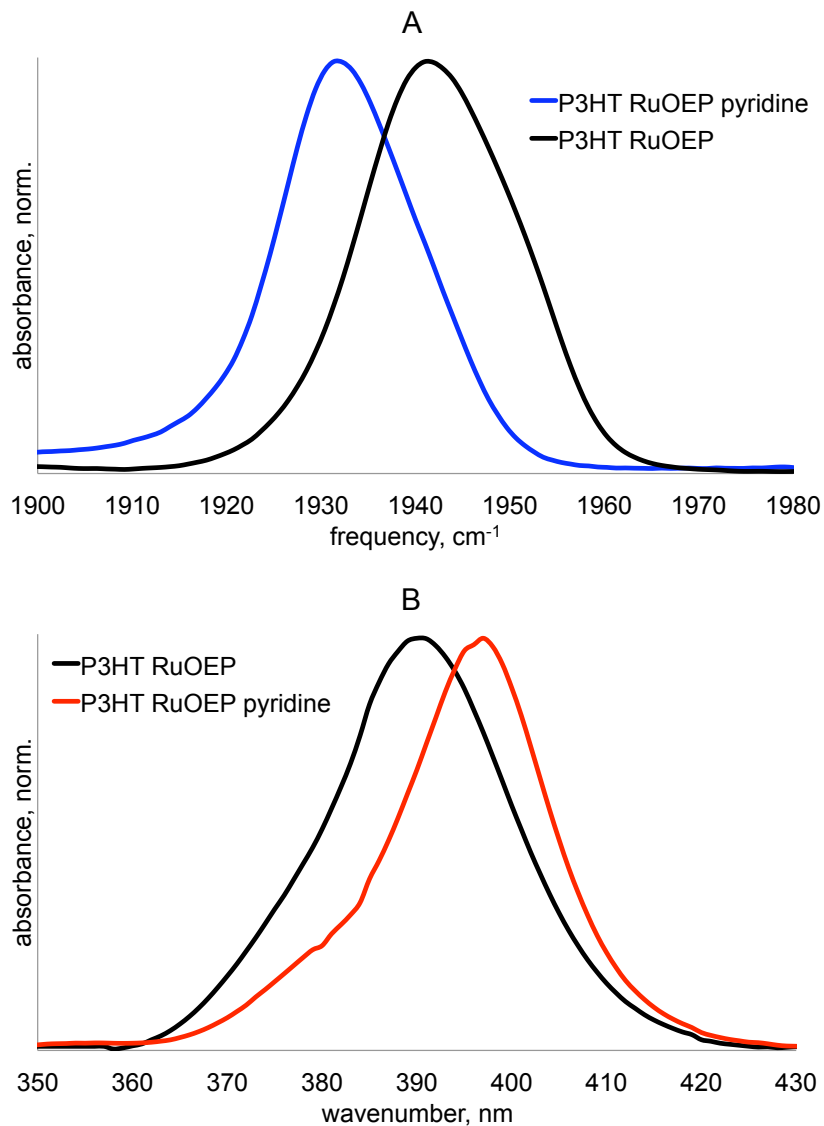


Figure 2.13: (A) FTIR showing the CO symmetric stretching region and (B) UV-visible spectra showing the Soret band region of a RuOEP:P3HT film compared with a RuOEP:P3HT film with pyridine binding of the porphyrin.



Conclusive evidence of this 1D coordination polymer-like arrangement of RuOEP molecules in the phase segregated aggregates at long annealing times could be provided by a crystal structure analysis, which is an on-going effort in our lab. In lieu of this data, we note the following additional evidence for bridging isocarbonyl formation. Coordination of the sixth coordination site on the ruthenium with pyridine prior to P3HT/RuOEP film casting resulted in the expected blue-shift of the CO symmetric stretching frequency (Figure 2.13A), as well as a red-shift of the Soret band due to ligation on the backside of the RuOEP (Figure 2.13B). Upon annealing of these films in solvent vapor, the CO stretching frequency red-shifts, as it did in Figure 2.4, but, rather than continuing to split into a red-shifted peak and a small blue-shifted peak, it then settles slightly back to the blue (Figure 2.14A). Figure 2.14B additionally shows that the Soret band in these films does not shift upon annealing. Thus, by filling the sixth coordination site of the RuOEP with pyridine, we are able to shut down the second annealing stage.

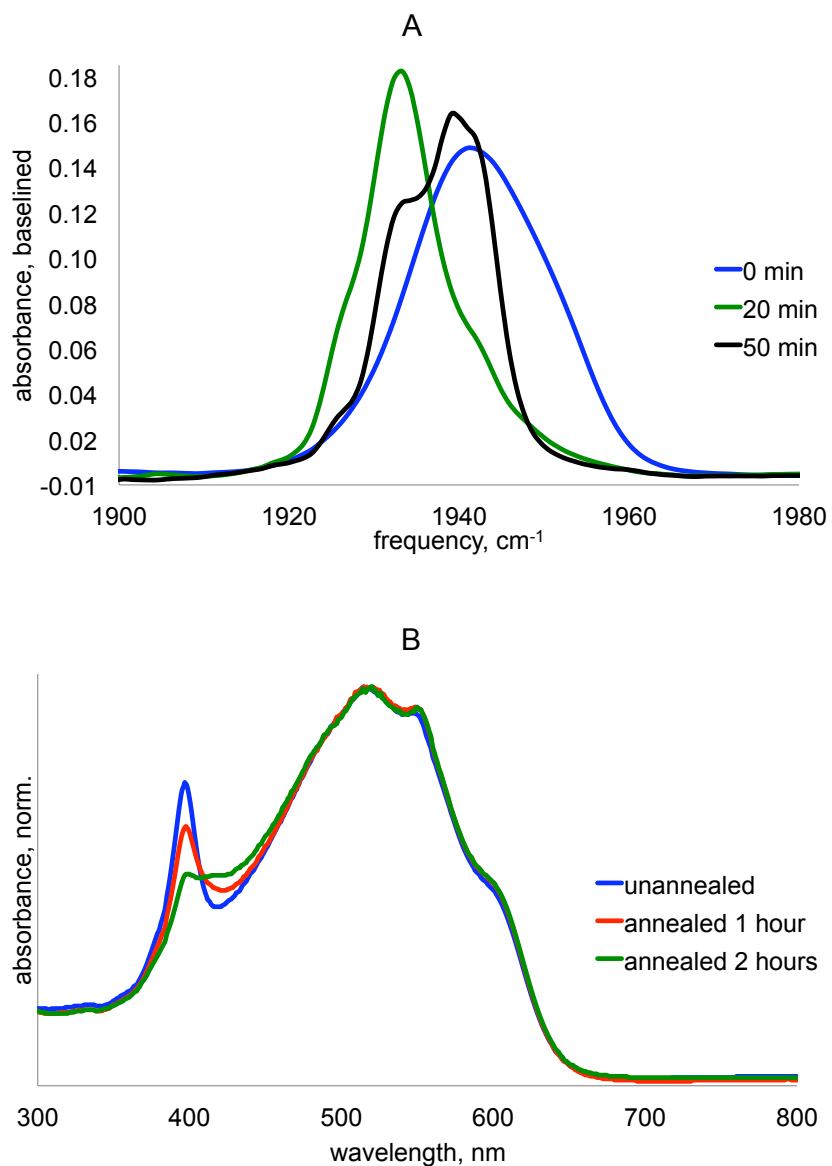


Figure 2.14: (A) FTIR Spectra of a 1:10 weight ratio RuOEP:P3HT film with a 1:7 mole ratio RuOEP: pyridine annealed in chloroform vapors. (B) UV-visible spectra of a 1:10 RuOEP:P3HT, with pyridine binding of the porphyrin, during annealing in solvent vapors.

## 2.5. Conclusion

Phase morphologies in blended organic materials must be controlled to achieve optimal device performance. In this work it has been demonstrated that microscopic and spectroscopic handles can provide complementary information that can be used to accurately characterize the phase segregation process in blended films of P3HT and RuOEP. It is found that porphyrin aggregation is avoided during annealing at sufficiently low concentrations of RuOEP. This implies that a blended P3HT/RuOEP photoanode could be prepared in a way that yields the benefits of annealing the polymer, but avoids the detrimental photophysics of porphyrin aggregation. In blended films with higher concentrations of RuOEP, solvent vapor annealing produces dynamic spectral changes in the CO symmetric stretching mode and the Soret absorption band of the porphyrin. TEM images confirm the segregation of the P3HT and RuOEP species into microscopic domains. All of the methods applied here suggest that the aggregation state of RuOEP in the films is increased as the films are annealed by solvent vapor. During the early stages of RuOEP aggregate formation, the data indicate that the CO transition dipole moments are aligned in a head-to-tail fashion leading to a narrow exciton band, but this ordering is lost at longer annealing times. It is possible that longer annealing times result in quasi-1D RuOEP assemblies that are connected by bridging CO ligands. Throughout this process, the ruthenium-bound CO provides a particularly sensitive spectroscopic handle of the annealing progress that enables us to describe a molecular-level picture of the porphyrinic interactions in the formed aggregates. This level of morphological control is an important feature to build into films that are to be controllably annealed. Furthermore, the inclusion of a sensitive IR

chromophore, such as the metal-bound CO, which could be introduced on many metallated porphyrin species, enables the chemical environments in the blend to be monitored in-situ during the annealing process.<sup>a</sup>

---

<sup>a</sup> The authors gratefully acknowledge funding from the Donors of the American Chemical Society Petroleum Research Fund for partial support of this research (46628-G6). We also acknowledge the 3M Corporation Nontenured Faculty Award, a Grant-in-Aid from the University of Minnesota, Twin Cities, and partial support by the National Science Foundation under CHE-0847356. TEM measurements were performed at the University of Minnesota Characterization Facility, which receives support from the NSF through the NNIN. AAE thanks the Blank research group at the University of Minnesota, Twin Cities, for assistance with photoluminescence measurements.

## Chapter 3

# 2D-IR Studies of Annealing-Induced Changes to Structural Dynamics in Organic Semiconductor Thin Films

Reproduced in part with permission from:

Audrey A. Eigner, Timothy C. Anglin, and Aaron M. Massari. 2D-IR Studies of Annealing – Induced Changes to Structural Dynamics in Organic Semiconductor Thin Films. *Journal of Physical Chemistry C*. **2010**, 114, pp. 12308 – 12315.

Copyright, 2010 American Chemical Society.

### 3.1. Chapter Summary

In this chapter, polymer dynamics in blended films of P3HT and RuOEP are examined with 2D-IR vibrational echo spectroscopy. Solvent vapor annealing generates three unique structural states in the films, previously discussed in Chapter 2, for electrical and spectroscopic characterization. The field-effect hole mobilities of the unannealed films are unaffected by the presence of the RuOEP guest species, and comparable mobility increases are observed during the early stages of the annealing process. The FTIR spectrum of the CO symmetric stretch exhibits dramatic changes over the course of annealing, indicating that substantial changes occur in the surrounding chemical environments in the P3HT film. During the early annealing steps, the 2D-IR VES measurements indicate a loss of dynamics on the time scale of 400 femtoseconds, concurrent with annealing-induced hole mobility improvements. These results are cast in light of several recent theoretical studies that predict that structural dynamics can have a profound influence on charge carrier mobilities.

## 3.2. Introduction

Charge mobilities for amorphous and semicrystalline organic materials rarely exceed  $0.5 \text{ cm}^2/\text{Vs}$ , and typically fall orders of magnitude short of the mobilities required for device applications.<sup>22,23,66</sup> The conduction efficiencies of newly synthesized organic materials can often be improved to approach this mobility limit by synthetic modifications to their molecular structures to enhance packing and orbital overlaps,<sup>1-3</sup> and by post-processing treatments such as annealing.<sup>18,133,153-158</sup> Over the past decade, the effects that these variables have on charge mobilities have been investigated extensively in the interest of achieving mobilities that consistently surpass the  $0.5 \text{ cm}^2/\text{Vs}$  metric. However, the performance enhancements have been incremental and continue to approach this ceiling value asymptotically. It seems that current approaches to improving organic electronic materials have reached an upper-bound for optimizing charge mobilities and the next performance breakthrough may have to come from an unexplored direction of research.

For amorphous materials, which generally conduct via a charge hopping mechanism,<sup>56,159</sup> the onset of the organic ceiling mobility implies a hopping time scale that coincides with a range of low frequency structural motions. Such a coincidence of time scales has been predicted to have important consequences for the rates of site-to-site charge transfer.<sup>25-30,56,83,160,161</sup> For hopping domain charge transport, as viewed from a dynamic perspective, localized charges must navigate a convoluted energy landscape whose peaks and valleys undulate with time. These stochastic thermal fluctuations not only provide the energy for successful hopping events, but also lead to a time dependence of barrier heights on the ultrafast time scale (femtoseconds to picoseconds).

It should be appreciated that the structural, and therefore energetic, memory is not retained even in solid-state films, as it is at least partially washed out by nuclear rearrangements and structural dynamics. Stated differently, the energetic experience for sequential charges following identical trajectories through an organic film must be different.

The effects that molecular motions or structural dynamics have on charge mobilities have been explored by theoretical modeling of charge transport using dynamics simulations,<sup>25-30,56,83,160,161</sup> and demonstrate that charge conduction is inherently related to time-dependent intra- and intermolecular electronic couplings. In condensed phase systems the experimental extraction of dynamical information from linear absorption spectra is not possible, as the homogeneous lineshapes are completely concealed under broad inhomogeneous absorption bands. However, 2D-IR VES has emerged as a method that can recover ultrafast chemical dynamics from an inhomogeneous distribution of environments.<sup>162-166</sup> The dynamical processes that lead to homogeneous lineshape broadening within sub-ensembles of IR-active chromophores are the same structural fluctuations that modulate the energy landscape experienced by hopping charges. Therefore, by quantifying the time scales of structural motions in polymer films with varied electrical properties, 2D-IR spectroscopy could be used to experimentally correlate dynamics and mobilities.

In this chapter, spectrally resolved, homodyne detected 2D-IR VES was employed to examine blended films of poly(3-hexylthiophene-2,5-diyl) (P3HT) with a carbonyl-containing ruthenium porphyrin (RuOEP) before and after a solvent vapor annealing treatment that is known to improve hole mobilities in the polymer.<sup>18,133,155,156,158</sup> In



Chapter 2, it was shown that phase segregation of the two components can be controlled during this annealing process to generate several different microenvironments as the polymer regions become more crystalline and the porphyrin molecules begin to aggregate.<sup>167</sup> Here, the dynamics experienced by the ruthenium-bound CO vibrational mode that serves as a reporter of the time dependent changes in its surrounding solid state organic environment are measured. Three different microstates were trapped in the solid-state films and examined by 1D and transmission electron microscopy (TEM). Two of the three microstates were examined with 2D-IR VES. Concurrently, the hole-mobilities for films in these same annealed states were measured in an effort to relate the changes in dynamics back to changes in electrical performance.

### **3.3. Experimental**

#### **3.3.1. Materials**

Electronic grade 97% regioregular poly(3-hexylthiophene-2,5-diyl) (P3HT) (50,000 M<sub>w</sub>) was used as received from Rieke Metals Inc. and 2,3,7,8,12,13,17,18-octaethyl-21*H*,23*H*-porphine ruthenium(II)carbonyl (RuOEP) was used as received from Sigma-Aldrich. All solvents were reagent grade and were used as received without further purification.

#### **3.3.2. Thin Film Preparation**

A 1:10 mass ratio blend of RuOEP to P3HT was prepared by adding 3 mL of chloroform to 200 mg of P3HT and 20 mg of RuOEP in a small glass vial. Solutions of P3HT without RuOEP were also prepared at the concentration of 200 mg of P3HT per 3 mL of chloroform for hole mobility measurements (see below). The solutions were stirred for 15 minutes at 45 °C and then filtered through a 0.45 μm syringe filter to

remove particulates. A 700  $\mu\text{L}$  aliquot of solution was then spin-coated at 400 rpm for 2 minutes onto a 1 inch  $\text{CaF}_2$  window. The films were then dried for at least several hours and stored in a dark container under a flowing dry nitrogen atmosphere. FTIR spectra taken of these films before and after exposure to high vacuum conditions ( $<1 \times 10^{-6}$  Torr for 24 hours) indicated no residual solvent molecules, however, it is conceivable that imperceptible quantities of chloroform remain trapped within the polymer matrix. Solvent vapor annealing was performed with chloroform vapors as described previously<sup>167</sup> and the FTIR spectra were measured in-situ to monitor the annealing progress. FTIR spectra were collected (Thermo Electron Nicolet 6700) as an average of 16 scans at a resolution of  $1 \text{ cm}^{-1}$ . TEM was performed at the University of Minnesota Characterization Facility on a JEOL 1210 at 120 kV. Sample solutions were prepared and mounted onto 400 mesh, copper TEM grids (Ted Pella) as described previously.<sup>167</sup>

### 3.3.3. Field-effect Mobility Measurements

Field effect transistors (FETs) were prepared in a bottom-contact geometry from freshly prepared polymer solutions by spinning the films onto substrates onto which the source, gate, and drain contacts were previously deposited. The FET channel dimensions were 1 mm long and 2 mm wide. Prior to the deposition of the P3HT and RuOEP/P3HT films, the wafer was immersed overnight in hexamethyldisilazane (HMDS) (Sigma-Aldrich), rinsed in ethanol, and dried with  $\text{N}_2$  in order to minimize trap density at the  $\text{SiO}_2$  interface.<sup>168,169</sup> As such, the dielectric in these devices is HMDS coated  $\text{SiO}_2$ . Electrical characterization was performed with two Keithley 617 electrometers configured as source-measure units. The output and transfer characteristics were determined for each FET device in the unannealed state and at each

of the two solvent vapor annealed states.<sup>167</sup> The annealing was performed as described above, and the extent of annealing was monitored by FTIR spectroscopy of an additional thin-film sample prepared on a CaF<sub>2</sub> substrate and located in the annealing chamber with the FET devices. The hole mobilities ( $\mu$ ) were determined from the transfer characteristics collected in the linear regime with a source-drain bias ( $V_{SD}$ ) of 10 V.<sup>56,59</sup> Five different RuOEP/P3HT devices and five different P3HT devices were analyzed, and the same ten devices were carried through each of the annealing steps to identify mobility trends.

#### **3.3.4. 2D-IR VES**

A titanium sapphire (Ti:Sapph) oscillator (Kapteyn-Murnane Laboratories) was pumped by a frequency-doubled continuous-wave neodymium vanadate laser (Spectra-Physics, Millennia 5W) to generate mode-locked pulses centered at 800 nm with 50 nm of bandwidth and 3 nJ of power per pulse. These pulses were used to seed a regeneratively amplified Ti:Sapph laser (Spectra-Physics, Spitfire-Pro) pumped by a diode-pumped Q-switched neodymium yttrium lithium fluoride (Nd:YLF) laser (Spectra-Physics, Empower 15) to produce amplified 1.2 mJ pulses at 1 kHz. Half of the total power generated from the amplifier system (600 mW) was then used to pump an optical parametric amplifier (OPA) (Spectra-Physics, OPA-800C). The near IR signal and idler beams generated by a  $\beta$ -barium borate (BBO, 3 mm thick) crystal in the OPA were difference frequency mixed in a silver gallium sulfide crystal (AgGaS<sub>2</sub>, 0.5 mm thick) to generate 3-4  $\mu$ J mid-IR pulses. The final output pulses were centered at the CO symmetric stretching frequency in RuOEP and had a temporal duration of 90 fs and approximately 200 cm<sup>-1</sup> of bandwidth (1.2 times the transform limit). The pulse

durations were characterized prior to each experiment by second-order autocorrelation in a type I AgGaS<sub>2</sub> crystal.

For the 2D-IR VES experiments, the mid-IR beam was split into three roughly equal intensity beams for use in the 2D-IR excitation sequence and one weak beam (1-2 %) that served to locate the generated vibrational echo signal. Each of the three pump beams transmitted through only one 5 mm ZnSe optic during the splitting process. An off-axis parabolic reflector crossed and focused the three excitation pulses in the sample in the BOXCARS geometry<sup>170</sup> with the third order signal being generated in the phase matched direction. The three pulses were temporally overlapped by optimizing the non-resonant third-order signal from a 50  $\mu\text{m}$  thick carbon tetrachloride sample. The vibrational echo signals were spectrally resolved in a 0.32 meter monochromator (Horiba Jobin Yvon, iHR320) and detected with a liquid N<sub>2</sub> cooled indium antimonate (InSb) detector (Infrared Associates, Inc). The spectral resolution of the detection system is 0.6  $\text{cm}^{-1}$ , but resolutions of 2  $\text{cm}^{-1}$  were typically used for echo measurements to improve the signal-to-noise ratio. The entire optical system was purged with dry CO<sub>2</sub>-free air during data collection. An IR polarizer was used to attenuate the intensity of the IR beams (prior to beamsplitting) to avoid sample damage, and all data in this study were collected with the laser power diminished to the lowest power that could still achieve a reasonable signal-to-noise ratio (typically 0.3  $\mu\text{J}$  per pulse in each beam). Over the range of powers tested, no power dependence was observed for the samples in this work.

The spectrally resolved vibrational echo technique has been described in detail elsewhere and is a homodyne detected form of 2D-IR spectroscopy (one dimension is

the time, or  $\tau$ , axis of the vibrational echo decays and the other is frequency as resolved by the monochromator).<sup>40,105,115,171</sup> Briefly, the time delay between pulses 1 and 2,  $\tau$ , was scanned as the time delay between pulses 2 and 3,  $T_w$ , remained fixed to obtain vibrational echo decay curves at each frequency. To cancel scatter from these heterogeneous solid-state samples, the exact timing of the scanning pulse was randomly varied by a fraction of a wavelength of light at each point and many scans were averaged. This decreased the temporal resolution by 8-9 fs. Multiple echo decays were measured at five  $T_w$ s for each sample at several frequencies across the inhomogeneous lineshape. The echo decays were normalized and fit to a single frequency-frequency correlation function (FFCF) having a multiple exponential plus a constant offset form. The full details of the fitting procedure were described in the introductory chapter. The FFCF was deemed accurate when it successfully reproduced the vibrational echo decays at all  $T_w$ s at all frequencies and also reproduced the linear lineshape. The lifetimes of the CO vibrations in these calculations were directly measured using transient grating experiments.<sup>113,146,172</sup>

### 3.3.5. Pump-Probe Spectra

For pump-probe measurements, the mid-IR beam (described in the preceding section) was split into two beams: one strong beam for use in as the pump (99 %) and one weak beam (1-2 %) that served as the probe. An off-axis parabolic reflector crossed and focused the two beams in the sample, and the time delay between the pulses was set at 0.5 ps. The probe was then spectrally resolved in a 0.32 meter monochromator and detected with a liquid N<sub>2</sub> cooled indium antimonate (InSb) detector.

## 3.4. Results and Discussion

### 3.4.1. Characterization of Annealed States

In Chapter 2, the dramatic spectral changes exhibited by the ruthenium-bound CO ligand during the solvent vapor annealing process in blends of P3HT and RuOEP were reported, and categorized into three distinct states referred to as unannealed, half-annealed, and fully-annealed.<sup>167</sup> The FTIR spectra of these states are shown in Figure 3.1. The spectrum of the unannealed state is characterized by a broad peak (17  $\text{cm}^{-1}$ , FWHM) centered at 1932  $\text{cm}^{-1}$ . After approximately 20 min in a saturated chloroform vapor environment this peak red-shifts to 1927  $\text{cm}^{-1}$  and narrows to approximately 7  $\text{cm}^{-1}$  (FWHM). Following this half-annealed state, the peak at 1927  $\text{cm}^{-1}$  diminishes and splits into a broader red-shifted band centered at 1919  $\text{cm}^{-1}$  (10  $\text{cm}^{-1}$ , FWHM) and a small blue-shifted peak centered at 1946  $\text{cm}^{-1}$ . This fully-annealed state occurs after approximately 70 min in a saturated solvent environment.

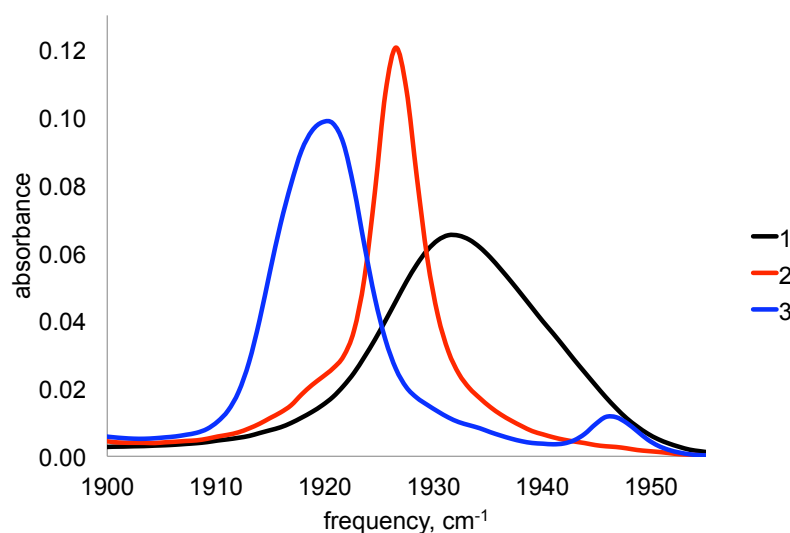


Figure 3.1: Baselined FTIR spectra of the CO symmetric stretching mode on RuOEP embedded into P3HT thin films at the (1) unannealed, (2) half annealed and (3) fully annealed stages.

During these spectral changes we have noted some evidence of phase segregation between the unannealed and fully-annealed states.<sup>167</sup> To corroborate this evidence, Figure 3.2 shows the TEM images for representative samples at all three states of the solvent vapor annealing process. In these micrographs, the ruthenium center of RuOEP is a strong electron scatterer leading to dark regions wherever there are high concentrations of this molecule. Consistent with Chapter 2, the unannealed RuOEP/P3HT films (Figure 3.2A) appear to have the RuOEP homogeneously blended into the P3HT matrix, whereas the fully-annealed blends (Figure 3.2C) undergo phase segregation into large aggregates of RuOEP. The TEM image of the half-annealed state (Figure 3.2B) looks very much like the unannealed sample, suggesting that phase segregation is as minimal as it is in the unannealed sample. The FTIR spectra for these samples were also collected prior to imaging and are shown to the left of each image to verify the annealed states of the films that were imaged.

In this work, an understanding of the changes in molecular dynamics of the semiconducting polymer, P3HT, as it is progressively annealed in solvent vapors is sought. These dynamics were measured by using 2D-IR VES to monitor the frequency fluctuations experienced by the CO ligands on embedded RuOEP in response to time dependent changes in their local electrostatic environments. This approach has been shown to be a valid representation of the dynamics of proteins,<sup>40,105,115,173,174</sup> liquids,<sup>50,88,175-178</sup> and solids state glasses,<sup>100,105,179,180</sup> and is not unlike attaching a fluorescent probe to an enzyme to measure its activity<sup>181,182</sup> or introducing an imaging contrast agent to a cell to visualize a chemical process in-vivo.<sup>183-185</sup> Accordingly, the same underlying questions arise regarding the perturbation of the probe species on the

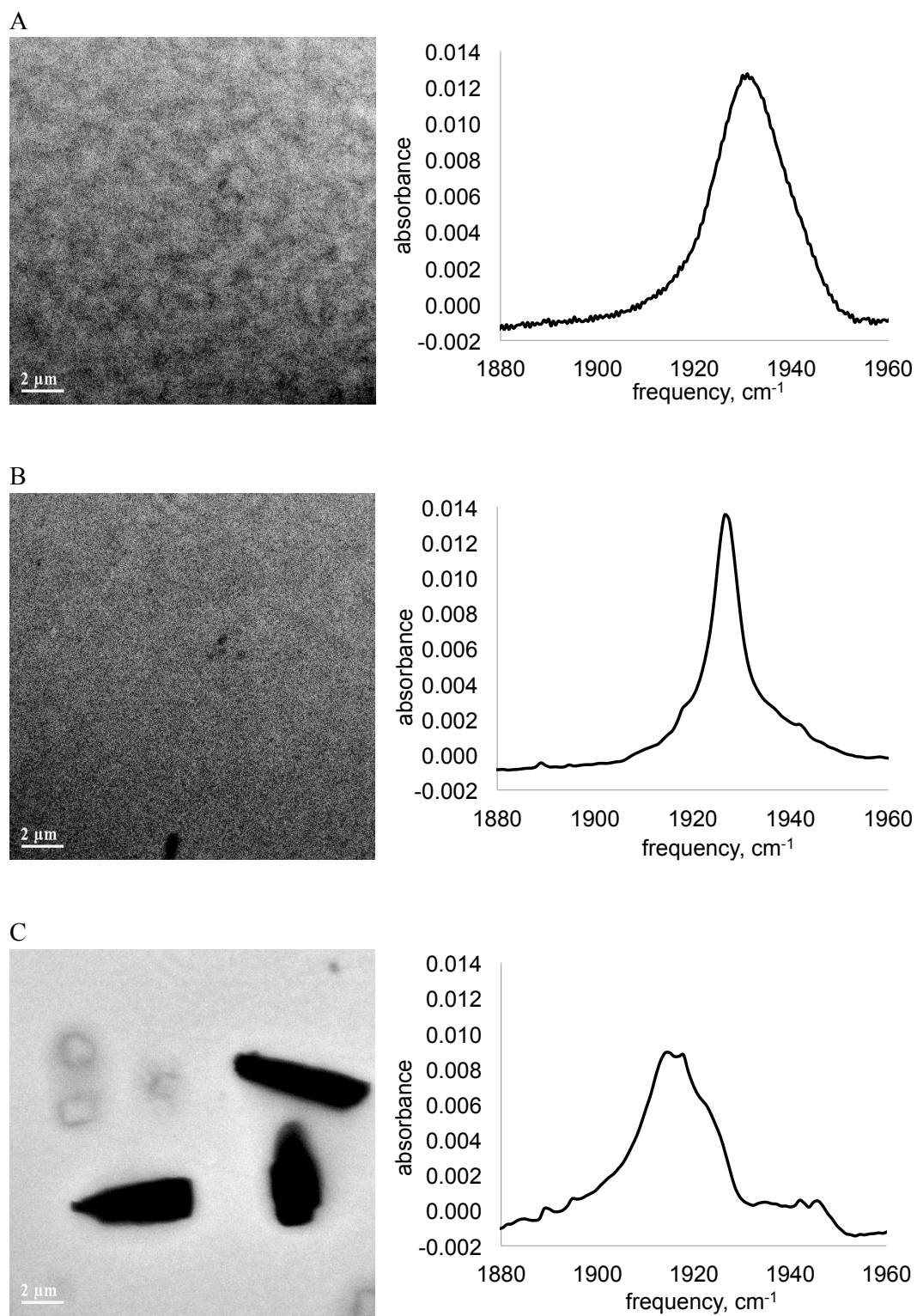


Figure 3.2: TEM images of (A) unannealed, (B) half annealed and (C) fully annealed RuOEP:P3HT films during the solvent vapor annealing process. Also shown, to the left of each image, are the corresponding FTIR spectra taken from these same films.



behavior of the system of interest. To evaluate the level of this perturbation for the RuOEP/P3HT materials in this work, the electrical properties of these blended films were characterized and compared to thin films prepared without the RuOEP reporter species.

### 3.4.2. Mobility of Annealed States

Using a sample preparation identical to that used to produce the blended films used in the dynamics measurements below, P3HT and RuOEP/P3HT FETs were fabricated for testing the electrical responses of the two systems. The details of FET operation can be found elsewhere.<sup>59</sup> The advantage of this approach in this case is that the semiconductor is only temporarily doped in the vicinity of the SiO<sub>2</sub>, without resorting to chemical doping of the entire film, which drastically alters the film morphology. Thus, a measure of field-effect carrier mobilities in the films as prepared for the dynamics studies below was obtained.

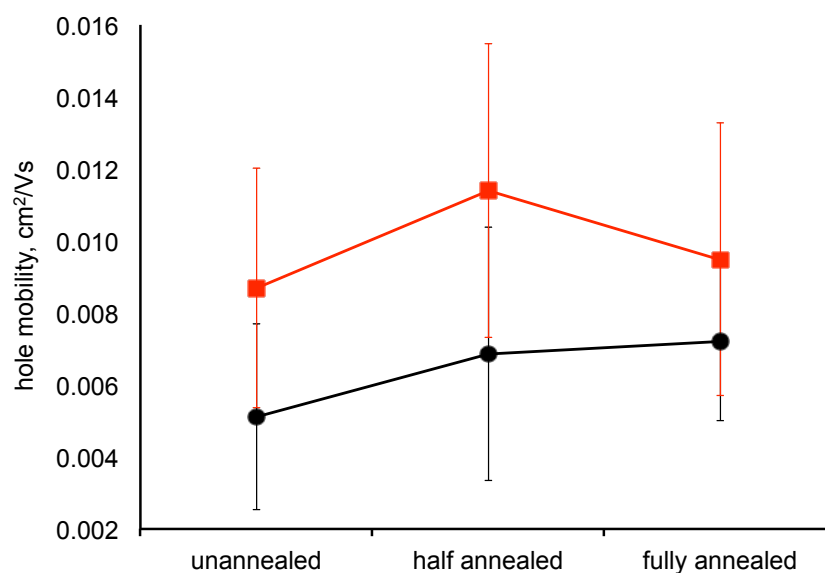


Figure 3.3: Field-effect hole mobilities extracted in the linear regime for FETs prepared with pure P3HT (circles) and RuOEP:P3HT blends (squares). The error bars represent the standard deviations for each data point over five samples.

Figure 3.3 plots the field-effect hole mobilities measured for several P3HT and RuOEP/P3HT blends in the FET linear regime at the three relevant states of solvent vapor annealing.<sup>59</sup> For the unannealed samples, the charge carrier mobilities were found to be the same between the pure and blended films within the error bars of the measurements ( $5.1 \times 10^{-3} \pm 2.6 \times 10^{-3} \text{ cm}^2/\text{V}\cdot\text{s}$  and  $8.7 \times 10^{-3} \pm 3.3 \times 10^{-3} \text{ cm}^2/\text{V}\cdot\text{s}$  for pure P3HT and RuOEP/P3HT blends, respectively). The uncertainties on these measurements are the standard deviations from the mean for a series of five different P3HT or five different RuOEP/P3HT devices. Furthermore, it was found that there is no clear influence of the RuOEP guest on the FET threshold voltage required to turn these devices on (not shown), which is evidence that the density of charge trap states and defects are comparable.<sup>186,187</sup> Therefore, it can be concluded for the unannealed samples that the inclusion of the RuOEP vibrational dynamics reporter has no significant effect on the electrical performance of the materials.

As the P3HT and RuOEP/P3HT films were annealed in chloroform vapors to the half-annealed state, notable increases in their respective hole mobilities to approximately 30% greater than their unannealed values (up to  $6.9 \times 10^{-3} \pm 3.5 \times 10^{-3} \text{ cm}^2/\text{V}\cdot\text{s}$  and  $1.1 \times 10^{-2} \pm 4.1 \times 10^{-3} \text{ cm}^2/\text{V}\cdot\text{s}$  for pure P3HT and RuOEP/P3HT blends, respectively) were measured. This is consistent with literature reports for mobility improvements upon thermal or solvent vapor annealing of P3HT films.<sup>18,133,153-158</sup> The improvement is ascribed to an increase in order and crystallinity that occurs within the films as solvent vapors solvate the P3HT and RuOEP molecules, imparting structural mobility that allows them to rearrange and pack with a greater degree of pi-orbital

overlap. This demonstrates that the change in electrical performance during this morphological transition is unaffected by the presence of the RuOEP species.

As the samples were further annealed to the fully-annealed state, Figure 3.3 shows that the charge carrier mobilities did not improve noticeably for the P3HT films while the RuOEP/P3HT blends decreased to about 9% over their unannealed values (ending at  $7.2 \times 10^{-3} \pm 2.2 \times 10^{-3} \text{ cm}^2/\text{V}\cdot\text{s}$  and  $9.5 \times 10^{-3} \pm 3.8 \times 10^{-3} \text{ cm}^2/\text{V}\cdot\text{s}$  for pure P3HT and RuOEP/P3HT blends, respectively). Although the fully-annealed mean hole mobilities are not significantly different for these two samples, we note that the mobility trends were consistent across all five devices measured for each sample type. It has been reported that annealing of pure P3HT films improves their performance initially, but reaches a limit where no further improvement is measured, as seen in the pure P3HT devices sampled in Figure 3.3.<sup>155,158,188</sup> Likewise, the mobility of the P3HT phase in organic blends, such as the RuOEP/P3HT samples studied here, typically exhibit mobility improvements followed by a period of degradation due to severe phase segregation.<sup>17,18,120,157</sup> This is consistent with the electrical characterization of the RuOEP/P3HT devices annealed in Figure 3.3, and corroborates the phase segregation observed in Figure 3.2C. Therefore, it can be concluded from these measurements that the mobilities of the blended RuOEP/P3HT materials behave as the pure P3HT films during the transition to the half-annealed state, but exhibit performance differences during the final stage of annealing that reflect the phase segregation of the two species. For this reason, the 2D-IR studies below focus on the dynamical changes that accompany the unannealed to half-annealed transition.

### 3.4.3. 2D-IR VES of Unannealed and Half-annealed States

The electrical characterization supports a model in which the vibrational dynamics probe (the CO bound to RuOEP) serves as a spectator to its P3HT surroundings without significantly altering them during the transition to the half-annealed state with a 30% higher hole mobility. The purpose of this study was to measure the changes in molecular dynamics that accompany these annealing-induced changes via 2D-IR VES on the ruthenium-bound CO of the porphyrin. The three IR spectra shown in Figure 3.1 represent three stages in the annealing process during which the charge mobilities of the RuOEP/P3HT film increase and then diminish (see Figure 3.3). Beneath each of the inhomogeneously broadened lineshapes are many sub-ensembles corresponding to a distribution of different chemical environments solvating the ruthenium-bound CO ligands. The CO vibrational frequencies within any one of these chemical environments are not static, but are continuously modulated by fluctuations of the surrounding medium, in this case, the structural dynamics of P3HT. 2D-IR VES recovers these underlying dynamics by measuring the time evolution of coherent quantum mechanical states. The technique incorporates a three pulse sequence in which the first IR pulse creates a coherently resonating collection of ruthenium-bound CO oscillators. All of these excited oscillators have their own unique solvation environments in the P3HT film, giving rise to a range of instantaneous vibrational frequencies (spectral inhomogeneity). Changes in the nuclear positions of the surrounding polymer due to structural dynamics continuously modulate all of these instantaneous frequencies (homogeneous broadening). The combination of these inhomogeneous and homogeneous processes cause the macroscopic polarization

induced by the first pulse to rapidly decay (within a ps) due to destructive interference between the microscopic fields emitted by each CO oscillator. Many of these CO ligands are still vibrating and may continue to do so for tens of ps, but the phase relationships between the oscillators have been scrambled.

After a time delay,  $\tau$ , the second IR pulse arrives at the sample to convert some of the dephased oscillators to their excited or ground state populations where the degree of dephasing is momentarily stored for time periods that can exceed one vibrational lifetime (typically 15-20 ps). During this period following the second IR pulse,  $T_w$ , the ground and excited state vibrational energy levels continue to fluctuate as the surrounding solvation environment of the P3HT continues to fluctuate. However, relatively fast frequency perturbations that do not change the average frequency of a given sub-ensemble during the  $T_w$  period have no effect on the phase relationships of the oscillators that were stored in population states. On the other hand, slower perturbations that shift the average ensemble frequency on time scales comparable to the length of the  $T_w$  period will lead to additional homogeneous dephasing. The third pulse initiates a process that causes the microscopic polarizations emitted from the surviving CO oscillators to rephase and recover a fraction of the initial macroscopic polarization generated by the first pulse. This rephased coherence emits a fourth pulse that is referred to as the vibrational echo, the intensity of which is measured as a function of  $\tau$  while the  $T_w$  delay is held constant to obtain a vibrational echo decay curve.

For a given sample the vibrational echo decays are collected at several  $T_w$ s and multiple spectrally resolved frequencies. The individual decays provide qualitative

information about the rates of pure dephasing, which are driven by molecular motions in the system. They provide information about the fastest structural motions that occur on time scales up to a few picoseconds. By collecting vibrational echo decays at different  $T_w$ s the slower structural motions that lead spectral diffusion are sampled. Spectral diffusion is qualitatively observed as an increase in the vibrational echo decay rate and a decrease in the peak shift of the decay curve towards the origin as  $T_w$  is increased. In the limit that all dynamics have occurred on all time scales the vibrational echo peak shift will be zero. However, this limit is typically not observed for 2D-IR VES measurements on solid state samples due to static inhomogeneity and molecular dynamics that occur on time scales significantly longer than the vibrational lifetime of the reporting vibration.

This discussion focuses on a comparison between the homodyne-detected 2D-IR data for the unannealed and half-annealed states since the fully-annealed state was shown above to be phase-segregated and the 2D-IR data likely reflect the dynamics of RuOEP aggregates rather than P3HT. Figure 3.4A shows a comparison of the echo decays collected at  $T_w$ s of 0.5 and 15 ps for the unannealed state measured at  $1932\text{ cm}^{-1}$ . The data exhibit pronounced oscillations that are well understood to be accidental degeneracy beats caused by the spectral overlap of the 1-2 vibrational transition with the 0-1 transition.<sup>189</sup> The bandwidth of the excitation pulses spans the anharmonicity of the CO oscillator leading to a finite probability of exciting higher order transitions. In this case, the 1-2 emission spectrum is sufficiently broad to overlap with the 0-1 echo spectrum at the selected frequency, leading to periodic interference at the frequency of the vibrational anharmonicity. As  $T_w$  is increased from 0.5 ps to 15 ps, the vibrational

echo signal decays faster with a minimal peak shift towards the origin. This indicates that a small amount of spectral diffusion occurs for the ruthenium-bound CO in response to structural motions in the polymer film on the time scale of tens of picoseconds. The observation that the echo decay peak has not reached zero by 15 ps is evidence of some static inhomogeneity or polymer dynamics that occur on time scales so slow they are outside the sampling range of this technique. However, the molecular dynamics that occur within tens of picoseconds are those that we are most interested in characterizing here, as they occur on time scales similar to charge hopping events.<sup>24,66</sup>

Figure 3.4B shows a comparison of the echo decays collected at  $T_w$ s of 0.5 ps and 15 ps for the half-annealed state measured at  $1927\text{ cm}^{-1}$ . These decays show less intense beating than those of the unannealed films and a pronounced peak shift from 0.65 ps to 0.3 ps with increasing  $T_w$ s. Because the inhomogeneously broadened linear spectrum of the half-annealed sample is much narrower than that of the unannealed sample, the overlap between the 0-1 and 1-2 energy states is smaller. Assuming a similar anharmonicity, this leads to less accidental degeneracy beating.<sup>189</sup> At first glance, the large peak shift in the half-annealed sample data, typically ascribed to greater inhomogeneity, is surprising in light of the narrow inhomogeneously broadened linear lineshape. However, this simply reflects the inability of the linear observation to predict the molecular dynamics of the system. One dynamical explanation for the peak shift in Figure 3.4B is that a drastic decrease in the time scales of frequency fluctuations has occurred, pushing some of the dynamics into the motionally-narrowed regime.<sup>49,190,191</sup> Motional narrowing occurs when the modulation time,  $\tau_m$ , is much larger than the inverse amplitude of the modulation,  $\Delta_m$ . It can be understood to be the

point at which the dynamics become so fast that their effects on the oscillating vibrational modes are essentially averaged out. Motionally-narrowed dynamics would be manifest as large vibrational echo peak shifts at all  $T_w$ s, but a narrow linear lineshape. Clearly, there is a need to quantify the dynamic parameters contained in these data before conclusions can be drawn.

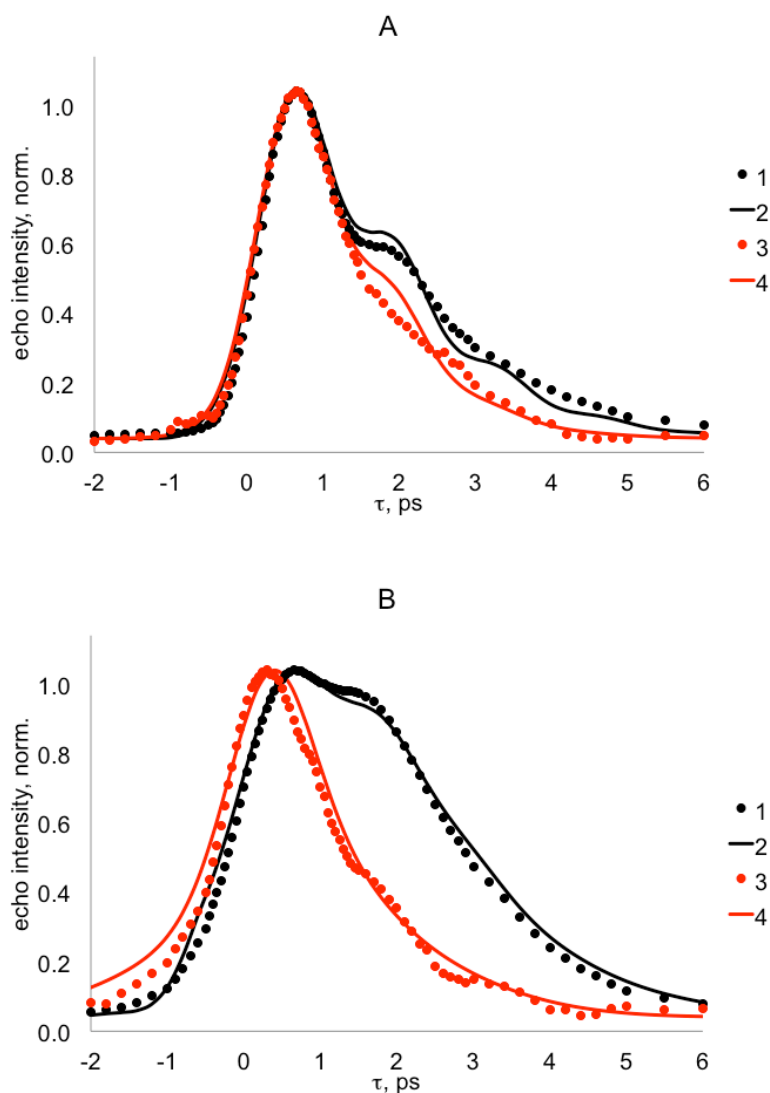


Figure 3.4: Spectrally resolved 2D-IR VES decays collected for RuOEP:P3HT blends in the (A) unannealed at  $1931\text{ cm}^{-1}$  and (B) half annealed state at  $1925\text{ cm}^{-1}$ . In both frames, the decays are shown at  $T_w = 0.5\text{ ps}$  [1] [2] and at  $T_w = 15\text{ ps}$  [3] [4]. Experimental data are depicted as markers and calculated best fits are overlaid as solid lines.



### 3.4.3. Pump-Probe Spectra of RuOEP in Different Solvents

In order to determine if the CO vibrational modes of the porphyrin molecules couple differently in distinctive sub-environments within the blended films, the pump-probe spectrum (Figure 3.5) of RuOEP in three different solvents were taken. Thiophene, 3-hexylthiophene and hexanes were chosen in order to examine the porphyrin in solvents that mimic the chains and rings of the P3HT backbone. In these spectra, the 0-1 transition is seen as a positive feature and the 0-2 transition is seen as a negative feature. Upon evaluation, the anharmonicity of the vibration in each of the three solvents is similar:  $24\text{ cm}^{-1}$  in hexanes,  $25\text{ cm}^{-1}$  in 3-hexylthiophene, and  $17\text{ cm}^{-1}$  in thiophene. This suggests that there is not a significant coupling of one sub-environment over another.

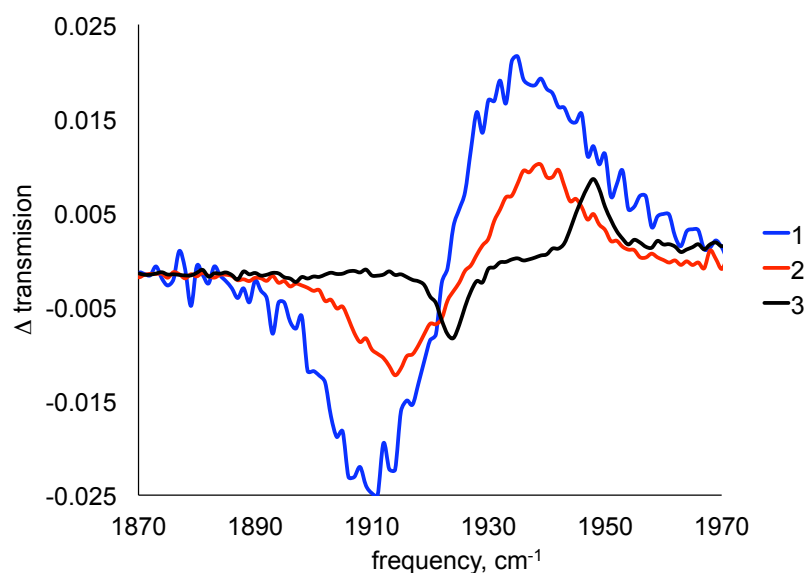


Figure 3.5: Pump-probe spectra of RuOEP dissolved in (1) thiophene, (2) 3-hexylthiophene and (3) hexanes.

### 3.4.5. Frequency-Frequency Correlation Function

The 2D-IR VES and FTIR data for each annealed state were collectively fit to a frequency-frequency correlation function (FFCF) with the bi-exponential form shown in Equation 3.1 using non-linear response theory.<sup>114</sup>

$$FFCF(t) = \Delta_0^2 + \sum_1^2 \Delta_i^2 \exp\left(\frac{-t}{\tau_i}\right) \quad (3.1)$$

The complete data sets (echo decays at all  $T_{ws}$  and all frequencies, plus the linear FTIR spectrum) were simultaneously fit with these FFCFs, which describe the dynamics leading to a loss of correlation between the starting frequencies of oscillators in a sub-ensemble and their frequencies at some later time,  $t$ . In this equation,  $\Delta_i$  is interpreted as the amplitude of a dynamic process or frequency perturbation having a time scale of  $\tau_i$ , and  $\Delta_0$  represents static inhomogeneity and polymer dynamics that occur on time scales longer than several vibrational lifetimes ( $>100$  ps). The full details of the fitting procedure is discussed in the introductory chapter (Section 1.3.3.).

The FFCF fitting parameters for the 1D- and 2D-IR data from the unannealed and half-annealed states are compiled in Table 3.1. Consistent with our previous work, the linear FTIR spectrum of the three samples each requires multiple Gaussian transitions to be properly fit.<sup>167</sup> The data from each of the three annealed states were fit using the two largest amplitude vibrational transitions with center frequencies matching those reported previously and each having an independent FFCF. To demonstrate the quality of these fits, the calculated vibrational echo decays for the unannealed and half-annealed samples at  $T_{ws}$  of 0.5 and 15 ps are overlaid (solid lines) with the experimental data in Figures 3.4A and 3.4B. The fits simultaneously reproduce the linear and non-

linear data very well at all  $T_{ws}$  and multiple frequencies (all fits and experimental data at all  $T_{ws}$  and all frequencies are provided in the Figures 3.6 and 3.7). For the unannealed RuOEP/P3HT film the two dominant time scales of dynamic components of the FFCFs are 400 fs and greater than 100 ps for both of the transitions (see Table 3.1). The long time scale dynamic components in these FFCFs are very slow, consistent with the minimal peak shift noted in Figure 3.7A, however their dynamics are necessary to fit the accelerated echo decays at longer  $T_{ws}$ . Combining these parameters with the  $\Delta_0$ s of  $5.2 \text{ cm}^{-1}$  and  $6.9 \text{ cm}^{-1}$ , it can be concluded that the majority of the peak shift in that figure is the result of static inhomogeneity or very slow dynamics. It is noteworthy that the FFCF parameters for both transitions were floated independently during the fitting procedure, yet converged on very similar values in both FFCFs. This supports a model in which the two sub-ensembles that are present beneath the IR linear lineshape experience similar dynamic fluctuations, as would be expected if the primary source of these perturbations were the surrounding P3HT. The error bars on the fit parameters in this table represent the magnitude that each parameter can be varied while still recovering 99% of the squared fit residuals by iteratively varying the remaining parameters.

Table 3.1: FFCF parameters used to fit 2D-IR VES data in Figure 3.6 and 3.7.

FFCF parameters	Unannealed		Half-annealed	
	<i>transition 1</i>	<i>transition 2</i>	<i>transition 1</i>	<i>transition 2</i>
center frequency ( $\text{cm}^{-1}$ )	1931.2	1940.1	1927.5	1930.5
relative concentration	1	0.53	1	1.36
anharmonicity ( $\text{cm}^{-1}$ )	24.7	24.7	27	27
vibrational lifetime (ps)	17	17	14	17
$\Delta_0$ ( $\text{cm}^{-1}$ )	5.2 (+0.4/-0.4) <sup>a</sup>	6.9 (+0.8/-1.2)	---	---
$\Delta_1$ ( $\text{cm}^{-1}$ )	3.3 (+0.6/-0.3)	2.5 (+0.7/-0.6)	2.40 (+0.03/-0.04)	8.1 (+0.2/-0.3)
$\tau_1$ (ps)	0.4 (+0.2/-0.1)	0.4 (+0.4/-0.2)	29 (+3/-3)	55 (+6/-5)
$\Delta_2$ ( $\text{cm}^{-1}$ )	3.0 (+1.0/-0.9)	4.8 (+1.3/-1.5)	---	---
$\tau_2$ (ps)	162 (+232/-105)	116 (+196/-62)	---	---

a. Values in parenthesis demonstrate positive and negative uncertainties as defined in the text

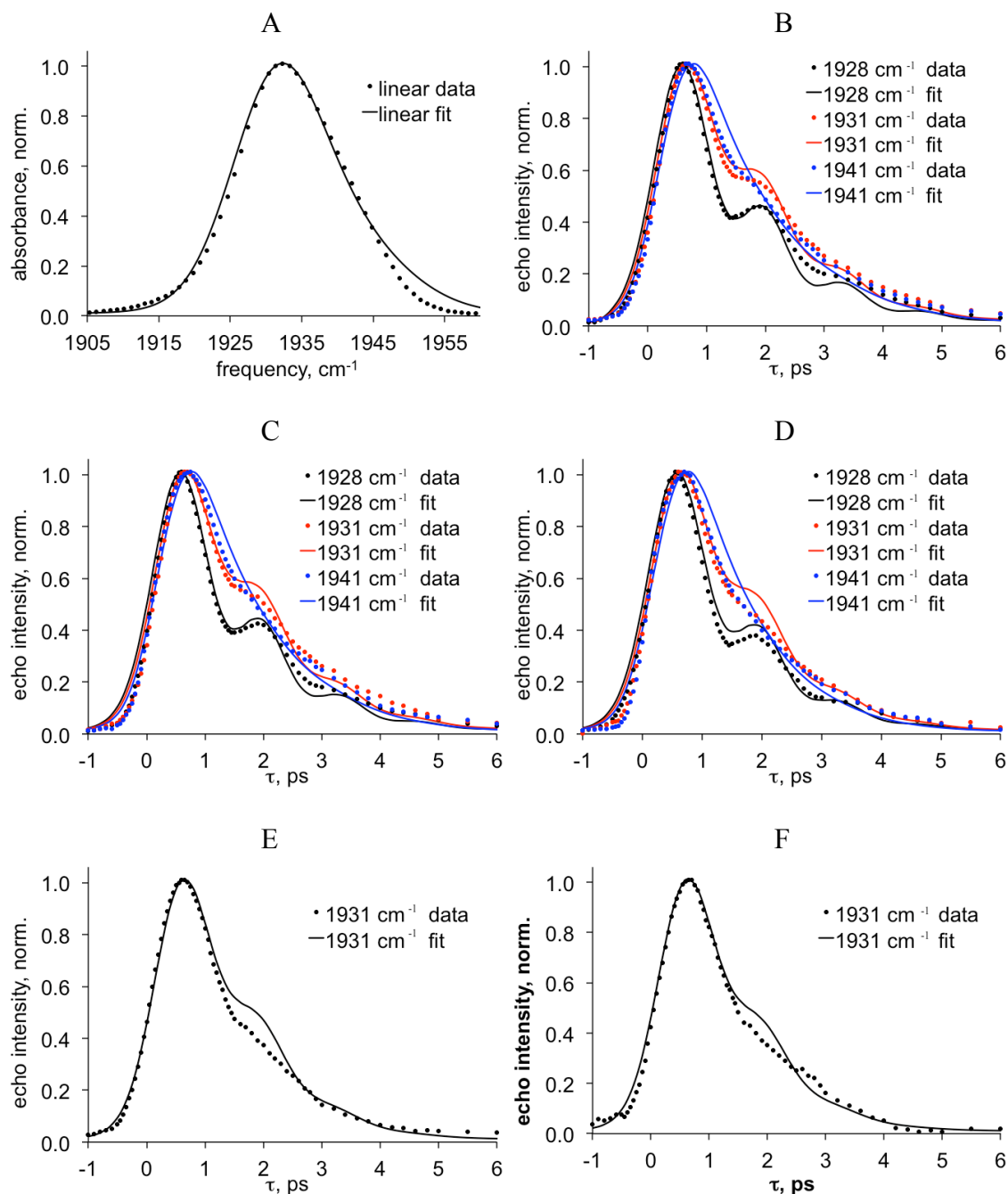


Figure 3.6: Full 1D- and 2D-IR VES data sets for unannealed RuOEP:P3HT. Subplots correspond to (A) linear spectrum, (B)  $T_w = 0.5$  ps, (C)  $T_w = 2$  ps, (D)  $T_w = 5$  ps, (E)  $T_w = 10$  ps and (F)  $T_w = 15$  ps.

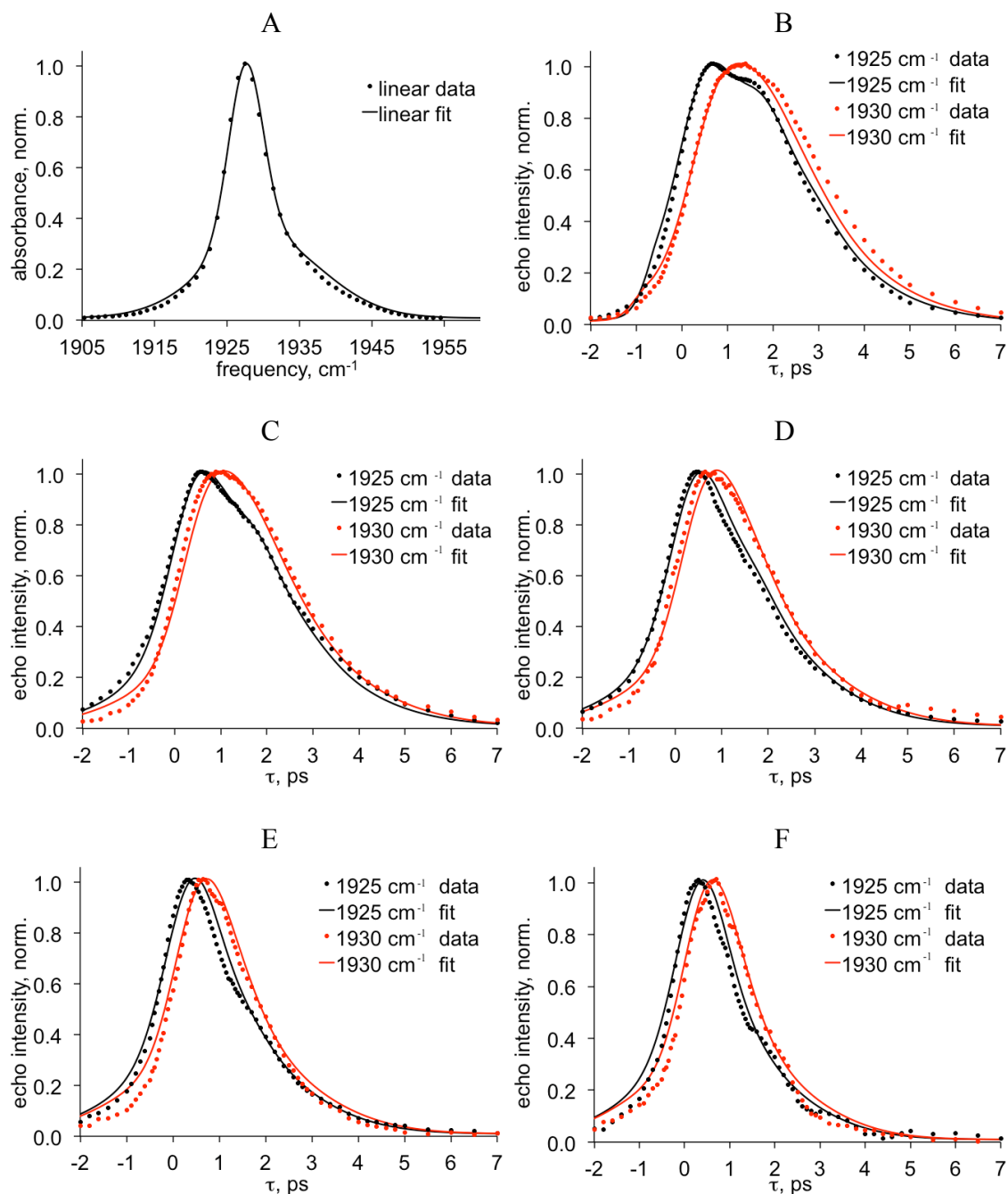


Figure 3.7: Full 1D- and 2D-IR VES data sets for half annealed RuOEP:P3HT. Subplots correspond to (A) linear spectrum, (B)  $T_w = 0.5$  ps, (C)  $T_w = 2$  ps, (D)  $T_w = 5$  ps, (E)  $T_w = 10$  ps and (F)  $T_w = 15$  ps.

### 3.4.6. Evaluation of FFCF Fits

Two features of the unannealed sample FFCFs are notably absent in the half-annealed FFCFs: the static inhomogeneity ( $\Delta_0$ ) and the 400 fs dynamic components. In fact, the entire data set for the half-annealed sample can be fit by two FFCFs containing only exponential terms with dynamics on the tens of ps time scale. The lack of a significant  $\Delta_0$  is consistent with the narrow width of the steady-state absorption spectrum, however, the absent dynamic component could not have been predicted without the use of a 2D-IR methodology. As discussed above, it was anticipated that there would be a motionally-narrowed exponential component in the FFCFs, however, the degree of motional narrowing can determine whether or not this component would be required to fit the data. In the motionally-narrowed regime, the time scale of frequency fluctuations,  $\tau_i$ , is fast compared to the inverse amplitude,  $1/\Delta_i$ , such that the product  $\Delta_i \cdot \tau_i \ll 1$  ( $\Delta_i$  in radians/ps). Under these conditions, neither  $\Delta_i$  nor  $\tau_i$  can be known independently, leaving only their product to describe a single dephasing time. The relevance to the current discussion is that the time scale of frequency fluctuations could become faster upon annealing ( $\tau_i$  gets very small) and this would be indistinguishable from the effect of a vanishing amplitude in the exponential term ( $\Delta_i$  becomes very small).

To demonstrate the role of this exponential term in the fits to the half-annealed data, the linear and nonlinear observables with and without the motionally-narrowed component (defined by  $\Delta_{\text{new}}$  and  $\tau_{\text{new}}$ ) were calculated and compared to their goodness of fits in Figure 3.8. For all calculations in the figure, the parameters listed in Table 3.1 for the half-annealed sample were held fixed and the new motionally-narrowed

exponential term was included. For this additional component, only the motionally-narrowed regime where  $\Delta_{\text{new}} \cdot \tau_{\text{new}} \ll 1$  is plotted. The solid lines in this figure show the percent change in the total residuals squared for fitting all vibrational echo decays at all  $T_w$ s and all frequencies, plus the linear spectrum, as a function of the product of  $\Delta_{\text{new}}$  and  $\tau_{\text{new}}$ . The black, red, blue, and green lines were obtained by maintaining  $\tau_{\text{new}}$  at 50, 100, 200, and 300 fs, respectively, and varying  $\Delta_{\text{new}}$ , while the purple and orange traces were obtained by holding  $\Delta_{\text{new}}$  at 1 and 2  $\text{cm}^{-1}$  and varying  $\tau_{\text{new}}$ . For each curve there is a corresponding dashed line of the same color that shows the pure dephasing time,  $T_2^*$ , obtained as  $(\Delta_{\text{new}}^2 \tau_{\text{new}})^{-1}$ .<sup>49,190,191</sup>

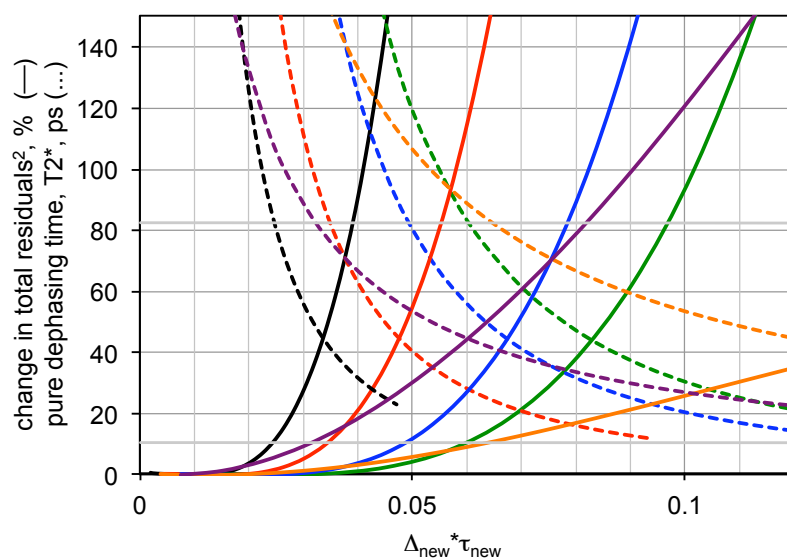


Figure 3.8: Calculated change to the goodness of fit (monitored as the percent change in the total residuals squared) for the half annealed RuOEP:P3HT sample. The FFCF parameters shown in Table 4.1 were held constant for all calculations, and a motionally narrowed exponential term was added to each of the two FFCFs. The  $\Delta_{\text{new}}$  and  $\tau_{\text{new}}$  in this additional component were varied together over a range of values. The black, red, blue, and green solid lines demonstrate the percent changes to the residuals squared, for  $\tau_{\text{new}} = 50, 100, 200,$  and  $300$  fs while varying  $\Delta_{\text{new}}$ . The violet and orange solid lines represent  $\Delta_{\text{new}} = 1$  and  $2 \text{ cm}^{-1}$  while varying  $\tau_{\text{new}}$ . The dashed lines show the pure dephasing time,  $T_2^*$ , dependence on the product of  $\Delta_{\text{new}} \cdot \tau_{\text{new}}$  for each of the corresponding colors.



Accordingly, regardless of the values of  $\Delta_{\text{new}}$  and  $\tau_{\text{new}}$  used in this motionally-narrowed exponential component, for identical  $T_2^*$ s, the effect on the goodness of fit is the same. This can be seen by taking a horizontal slice at any value of  $T_2^*$ , and then looking vertically from each dashed line to its accompanying solid line of the same color to find the magnitude of the perturbation of the fit. Setting a limit on the change in total residuals squared to be 10% (demarcated by a horizontal gray line), it can be shown for the annealed sample that a  $T_2^*$  in excess of 80 ps leads to a minimal (less than 10%) perturbation of the total residuals squared. In fact, when the  $T_2^*$  exceeds 150 ps (the location where each dashed line exits the figure at the top), the inclusion of the additional exponential component in the FCF has a negligible effect on the goodness of fit. When  $T_2^*$  is less than 80 ps, it was found that the presence of the second exponential term in the FFCF can lead to notable changes in the calculated echo decays.

The point of this analysis, with respect to Figure 3.4B, is that  $\Delta_{\text{new}}/\tau_{\text{new}}$  combinations of  $0.8 \text{ cm}^{-1}/300 \text{ fs}$  and  $2 \text{ cm}^{-1}/50 \text{ fs}$  have  $T_2^*$ s of approximately 150 ps and would both lead to imperceptible improvements to the fit qualities over the single exponential plus a constant FFCFs used in Table 3.1. The observations of large peak shifts in Figure 3.4B and narrow linear lineshapes are explained by the transition of the 400 fs exponential term in the FFCFs for the unannealed sample to a motionally-narrowed exponential component in the FFCFs for the half-annealed sample. Whether the motional-narrowing is achieved by a loss of frequency perturbation amplitude ( $\Delta$ ) or a decrease in modulation time scale ( $\tau$ ) cannot be determined from these experiments, and we have minimized unnecessary adjustable parameters in our fitting procedure by excluding them whenever possible. Thus, it is conceivable that there is a combination

of both effects since the spectrum of low frequency vibrations that leads to vibrational dephasing in the 2D-IR VES experiment should peak at higher frequencies as the P3HT molecules become more densely packed and ordered during annealing.<sup>192-195</sup>

#### **3.4.7. Rationalization for Observed Vibrational Dynamics and Mobility**

Referring back to the electrical data taken on these films, as the annealing proceeds and the mobility increases from the unannealed to the half-annealed state, the FFCFs obtained by fitting the 2D-IR VES data indicate a concurrent loss of vibrational dephasing with a time constant of 400 fs. Low frequency ring torsional vibrations have been calculated for poly(phenyl) and poly(thiophene) systems to be in the range of 60 to 130  $\text{cm}^{-1}$ .<sup>196-198</sup> Although the 400 fs dephasing dynamics cannot be definitely assigned to a molecular origin using 2D-IR VES alone, their time scale is consistent with these ring torsional vibrations (approximately 80  $\text{cm}^{-1}$ ). A damping of torsion motions would be expected with a decrease in the interchain spacing and an increase in pi-orbital stacking, leading to higher carrier mobilities. Vukmirovic and coworkers have recently used molecular dynamics simulations to demonstrate that charge carriers can in fact be localized through the disordered regions of P3HT by torsional motions, leading to a decrease of charge mobilities.<sup>29,30</sup> The experimental evidence in this chapter supports the notion that mobility enhancements can originate in both static and dynamic structural changes. Using a simplified model that incorporated only torsional degrees of freedom, de Brito and coworkers have shown through simulations that charge carrier trapping occurs along P3HT chains when the antinode spacings of torsional vibrations are comparable to the size of the polaron or bipolaron, whereas vibrational wavelengths significantly larger or smaller than the polaron width have no appreciable effect on its

mobility.<sup>199</sup> Therefore a shift of the low frequency vibrations to higher energies during annealing, characterized as a transition of the 400 fs FFCF component to the motionally-narrowed regime, could have the effect of boosting mobilities by eliminating hole trapping along the polymer chains.

### 3.5. Conclusions

Although P3HT is a semicrystalline polymer, its carrier mobilities are dominated by transport through disordered regions. The structural dynamics that occur in these amorphous regions are complex and have been studied to some degree by simulations. In this work, a known method for improving hole mobilities in P3HT was taken and the impact of this process on the ground state molecular dynamics using 2D-IR VES was measured. A vibrational dynamics probe, RuOEP, was incorporated and verified to cause a minimal perturbation on the electrical characteristics of the unannealed and half-annealed P3HT films. The 2D-IR studies enabled extraction of FFCFs for each annealed state that could be used to quantify dynamical changes in the films. Concurrent with a 30% increase in hole mobility, a loss of structural dynamics on the time scale of 400 fs is noted, which is suggestive of a damping of ring torsion vibrational modes in the 100-200  $\text{cm}^{-1}$  regime. This work provides experimental support for simulations that have predicted that dynamic disorder, especially in the frequency range of torsional vibrations, can lead to decreased carrier mobilities in polyaromatic thin films. Based on these results, it can be concluded that the mobilities of organic semiconducting films could be improved by synthetic modifications that not only optimize static molecular packing but also tune specific dynamical degrees of

freedom.<sup>b</sup>

---

<sup>b</sup> The authors gratefully acknowledge funding from the Donors of the American Chemical Society Petroleum Research Fund for partial support of this research (46628-G6). We also acknowledge the 3M Corporation Nontenured Faculty Award, a Grant-in-Aid from the University of Minnesota, Twin Cities, and partial support by the National Science Foundation under CHE-0847356. TEM measurements were performed at the University of Minnesota Characterization Facility, which receives support from the NSF through the NNIN. The authors additional thank Dr. Tim Anglin for the mobility measurements.

## Chapter 4

# Ground-State Structural Dynamics in Doped and Undoped Polyaniline Films Probed by 2D-IR Vibrational Echo Spectroscopy

Reproduced in part with permission from:

Audrey A. Eigner, Brynna H. Jones, Bryce W. Koprucki, and Aaron M. Massari.

Ground-State Structural Dynamics in Doped and Undoped Polyaniline Films Probed by 2D-IR Vibrational Echo Spectroscopy. *Journal of Physical Chemistry B*. **2011**, 115, pp. 4583-4591.

Copyright, 2011 American Chemical Society.

## 4.1. Chapter Summary

In this chapter, 2D-IR VES is used to study polyaniline (PANI) thin films in three states of varying conductivity: emeraldine base (PANI-EB, semiconducting) and emeraldine salt (PANI-ES) doped with dinonylnaphthalene sulfonic acid (DNNSA, conductive) and camphor sulfonic acid (CSA, highly conductive). UV-visible and FTIR spectroscopies were used to characterize the static electronic and structural differences between these materials, and then these results were compared to the dynamical results from 2D-IR VES. The electronic ground state ultrafast dynamics for the PANI-EB reveal very fast motions that are not present in either of the PANI-ES samples. Despite differences in conductivity, no significant dynamical differences are observed for the films prepared with the two dopants. These results are interpreted in light of previous work on the structural ordering induced by doping with sulfonic acids and the possible correlations between charge carrier mobilities and low frequency structural dynamics.

## 4.2. Introduction

Polyaniline has been heavily studied as an organic conductor due to its excellent environmental stability, ease of processing, and relatively inexpensive starting materials.<sup>200-202</sup> PANI is unique among conducting polymers in that its conductivity can be tuned by both redox chemistry and the degree of protonation.<sup>203,204</sup> Figure 4.1 shows the partially oxidized semiconducting emeraldine base (EB) form of PANI and its protonated conducting emeraldine salt (ES) form, which has achieved metallic conductivities under certain conditions.<sup>5,203,205</sup> A wealth of acids have been demonstrated to be efficient dopants for converting PANI-EB to PANI-ES, but sulfonic acids are the most common. Several groups have studied the effects of different sulfonic acid dopants, and have found that the molecular ordering and conductivities correlated with the dopant used.<sup>202,206-210</sup> From the perspective of studying the impact of ultrafast structural dynamics on carrier mobilities, PANI-ES provides a convenient system in which the conductivity can be tuned by replacing the dopant species while leaving the chemistry of the polymer backbone unchanged. Although there are many reports on the ultrafast dynamics of conducting polymers, the majority of these have focused on the relaxation of electronically excited states, often addressing the role of structural dynamics in facilitating such processes.<sup>196,211-214</sup> Kim and coworkers have recently provided some insight into the time scales of dynamic processes that occur in PANI films, however they specifically probed the structural motions associated with relaxation of the electronic excited state. Their work suggested that distortions of the polymer backbone and ring-torsional motions play a role in the relaxation of the photoexcited polaron.<sup>215,216</sup>

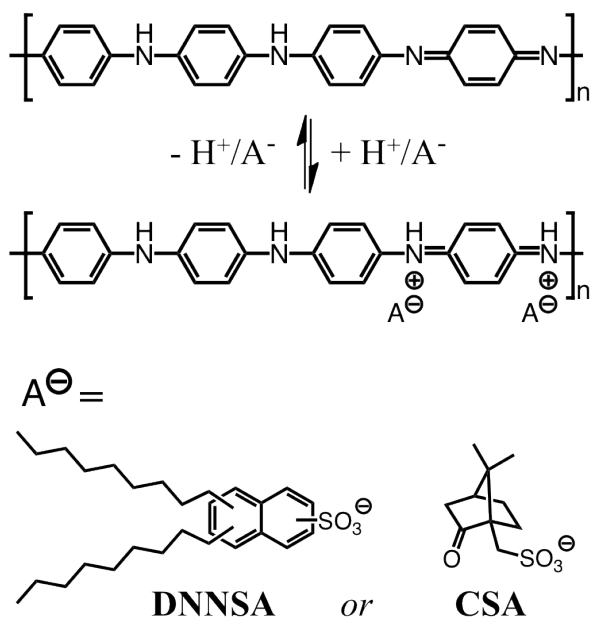


Figure 4.1: Molecular Structures for PANI-EB (top), PANI-ES (middle), and dopants (bottom).

In the present chapter, spectrally resolved homodyne-detected 2D-IR vibrational echo spectroscopy (2D-IR VES) was applied to thin films of PANI. By monitoring the frequency fluctuations of the metal-bound CO vibration on an extrinsic vibrational probe molecule, ruthenium octaethylporphyrin (RuOEP), the molecular dynamics in semiconducting PANI-EB and conducting PANI-ES films doped with two structurally different sulfonic acids (shown in Scheme 1) were measured. Camphor sulfonic acid (CSA) was chosen as a dopant that is known to produce well-ordered PANI-ES films with high conductivities,<sup>5,203,205</sup> while dinonylnaphthalene sulfonic acid (DNNSA) was selected as a dopant that generates films with moderate conductivities.<sup>207,217</sup> After characterizing these films with steady-state UV-visible and FTIR spectroscopies, 2D-IR VES was used to uncover differences in the time-dependent structural motions. The static and dynamic differences for these films were then interpreted in the context of what has been reported about their molecular architectures and charge mobilities.



## 4.3. Experimental

### 4.3.1. Materials

Polyaniline (emeraldine base) (MW=10kD) (PANI-EB), camphor-10-sulfonic acid  $\beta$  (98%) (CSA), dinonylnaphthalene sulfonic acid (50 wt% solution in heptane) (DNNSA), and 2,3,7,8,12,13,17,18-octaethyl-21*H*,23*H*-porphine ruthenium(II)carbonyl (RuOEP) were used as received from Sigma-Aldrich. All solvents were reagent grade and were used as received without further purification.

### 4.3.2. Preparation of undoped PANI-EB films

A solution of PANI-EB in *N*-methylpyrrolidone (NMP) was prepared by dissolving 10 mg of PANI-EB in 2 mL of NMP. The solution was stirred for 12 hrs before being filtered through a 0.45  $\mu\text{m}$  syringe filter to remove particulates. A 50  $\mu\text{L}$  aliquot of a separately made 0.45  $\mu\text{m}$  filtered 27 mM RuOEP in NMP solution was added to the PANI-EB mixture to obtain a 10:1 PANI:RuOEP mass ratio in the final mixture. A saturated solution of PANI-EB in formic acid was prepared and 0.45  $\mu\text{m}$  filtered to remove particulates, and then 50  $\mu\text{L}$  were spin-coated onto a 1 inch  $\text{CaF}_2$  window for 2 min at 1000 rpm. This thin formic acid doped PANI-ES coating served as an adhesion layer, enabling the subsequent PANI-EB film to wet the  $\text{CaF}_2$  surface. The adhesion layer was allowed to dry in air for 10 min before 350  $\mu\text{L}$  of the PANI/RuOEP in NMP were drop cast onto the window. The film was then dried for approximately 3 hrs in a vacuum oven at 45  $^\circ\text{C}$ .

### 4.3.3. Preparation of DNNSA doped PANI-ES films

A 1:3 mole ratio of PANI-EB (four ring repeat unit, see Scheme 1) to DNNSA was prepared by dissolving 30 mg of PANI and 270  $\mu\text{L}$  of DNNSA (in heptane) in 6

mL of chloroform in a small glass vial. The solution was stirred for approximately 12 hrs before being filtered through a 0.45  $\mu\text{m}$  syringe filter and drop cast in equal portions onto five clean glass microscope slides. The drop cast films were allowed to dry in air and were then washed from the slides with acetone onto 7.5 cm Whatman filter paper. This produced a doped PANI-ES powder free from excess heptane and DNNSA, which was dried and then redissolved in chloroform. Typically, 33 mg of washed PANI/DNNSA product were dissolved in 2000  $\mu\text{L}$  of chloroform and stirred for 12 hrs. The solution was then filtered through a 0.45  $\mu\text{m}$  syringe filter and a 50  $\mu\text{L}$  portion of a separately made 0.45  $\mu\text{m}$  filtered 27 mM RuOEP in chloroform solution was added to obtain a 10:1 PANI:RuOEP mass ratio (based on a 1:2 mol ratio of PANI to DNNSA) in the final mixture. A 350  $\mu\text{L}$  aliquot of the final solution was then spin-coated at 50 rpm for 4 min onto a 1 inch  $\text{CaF}_2$  window.

#### **4.3.4. Preparation of CSA doped PANI-ES films**

A 1:3 mole ratio of PANI-EB (four ring repeat unit, see Scheme 1) to CSA was prepared by dissolving 10 mg of PANI and 19 mg of CSA in 2 mL of chloroform in a small glass vial. The solution was stirred for approximately 12 hrs and then filtered through a 0.45  $\mu\text{m}$  syringe filter to remove particulates. A 50  $\mu\text{L}$  portion of a separately made 0.45  $\mu\text{m}$  filtered 27 mM RuOEP in chloroform solution was then added to obtain a 10:1 PANI:RuOEP mass ratio in the final mixture. A 350  $\mu\text{L}$  aliquot of the final solution was then spin-coated at 50 rpm for 4 min onto a 1 inch  $\text{CaF}_2$  window.

#### **4.3.5. 2D-IR Vibrational Echo Spectroscopy**

The 2D-IR VES technique employed in this work has been described previously (refer to Section 3.3.4.).

## 4.4. Results and Discussion

### 4.4.1. UV-vis PANI-EB and PANI-ES with and without RuOEP

The UV-visible spectra collected for PANI-EB (black solid line) and PANI-ES (red solid line is DNNSA-doped, blue solid line is CSA-doped) films are shown in Figure 4.2. An absorption spectrum for a film of only RuOEP spin-coated from chloroform is also overlaid (green dashed line) for reference, as each of the three films contains a small weight percent of RuOEP to PANI. Each of the three polymer absorption spectra shows strong evidence of the porphyrin Soret band near 400 nm and Q-bands at 515 and 545 nm despite the low concentration of the RuOEP in the blended films. This is readily explained by the fact that the absorption coefficients for porphyrin absorption bands are typically an order of magnitude greater than any of the absorbances in PANI.<sup>218,219</sup> For comparison, the UV-visible spectra for PANI-EB and PANI-ES doped with DNNSA and CSA without the RuOEP vibrational reporter were also collected and are included (vertically offset) as the dashed black, red, and blue lines, respectively. It is clear that the presence of the RuOEP in these films has minimal impact on the UV-visible spectra, which implies that the electronic structures of the polymers are not measurably perturbed by the guest species. In the spectrum of PANI-EB, there are two broad absorption features from the polymer centered at 300 and 605 nm. Huang and MacDiarmid have attributed the 300 nm peak to a  $\pi$ - $\pi^*$  transition and a transition from low-lying orbitals to the  $\pi_q$  orbital, and the 605 nm peak to the electronic excitation from benzenoid ( $\pi_b$ ) to quinoid rings ( $\pi_q$ ).<sup>220</sup>

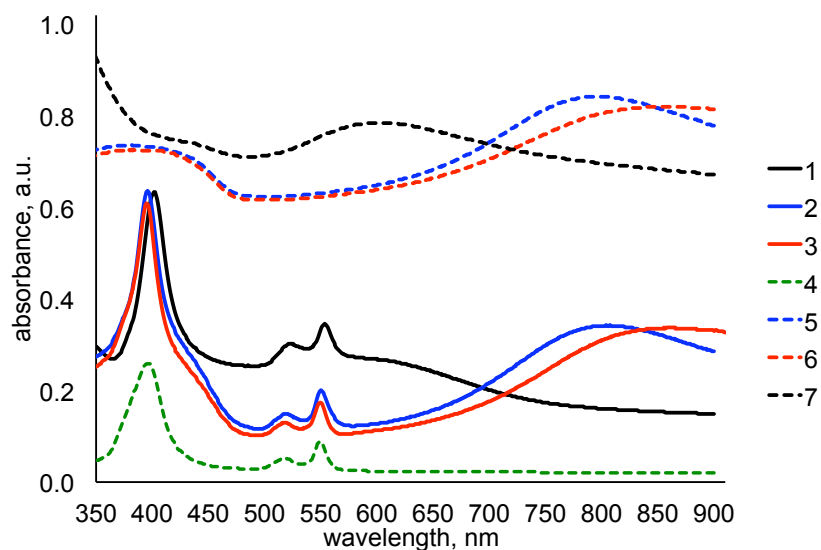


Figure 4.2: UV-visible spectra of RuOEP in (1) PANI-EB, (2) PANI-ES doped with CSA, and (3) PANI-ES doped with DNNSA. The spectrum for a RuOEP film spin-coated from chloroform is shown as a reference (3). Vertically offset by 0.55 (dashed lines) are the spectra for the three PANI samples without RuOEP for comparison, same color scheme.

The UV-visible spectra of the PANI-ES films are notably different from the PANI-EB spectrum, but are similar to each other, indicating that comparable electronic structures exist between the two doped films. Each of the films shows a transition near 400 nm and a lower energy band approaching the near IR region. The lower energy band in the doped films has been attributed to a transition from the  $\pi$  to polaron band, and occurs at 860 and 810 nm for the DNNSA and CSA doped samples, respectively. The location of this band in the near-IR is suggestive of a primary doping mechanism in PANI-ES, reflecting a “tight coil” molecular configuration in which there are frequent ring-ring torsions along the polymer backbone that cause adjacent benzenoid and quinoid rings to align in a non-planar fashion.<sup>221-223</sup> It has been demonstrated that exposure of PANI to strongly interacting solvents can relax this molecular configuration to an “expanded coil” (secondary doping) thereby shifting this localized polaron band

into the mid-IR region, increasing ring planarity, and improving the electrical conductivity of the polymer.<sup>221-223</sup> For PANI-ES films displaying the characteristic localized polaron band, including the DNNSA and CSA doped samples in the current study, the center wavelength of this feature is a spectral marker that reflects the extent to which the polymer exists in the tight or expanded coil conformations. Differences in the center wavelength of this absorption band have been previously reported and are dependent on the dopant used and the preparation method.<sup>207</sup> In this study, the lower energy band of the DNNSA doped film is somewhat broader than the band of the CSA doped sample, which may indicate a slightly more relaxed structure exists in the DNNSA film. Nevertheless, in both cases the UV-visible spectra in Figure 4.2 confirm that the PANI-ES films examined in this study were primarily doped using the preparations described above and casting from a volatile, non-hydrogen bonding solvent. The PANI-EB films, on the other hand, were cast from NMP, a non-volatile solvent that is frequently reported to remain in PANI films in small concentrations after casting. Zheng and coworkers have shown that PANI-EB films made in the absence of strongly interacting organic liquids or vapors have a  $\pi_b - \pi_q$  absorption band near 600 nm that shifts to 645 nm upon exposure to NMP vapors.<sup>223</sup> As such, the appearance of this absorption band at 605 nm in Figure 4.2 suggests that there is minimal residual solvent in the PANI-EB films studied here.

#### **4.4.2. FTIR of PANI-EB and PANI-EB doped with CSA and DNNSA**

Differences in the FTIR spectra of the PANI-EB and two PANI-ES thin films were also observed. Figure 4.3 shows the FTIR spectra of the three samples in the ruthenium-bound CO stretching region. All three of these baselined spectra require two

Gaussians to properly fit their shapes, a larger amplitude peak that we refer to as the major band and a smaller amplitude peak, the minor band, which compensates for the overall band asymmetry. In the PANI-EB film, the major band is centered at  $1923\text{ cm}^{-1}$  with a FWHM of  $24\text{ cm}^{-1}$ , while the major bands for the DNNSA and CSA doped PANI-ES films are located at  $1939$  and  $1926\text{ cm}^{-1}$  with FWHMs of  $21$  and  $17\text{ cm}^{-1}$ , respectively. The Gaussian shapes of these bands suggest that they are inhomogeneously broadened, as is typical of condensed phase FTIR spectra. In both of the doped PANI-ES films the major band is shifted to higher frequencies relative to that of the PANI-EB sample. These FTIR lineshape shifts are an indication of variations in the available range of frequencies for the metal-bound CO vibrational mode, and are caused by differences in the molecular configurations of the three PANI films. The linewidth of the PANI-EB major band is the broadest of the three samples studied, and that of the CSA doped PANI-ES is the narrowest. If the FTIR linewidths were dominated by inhomogeneous broadening, this could be interpreted as an indication that a more homogeneous chemical environment exists around the RuOEP molecules in the CSA film. This is a reasonable notion since the introduction of dopants into PANI films has been reported to induce a certain amount of molecular ordering, forming layered structures in which the polymer chains are aligned between the dopant molecules (see Figure 4.8 below).<sup>202,206-209,224,225</sup> For certain, the fact that the FTIR absorption spectrum of the metal-bound CO shifts and has different linewidths indicates that there are structural differences that exist between these three samples. This is further supported by the free carrier absorption that appears as a broad rising baseline in the full FTIR spectra of the PANI-ES thin films in Figure 4.3B. The PANI-ES samples have large

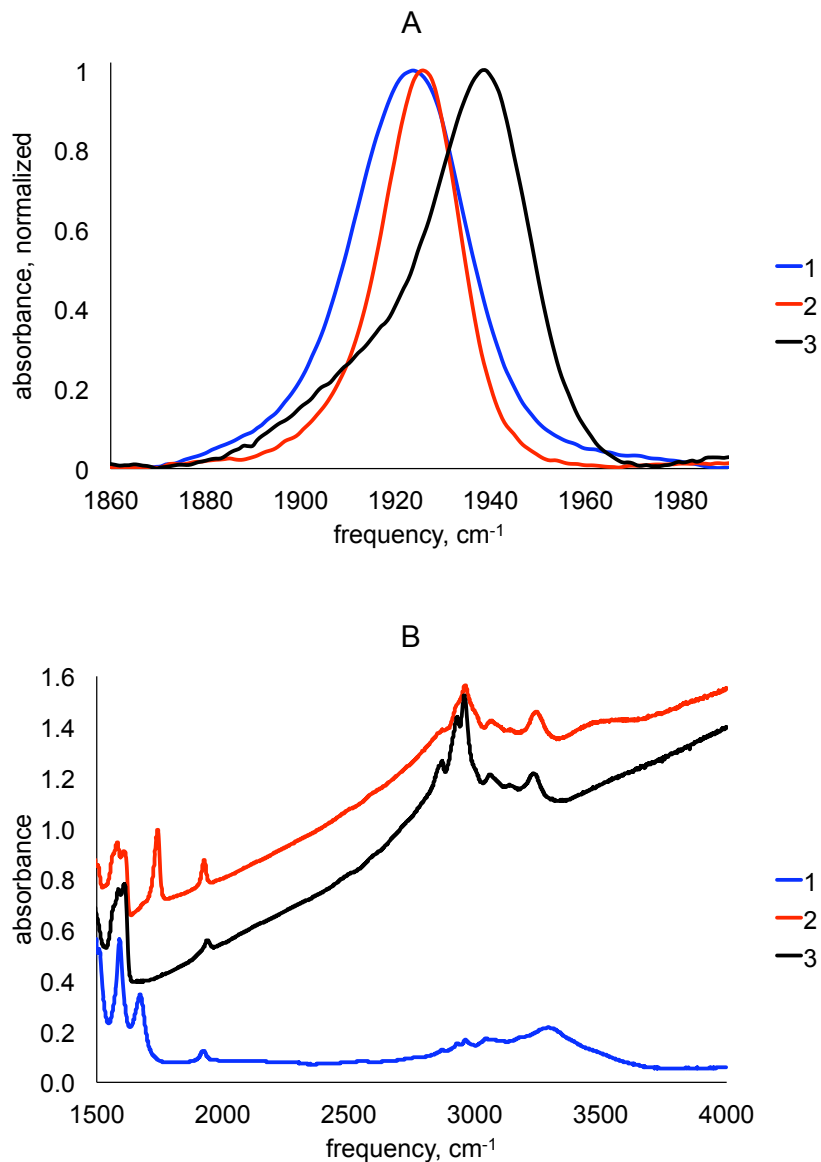


Figure 4.3: (A) Baselined and normalized FTIR spectra of the ruthenium-bound CO symmetric stretching vibration in PANI-EB [1], PANI-ES doped with CSA [2], and PANI-ES doped with DNNSA [3]. (B) The full range of FTIR spectra for these three materials (same color scheme).

offsets across the mid-IR due to the polaron absorption that results from protonation of the polymer by DNNSA and CSA. As expected, the undoped PANI-EB spectrum shows no evidence of this polaron band.

#### 4.4.3. 2D-IR VES of PANI-EB and PANI-ES doped with CSA and DNNSA

Selected vibrational echo decays for the three PANI samples are compared in Figure 4.4. Each frame shows two decays collected with  $T_w = 0.5$  ps and  $T_w = 10$  ps. For clarity, the data show the vibrational echo decays at only a single frequency, however, the complete data sets included decays measured at three frequencies across the FTIR lineshape. The full data sets, which also include decays collected at three additional  $T_w$ s, are provided in Figures 4.5, 4.6, and 4.7. In Figure 4.4, the  $T_w = 10$  ps traces decay faster than the  $T_w = 0.5$  ps traces in each frame. This indicates that the structural configurations in the PANI-EB and ES films are interconverting during the  $T_w$  period leading to spectral diffusion. These dynamics are occurring on the time scale of a few to tens of ps, and the ability to sample them is limited by the vibrational lifetime of the metal-bound CO.

As mentioned in Chapter 3, the oscillations in the intensities of the echo decays are attributed to strongly coupled anharmonic energy levels, and are referred to as accidental degeneracy beats (ADBs).<sup>189</sup> Because the bandwidth of the pulses used in this technique is broad enough to span the anharmonicity of the metal-bound CO mode, there is a high probability that higher order transitions are accessed (i.e.  $v = 1-2$ ). In systems in which the linewidths are comparable to the vibrational anharmonicity, vibrational echo signals emitted from higher transitions may have frequencies that overlap with those of lower transitions causing a modulation in the echo intensity at the



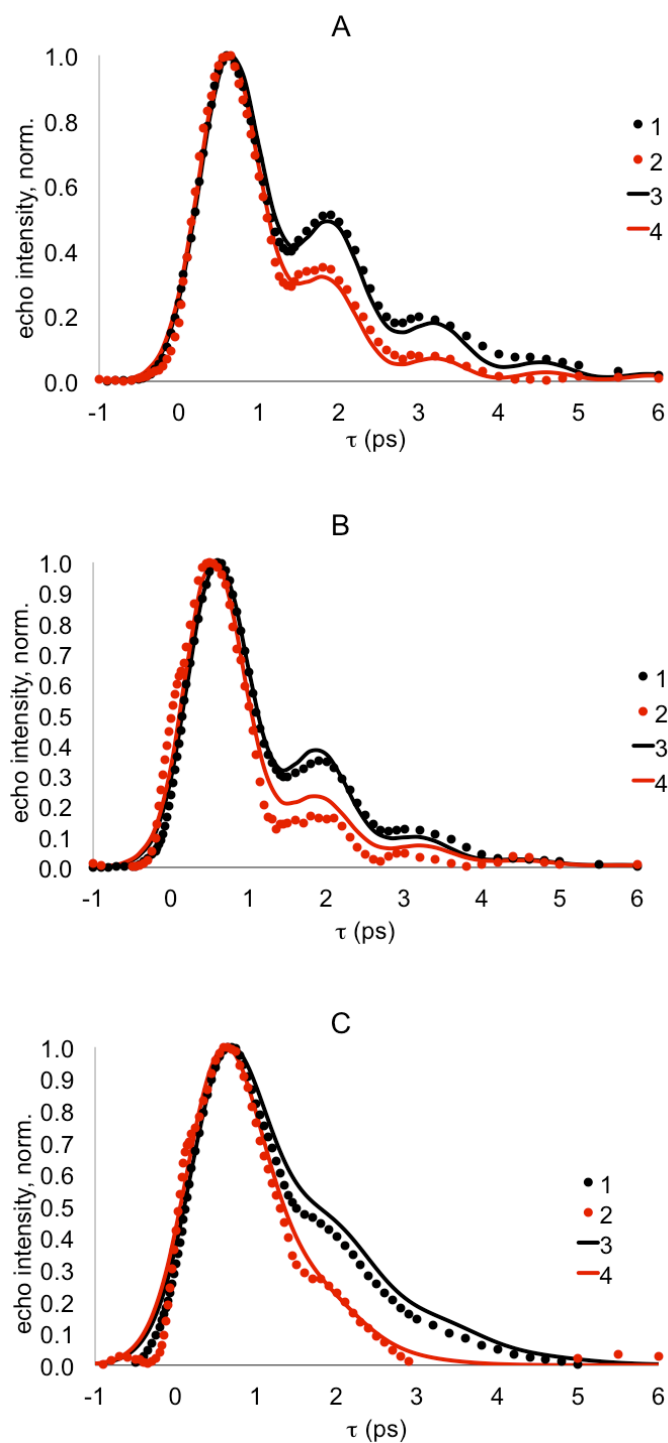


Figure 4.4: Vibrational echo decays collected at  $T_w = 0.5$  ps [1] and  $T_w = 10$  ps [2] for (A) PANI-EB measured at  $1925\text{ cm}^{-1}$ , (B) PANI-ES doped with DNNSA measured at  $1935\text{ cm}^{-1}$  and (C) PANI-ES doped with CSA measured at  $1925\text{ cm}^{-1}$ . In all plots, the dots are the experimental data [1][2] and the solid lines [3][4] are the corresponding calculated echo decays from the best fit parameters in Table 4.1.

difference in their frequencies (anharmonicity). The widths of the FTIR lineshapes in Figure 4.3A can explain the differences in oscillation depth on the decays of the three samples. The CSA doped PANI-ES films exhibit vibrational echo decays (Figure 4.4C) with shallower beats than both the PANI-EB and the DNNSA doped PANI-ES samples. Since the anharmonicity of the carbonyl vibration is the same in all three samples (as indicated by the nearly identical beating frequencies), a smaller overlap of the 0-1 and 1-2 states results in weaker beating for the CSA sample.

Another notable difference between the vibrational echo decays in Figure 4.4 is that the positions of the vibrational echo maxima on the  $\tau$ -axes vary between the three samples. For all samples, the appearance of this vibrational echo peak shift points to the existence of structural dynamics that are outside of the range that the technique is able to resolve. In practice, structural dynamics that occur on time scales greater than three vibrational lifetimes cannot be well resolved by the 2D-IR VES technique, and will appear as inhomogeneous broadening in the vibrational echo peak shift. Likewise, some of the fastest motions of the system are also not able to be resolved. These dynamics occur in the motionally narrowed regime where the product of the frequency modulation time,  $\tau_m$ , and the modulation amplitude,  $\Delta_m$ , is significantly less than unity.<sup>190,191</sup> In this study, neither the slowest nor fastest time scale regimes are of interest as they do not occur on the same time scale as charge hopping events for typical PANI films. It is interesting to note however, that the echo decays of the PANI-EB sample appear to shift to  $\tau = 0.5$  ps, while the decays of both of the doped samples shift somewhat farther to  $\tau = 0.8$  ps. This larger vibrational echo peak shift is usually

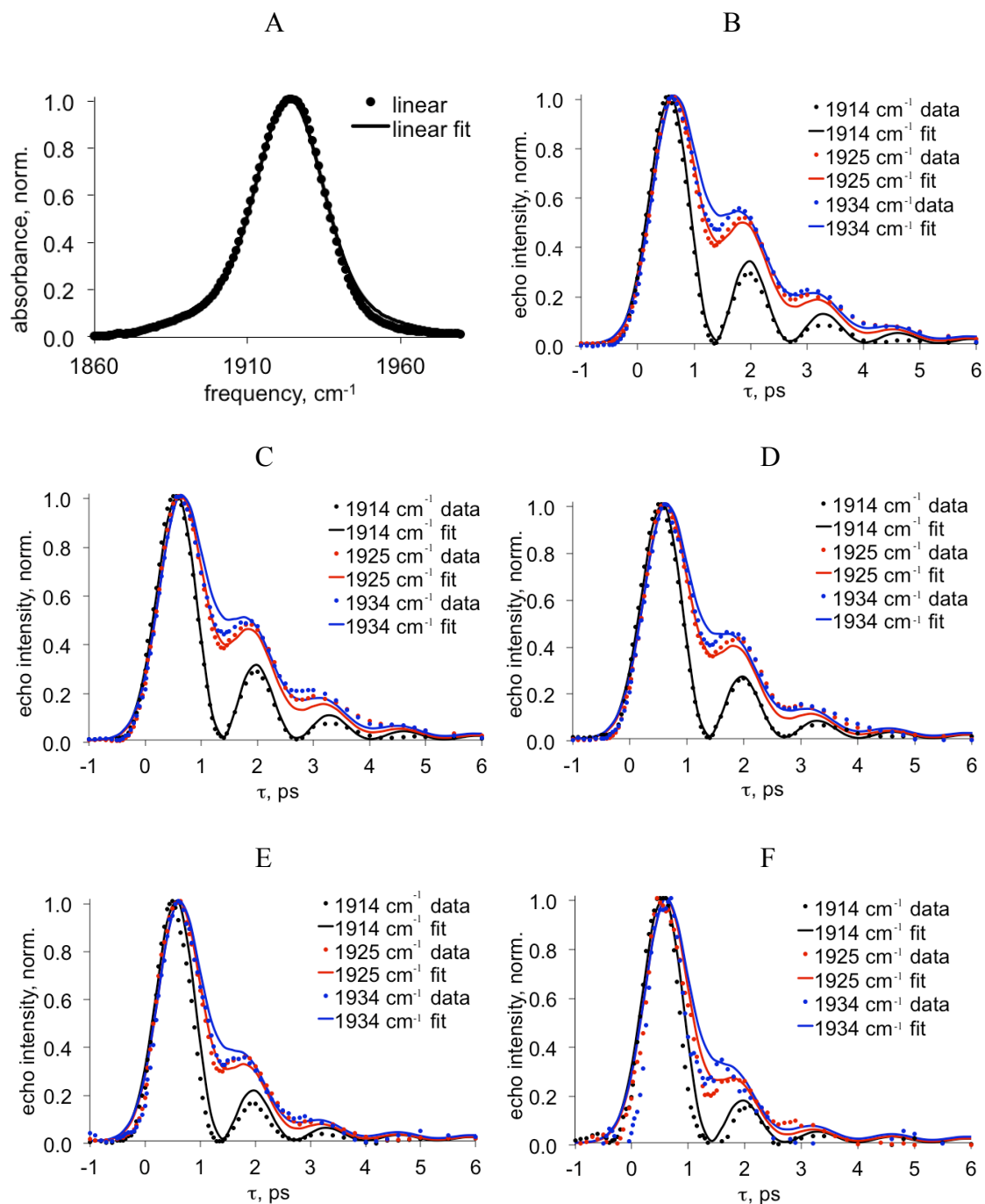


Figure 4.5: Full 1D- and 2D-IR VES data sets for RuOEP in PANI-EB. Data are shown as points and fits are shown as solid lines for the (A) linear, (B)  $T_w = 0.5$ , (C)  $T_w = 2$ , (D)  $T_w = 5$ , (E)  $T_w = 10$ , and (F)  $T_w = 15$ . The parameters used to generate these fit curves are those shown in Table 4.1.

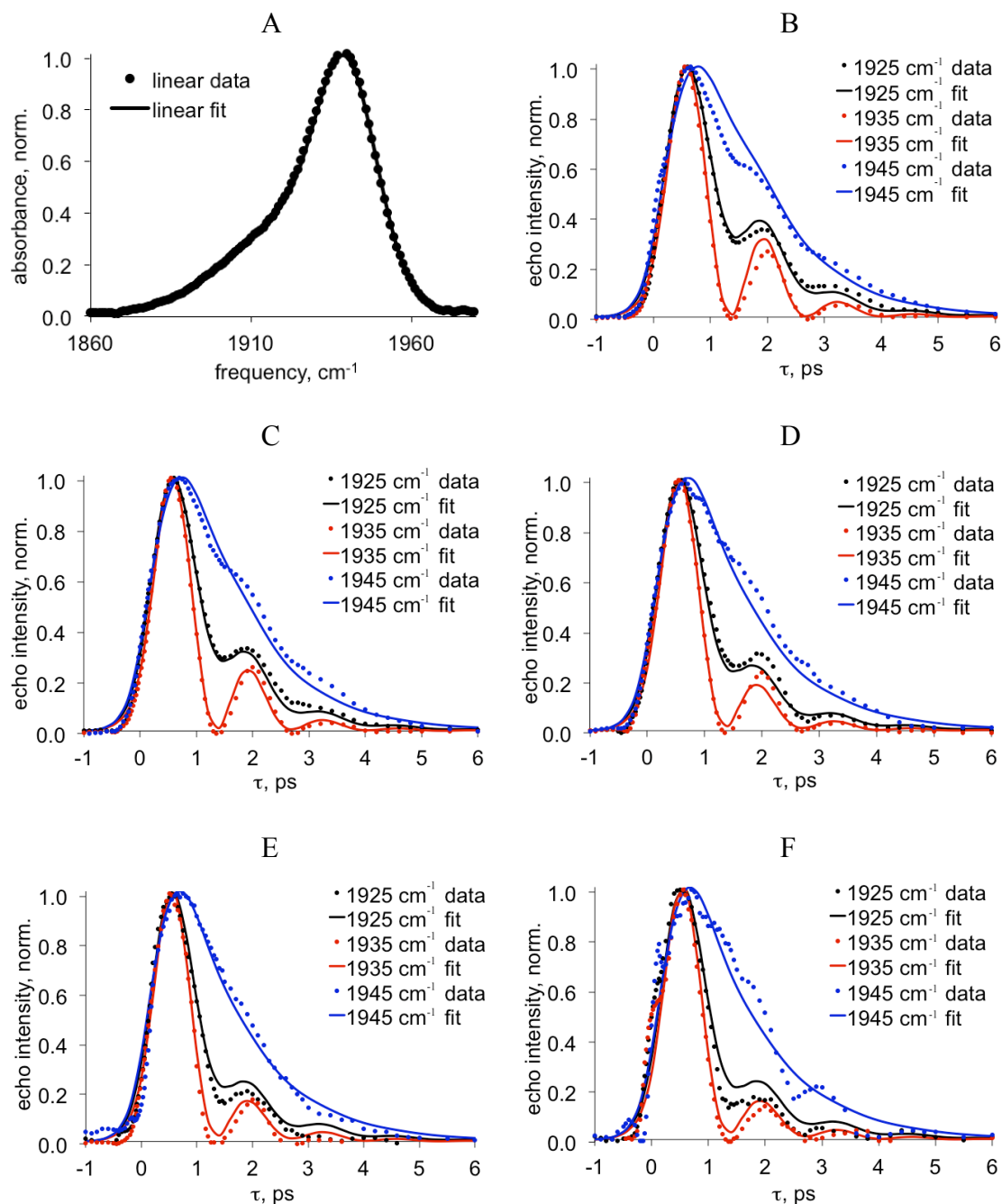


Figure 4.6: Full 1D- and 2D-IR VES data sets for RuOEP in PANI-ES doped with DNNSA. Data are shown as points and fits are shown as solid lines for the (A) linear, (B)  $T_w = 0.5$ , (C)  $T_w = 2$ , (D)  $T_w = 5$ , (E)  $T_w = 10$ , and (F)  $T_w = 15$ . The parameters used to generate these fit curves are those shown in Table 4.1.

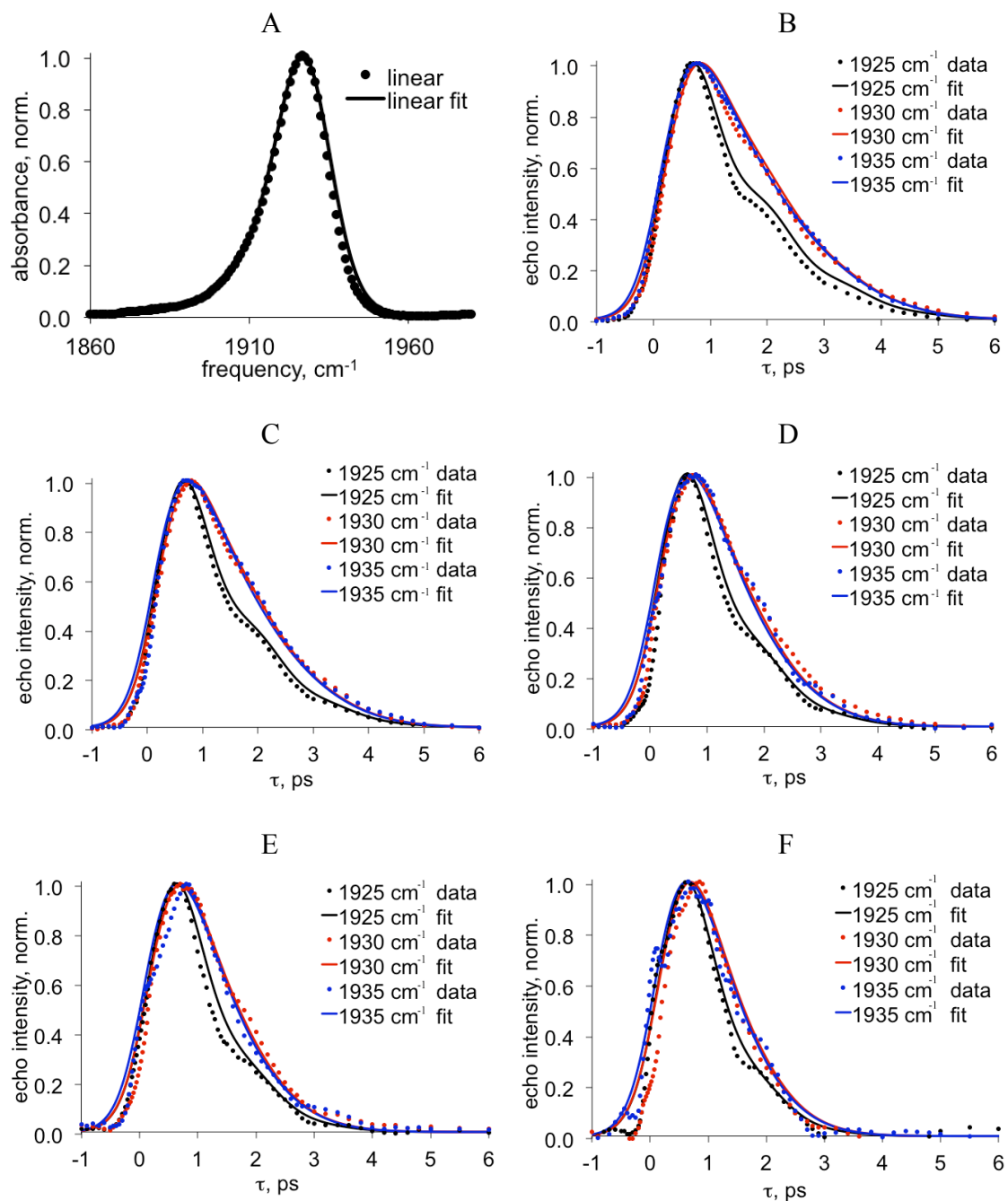


Figure 4.7: Full 1D- and 2D-IR VES data sets for RuOEP in PANI-ES doped with CSA. Data are shown as points and fits are shown as solid lines for the (A) linear, (B)  $T_w = 0.5$ , (C)  $T_w = 2$ , (D)  $T_w = 5$ , (E)  $T_w = 10$ , and (F)  $T_w = 15$ . The parameters used to generate these fit curves are those shown in Table 4.1.

correlated with a more inhomogeneously broadened lineshape. Yet the FTIR spectra in Figure 4.3A do not follow this trend, as the PANI-EB sample has the broadest lineshape, but the smallest positive shift of the echo decay maximum.

#### 4.4.4. Description of FFCF Parameters

The FFCF parameters generated for all PANI samples are compiled in Table 4.1. The error bars (in parentheses) in the table reflect the extremes to which each of the parameters can be varied letting all of the other parameters adjust to recover 99% of the sum of the residuals squared. In this work, and in previous chapters, it was found that the FTIR lineshape of the ruthenium bound carbonyl in blended polymer films requires the use of two Gaussian transitions to reproduce the data.<sup>32,167</sup> Likewise, two transitions are required to properly fit the vibrational echo decays, and there is a larger (major) and a smaller (minor) amplitude transition, each with its own FFCF. For the PANI-EB sample, transitions centered at 1921.7 and 1923.6  $\text{cm}^{-1}$  were found to reproduce the linear and nonlinear data well. For the two FFCFs of PANI-EB, the major transition had a bi-exponential form, while the minor transition contributed only an inhomogeneously broadened term ( $\Delta_0$ ). The presence of the minor transition was needed primarily to fit the linear lineshape and adjust the depth of the accidental degeneracy beats on the decays in Figure 4.4A, having minimal impact on the echo decay times. By fitting the PANI-EB data in this manner, structural dynamics with modulation times of 300 fs and a few hundred ps were found to dominate the frequency fluctuations of the metal-bound CO ( $\tau_1$  and  $\tau_2$  in Table 4.1).

Table 4.1: FFCF parameters used to fit 2D-IR VES data in Figures 4.4, 4.5, 4.6, and 4.7.

FFCF parameters	PANI-EB		PANI-ES DNNSA		PANI-ES CSA	
	<i>transition</i>	<i>transition</i>	<i>transition</i>	<i>transition</i>	<i>transition</i>	<i>transition</i>
	<i>1</i>	<i>2</i>	<i>1</i>	<i>2</i>	<i>1</i>	<i>2</i>
center frequency ( $\text{cm}^{-1}$ )	1923.6	1921.7	1939.7	1918.9	1927.3	1916.8
relative concentration	1	0.47	1	0.70	1	0.55
anharmonicity ( $\text{cm}^{-1}$ )	25.2	25.2	25.4	24.8	24	24
vibrational lifetime (ps)	10.1	10.1	11.5	11.5	7.1	7.1
$\Delta_0$ ( $\text{cm}^{-1}$ )	5.1 (+2.6/- 4.1) <sup>a</sup>	24.3 (+1.7/- 1.4)	9.2 (+0.1/- 0.2)	16.3 (+1.2/- 2.4)	6.8 (+0.4/- 0.7)	12.9 (+0.8/- 0.8)
$\Delta_1$ ( $\text{cm}^{-1}$ )	3.5 (+1.1/-0.6)	---	2.1 (+1.3/- 0.4)	7.9 (+3.9/- 3.5)	4.0 (+0.6/- 0.9)	4.2 (+0.3/- 0.3)
$\tau_1$ (ps)	0.3 (+0.1/-0.1)	---	1.1 (+0.9/- 0.7)	32 (+23/-32)	41 (+83/-21)	1.2 (+0.6/- 0.3)
$\Delta_2$ ( $\text{cm}^{-1}$ )	8.9 (+1.2/-1.9)	---	---	---	---	---
$\tau_2$ (ps)	229 (+119/-88)	---	---	---	---	---

a. Values in parenthesis demonstrate positive and negative uncertainties as defined in the text.

The PANI-ES samples doped with CSA and DNNSA were each found to be well fit by two single exponential FFCFs centered at approximately the same frequencies as the two Gaussians needed to fit their respective CO FTIR spectra. The resulting FFCFs had similar  $\tau_1$  values of 1.1 and 32 ps (DNNSA doped) and 1.2 and 41 ps (CSA doped). For the DNNSA doped PANI-ES, the  $\Delta_1$ s are more heavily weighted toward the slower frequency fluctuations, whereas the FFCF decay components are equally weighted for the CSA doped films. The structural dynamics reported by the metal-bound CO in the doped films are nearly identical within the uncertainty of the fitted parameters. For all three PANI films, the fits to the data for  $T_w = 0.5$  and 10 ps are overlaid in Figure 4.4 as the solid lines to demonstrate the excellent agreement to the data, and the overlays to all data at all  $T_w$ s and all frequencies are provided in Figures 4.5, 4.6 and 4.7.

#### 4.4.5. Collective Interpretation of Results

It was noted above that the trends in the vibrational echo peak shifts do not correlate with the widths of the major components of the FTIR spectra. With the full datasets fitted, it is seen that the static term ( $\Delta_0$ ) for the major transition is smallest for the PANI-EB, consistent with the smaller peak shift. This concludes that the increased linewidth in the FTIR for PANI-EB is in fact due to a greater contribution from dynamic broadening, while the major components of the doped samples are more inhomogeneously broadened. This could be interpreted as a greater distribution of chemical environments in the PANI-ES films, however, this is not consistent with static structural models for PANI-EB and ES films. For example, PANI-EB has been shown to adopt a disordered arrangement of polymer chains with poor chain packing,<sup>226</sup> while



PANI-ES films are generally believed to contain a certain amount of molecular ordering that is induced by the dopant.<sup>202,206,224,225</sup> A lamellar structure of PANI-ES films has been reported, consisting of layers of polymer chains and dopants,<sup>206,207,209,217</sup> in which the polymer chains adopt more planar structures with smaller interchain separations than in PANI-EB films.<sup>202,227</sup> From these studies, it is expected that the structural model shown in Figure 4.8 to represent the undoped and doped PANI films. The increase in ordering upon doping to PANI-ES is accompanied by a decrease in the motional freedom for the polymer chains as their interchain spacings become compressed and the dopant interactions lock their planarity. It has also been reported by several groups that the increase in crystallinity measured in X-ray studies is due, at least in part, to crystallization of the dopant molecules.<sup>210,217</sup> Using this model, a more likely interpretation of the linear lineshapes and vibrational echo peak shifts is that the PANI-EB is structurally more disordered but dynamically less hindered to move and interconvert between its molecular configurations. Thus, it is possible that some of the slow dynamics that were captured (with some uncertainty) in the  $\tau_2$  of the FFCF for PANI-EB are slowed to the point of being included in the  $\Delta_0$ s in PANI-ES.

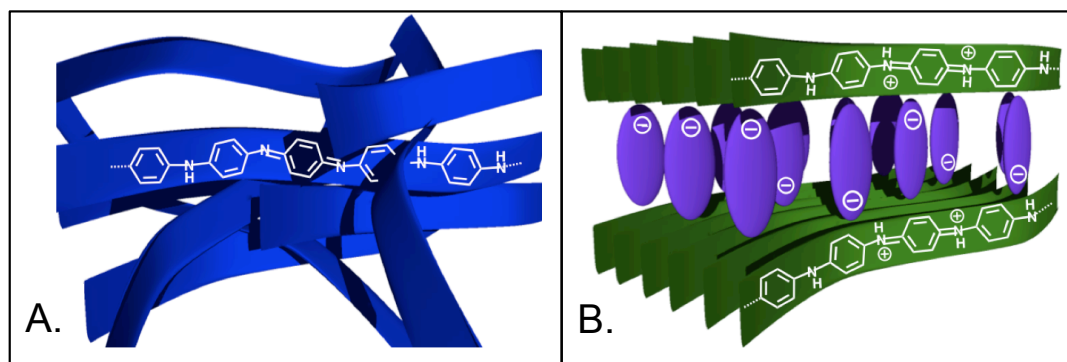


Figure 4.8: Structural models of (A) PANI-EB and (B) PANI-ES.

Comparing the FFCFs for the PANI-EB to those of the PANI-ES samples, it is apparent that the frequency fluctuations in the PANI-EB on the time scale of hundreds of fs are absent in the PANI-ES films. At the same time, the structural dynamics in the PANI-ES films are dominated by frequency fluctuations on the time scales of  $\sim 1$  ps and  $\sim 30$  ps, which are not present in PANI-EB. It is important to note that there is not always a one-to-one correspondence between the correlation function measured by a given technique and the time scales of the molecular dynamics from which it originates. Castner and Maroncelli demonstrated that the extent to which a particular observable reports on a molecular property depends on the nature of their coupling.<sup>228</sup> In 2D-IR VES, the dephasing processes induced by the solvation environment depend on the manner in which the CO oscillator missing vibrational energy levels are coupled to their surroundings. In this work, the electrostatic force model was invoked to describe this connection, wherein the coupling of molecular motions to vibrational frequencies occurs through the vibrational Stark coupling constant.<sup>229,230</sup> This parameter describes the frequency shift that would be expected based on a given electric field, and it has been used to accurately predict the vibrational echo decays for metal-bound COs in proteins from MD simulations.<sup>229</sup> The proximity of the surrounding molecular motions to the CO should play a role in determining their influence. The net electrostatic field that is experienced by the vibrational probe must have contributions from nuclei that reside at a range of distances, and the charged and more polar molecular fragments may have larger field contributions that could influence the CO frequency from a longer distance. It has been shown in 2D-IR VES studies on heme proteins that the metal-bound CO is influenced by the molecular motions of polar and nonpolar molecular

groups that are proximal to the oscillator, but is also affected by the motions of solvent dynamics up to 3 nm away.<sup>103,164</sup> These experiments serve as a reasonable basis for interpreting the results of the RuOEP-bound CO in these PANI films: through the fluctuating net electrostatic field, the probe is sensitive to the motions of proximal nuclei and, to a lesser extent, sensitive to motions up to a few nm away. The overriding assumption throughout this discussion is that the time scales of the frequency fluctuations that are recovered in the FFCFs are representative of the time scales of structural motions in the polymer films. While this correspondence is not always correct for the correlation functions obtained by other methods,<sup>228</sup> there is evidence to support this connection for 2D-IR VES.

Although the molecular origins of the dynamical changes in the PANI FFCFs cannot be assigned with the 2D-IR VES technique alone, the  $\tau_i$  values in Table 4.1 do provide some insight by characterizing the time scales over which these motions occur. If the time scales were directly correlated with molecular motions, these  $\tau_i$  values would correspond to low frequency inter- and intramolecular vibrations of 0.2 and 111  $\text{cm}^{-1}$  for PANI-EB, and  $\sim 1$  and  $\sim 30$   $\text{cm}^{-1}$  for both PANI-ES materials. One explanation for the absence of the 111  $\text{cm}^{-1}$  dynamics in the FFCFs of the PANI-ES films comes from the changes that occur in the structural ordering upon doping shown schematically in Figure 4.8. The PANI-ES films have more compact structural arrangements than PANI-EB that may consequently affect the torsional motions of the phenyl-rings and explain the absence of the fs time scale component in the FFCFs. In Chapter 3, a similar observation for the polymer dynamics in annealed films of poly(3-hexylthiophene) in which the absence of this fast hundreds of fs component was correlated with an increase

in charge carrier mobilities.<sup>32</sup> Low frequency ring-ring torsional vibrations have been calculated for poly(phenyl) and poly(thiophene) systems to be in the range of 60 to 130  $\text{cm}^{-1}$ .<sup>196-198</sup> Incoherent neutron scattering experiments by Sauvajol and coworkers on PANI-EB films reported that phenyl-ring librations also occur in this frequency range.<sup>231</sup> Zheng and coworkers have also predicted phenyl-ring wagging motions to occur with energies around a few hundred  $\text{cm}^{-1}$  for the fully reduced form of PANI.<sup>232</sup> These reports suggest that the absence of the 111  $\text{cm}^{-1}$  component from the PANI-EB may be due to a perturbing of the phenyl ring motions with respect to one another as the polymer chains are ordered into lamellar structures (Figure 4.8) and the material becomes more conductive. Ultimately, the restructuring of the polymer films upon doping could shift the frequencies of these dynamics to a regime to which we are insensitive.

At the outset, it was hypothesized that PANI-ES films with different dopants would have characteristically unique dynamics when the dopants produced films with different conductivities. The spacing between layers of the polymer chains (Figure 4.8) and the degree to which they are ordered is thought to depend on the degree of doping as well as the dopant chemistry.<sup>202,206-209,224,225</sup> Of the two dopants used in this study, CSA is reported to form more compact and ordered lamellar structures than DNNSA. The smaller, less bulky, structure of CSA and its ability to form hydrogen bonds to the PANI backbone have both been attributed to the tighter configuration.<sup>208,209</sup> However, the 2D-IR VES measurements of the dynamics reported by the metal-bound CO in these two PANI-ES films are nearly the same, having frequency modulation times of  $\sim 1$  ps and  $\sim 30$  ps. This suggests that the difference in charge carrier mobilities for PANI-ES

films with different dopants is not due to a difference in the structural dynamics that the 2D-IR VES technique is sensitive to in these films. Low frequency vibrations at 1.1 THz ( $37\text{ cm}^{-1}$ ) have been theoretically predicted to be particularly detrimental to carrier mobilities.<sup>83</sup> Laarhoven and coworkers reported that structural motions in pentacene thin films in this frequency regime were highly correlated to charge carrier mobilities and affected the probability of charge transfer events.<sup>35,83</sup> It is interesting that the FFCFs of both of the conducting PANI-ES films studied in this work share a dynamic component with a frequency of approximately  $30\text{ cm}^{-1}$ , very close to the predicted frequency that would greatly hinder charge mobilities through these films. Thus, although a dynamic signature of improved charge mobilities for the DNNSA compared to CSA doped films was not found, the appearance of dynamics with the potential to limit the conductivities in both materials was uncovered.

## 4.5. Conclusions

In this chapter, the ultrafast structural dynamics of PANI in its undoped semiconducting (PANI-EB) and doped conducting (PANI-ES) forms were characterized with 2D-IR VES measurements. By introducing a vibrational dynamics probe into three different PANI films (PANI-EB, PANI-ES doped with DNNSA, and PANI-ES doped with CSA), the structural dynamics in films with varying degrees of conducting ability were examined. It was found that intricate details that are otherwise buried beneath the inhomogeneous FTIR lineshape can be recovered with this approach, and that the results provide information that could not be obtained without the use of this nonlinear technique. Structural motions occurring on the time scale of a few hundred fs were observed only in the undoped PANI-EB films. The absence of these dynamics in

the data from the doped PANI-ES films suggests a perturbation of ring-ring torsional or chain wagging motions due to the more compact molecular architecture induced by the dopants. This clearly demonstrates that a change in material conductance through doping can be accompanied by a change in the time scales of structure motions detectable by 2D-IR VES measurements. The resulting structural dynamics in both types of the doped PANI-ES films occurred on the ps to tens of ps time scales, and no significant dynamical differences between the DNNSA and CSA doped materials were found, despite their established differences in conductivity. This demonstrates that, in some cases, an improvement in electrical performance may not have its origins in a dynamical change. However, it is intriguing that a dynamical component was revealed in both of the doped PANI-ES materials with a modulation time that coincided with that predicted to be particularly detrimental to charge transport. This may indicate that a dynamical barrier to conduction exists in these doped films, and that overcoming this obstacle could yield materials with greatly enhanced mobilities.<sup>c</sup>

---

<sup>c</sup> The authors gratefully acknowledge funding from the Donors of the American Chemical Society Petroleum Research Fund for partial support of this research (46628-G6). We also acknowledge the 3M Corporation Nontenured Faculty Award, a Grant-in-Aid from the University of Minnesota, Twin Cities, and partial support by the National Science Foundation under CHE-0847356.

## Chapter 5

# Static and Dynamic Structural Memory in Polyaniline Thin Films

Reproduced in part with permission from:

Audrey A. Eigner, Brynna H. Jones, Bryce W. Koprucki, and Aaron M. Massari. Static and Dynamic Structural Memory in Polyaniline Thin Films. *Journal of Physical Chemistry B*. **2011**, 115, pp. 8667 – 8812.

Copyright, 2010 American Chemical Society.

## 5.1. Chapter Summary

In this chapter, steady-state UV-visible and FTIR spectroscopies were used to characterize the electronic and structural changes that occur in polyaniline (PANI) thin films over the course of a single deprotonation and re-protonation cycle. The dedoping from the emeraldine salt (PANI-ES) to the emeraldine base (PANI-EB) form was achieved by treatment with a weak base (ammonia gas), and the PANI-ES was recovered by exposure to humid air and then dry air. The spectroscopic changes were classified into two general categories: those in which the recovered sample features were intermediate to the initial PANI-ES and the deprotonated PANI-EB, and those in which the recovered sample features changed monotonically from the starting PANI-ES towards a unique observable. Two-dimensional IR vibrational echo spectroscopy (2D-IR VES) was then used to demonstrate that ultrafast structural dynamics on the time scales of hundreds of femtoseconds to a few picoseconds could also be organized into these two categories. In contrast, it was found that the slower dynamics on the tens of ps time scale appear unperturbed by the dramatic structural changes of the dedoping-redoping cycle. The relevance of these dynamics to charge mobilities in the initial and final PANI-ES states are discussed and compared their behavior to the film electrical resistances over the course of the protonation cycle. The results show that specific structural dynamics are correlated with changes in the film conductivities and that PANI films have a memory of not only the static molecular structures of the as-cast materials, but also of some of the dynamics that are inherent to those morphologies.



## 5.2. Introduction

The most successful organic electronic materials strike an optimal balance between processability and charge mobility. The inter- and intra-molecular forces that hold these substances together must be weak enough that they are soluble in common volatile solvents, yet strong enough to maintain electronic communication for efficient charge transport in the final product.<sup>22,56</sup> The conductivities of amorphous and semi-crystalline polymeric thin films can be further tuned after film deposition through treatments that alter their crystallinity, morphology, and in some cases, the degree of phase segregation.<sup>16,18,32,133,153,154,156,157</sup> The ability to post-process these materials in this manner arises from kinetic trapping of molecular configurations away from their thermodynamic minima during solvent evaporation. Post-processing then provides an additional level of control over the final electronic properties of the thin films without sacrificing the desired solution processability. Thermal and solvent vapor annealing have been used to optimize the charge carrier mobilities through organic films<sup>18,32,133,153,154,156,157</sup> and to drive phase segregation in blended organic photovoltaics,<sup>16</sup> while in other cases the morphological changes induced by an analyte have been exploited to produce conductance-based sensors.<sup>10,11,233-235</sup> Although these effects have similar molecular origins, annealing generally seeks permanent adjustments, whereas sensing ideally involves reversible changes. Thus, depending on the application of an organic material, it is important to understand not only how such post-processing treatments alter material morphologies and carrier mobilities, but also the extent to which these changes can be reversed. Both static (time-averaged) and dynamic (time-dependent) molecular configurations can affect the transport of charge

carriers (electrons or holes) through organic thin films. In Chapter 2, 2D-IR spectroscopy was used to demonstrate that the structural dynamics in semiconducting poly(thiophene) films are notably different before and after solvent vapor annealing in conjunction with a 30% increase in hole mobility.<sup>32</sup> However, the morphological changes induced by the post-processing treatment in that work were irreversible and did not test for evidence of dynamic structural memory effects on the ultrafast time scale.

Owing to its unique combination of conductivity and processability, polyaniline (PANI) is an organic electronic material that has a long history of studies devoted to understanding the relationship between its structure and electrical function.<sup>200-202</sup> PANI can exist in several oxidation and protonation states, each of which has its own unique electronic properties. Two of the most commonly studied forms, the half-oxidized emeraldine salt (PANI-ES) and emeraldine base (PANI-EB), are shown in Scheme 1. PANI-ES is a cationic conducting polymer that can be readily converted to the semiconducting neutral PANI-EB form by deprotonation with a weak base.<sup>11,235,236</sup> During the dedoping process, dramatic changes are observed in the optical, electrical, and structural properties of the polymer as its morphology adjusts to the chemical changes to its backbone. It is generally believed that the conversion of PANI-ES to EB leads to a decrease in the ring planarity along the conjugated backbone and a disordering of the polymer chains from their as-cast structures.<sup>221-223</sup> The reversibility of these changes can also be tested since the PANI-EB can be readily reverted to the PANI-ES by protonation with a variety of organic acids.<sup>202,206-210</sup>

The chemical reactivity of PANI-ES films enables them to serve as sensitive and reversible detectors of many volatile compounds, including ammonia gas (NH<sub>3</sub>).<sup>10,11,235-</sup>

<sup>237</sup> Lubentsov and coworkers reported changes in the resistance of PANI films treated with various concentrations of water vapor and NH<sub>3</sub> gas,<sup>236,237</sup> and Kukla and coworkers later showed that these resistive effects could be completely reversed with a thermal treatment.<sup>11</sup> More recently, Verma and coworkers described the use of PANI-ES films doped with camphor sulfonic acid (CSA, shown in Scheme 1) as potentially more efficient NH<sub>3</sub> based sensors due to their unique hexagonal structure.<sup>10</sup> The chemical reaction of NH<sub>3</sub> with CSA doped PANI-ES is shown in Scheme 1. As the NH<sub>3</sub> deprotonates the polymer backbone, the resulting NH<sub>4</sub><sup>+</sup> is retained in the film and is stabilized by the CSA anion.<sup>236,237</sup> These electronic and morphological changes are the source of the conductivity changes in response to NH<sub>3</sub> gas. The PANI-ES/EB system can therefore serve as a useful model to study the impact of reversible or quasi-reversible morphological changes in conducting polymers on the static and dynamic structural properties and their connections to electrical conductivity.

In this chapter, steady-state UV-visible and FTIR spectroscopies were used to measure the static structural perturbations upon cycling the protonation and conductivity of PANI thin films with a weak base and weak acid. These results are compared to the concurrent changes in the ultrafast structural dynamics as reported by 2D-IR vibrational echo spectroscopy (2D-IR VES) and transient grating measurements. The thin film resistances were also monitored during the redox cycling process to relate the static and dynamic structural parameters back to the electrical performances of the PANI material at each stage. Intriguingly, it was found that some of the observed static and dynamic changes are partially reversible, while others change in a monotonic fashion and lead to entirely unique final products after the dedoping-redoping cycle.

## 5.3. Experimental

### 5.3.1. Materials

Polyaniline (emeraldine base) (MW=10kD), camphor-10-sulfonic acid  $\beta$  (98%), and 2,3,7,8,12,13,17,18-octaethyl-21*H*,23*H*-porphine ruthenium(II)carbonyl (RuOEP) were used as received from Sigma-Aldrich. Ammonia gas (pure, anhydrous) was used as received from Matheson Gas Products. All solvents were reagent grade and were used as received without further purification.

### 5.3.2. Preparation of PANI-ES films doped with CSA

A solution containing a 1:3 mole ratio of PANI-EB (four ring repeat unit) to CSA was prepared by dissolving 10 mg of PANI-EB and 19 mg of CSA in 2 mL of chloroform. This solution was stirred for approximately 3 hrs and then filtered through a 0.45  $\mu\text{m}$  syringe filter to remove particulates. A separate solution consisting of 15 mM RuOEP and 100 mM pyridine in 1 mL of methylene chloride was prepared. The methylene chloride was allowed to evaporate under low vacuum and heat (50°C), and the remaining solid was redissolved in 1 mL chloroform. This solution was then 0.45  $\mu\text{m}$  filtered, and a 100  $\mu\text{L}$  portion was added to the original PANI/CSA solution. A 350  $\mu\text{L}$  aliquot of the final solution was then spin coated at 50 rpm for 4 min on a 1 inch  $\text{CaF}_2$  window to produce a PANI-ES film. RuOEP was added to the films in this work to incorporate a small concentration of a particularly strong vibrational mode (metal-bound CO) that could be used as a probe for structural dynamics in the 2D-IR VES experiments. Chapter 4 has shown that the addition of porphyrin at low concentrations (1:10 RuOEP:PANI m/m in this work) does not significantly alter polymer film attributes.<sup>32</sup> Pyridine was ligated to the sixth coordination site on the ruthenium to

prevent RuOEP aggregation and  $\text{NH}_3$  ligation.

### **5.3.3. Dedoping of PANI-ES films to PANI-EB with $\text{NH}_3$ gas**

A CSA-doped PANI-ES film on a  $\text{CaF}_2$  window was sealed in a cell with a second  $\text{CaF}_2$  window and a rubber o-ring (1" outer diameter, 3/4" inner diameter), forming an air pocket over the polymer film. Anhydrous  $\text{NH}_3$  gas (0.5 mL) was collected in a syringe, diluted with 2.5 mL of room air, and then injected into the air pocket above the PANI-ES sample by inserting the syringe through the o-ring. The polymer film changed quickly from the PANI-ES characteristic green to the PANI-EB characteristic blue color. The sample was allowed to react with the  $\text{NH}_3$  gas for at least an hour and then remained in the sealed  $\text{NH}_3$  atmosphere for all spectroscopic measurements (typically 48 hours).

### **5.3.4. Recovering PANI-ES films**

To recover each CSA-doped PANI-ES film after the  $\text{NH}_3$  treatment, the sample cell was opened to ambient room air. A small amount of warm water (near reflux) was poured into a petri dish, and the PANI-ES film and the petri dish were placed together under a glass covering for 1-2 minutes. This brief exposure to humid air was necessary to recover the PANI-ES on a reasonable time scale. The samples were then dried in an atmosphere of dry air (-100 °F dew point) for 12-24 hours before measurements were performed. Repeated brief exposures to the humid and dry air were found to have no additional effects on the spectroscopic measurements described below.

### **5.3.5. Resistance Measurements**

Film resistances were measured by a two-point probe method using a Keithley 617 electrometer. A home-built two-point probe head was constructed from a rubber

stopper, copper wire, and copper foil. The contacts were constructed of 14 mm long copper foil strips maintained at 1 mm apart and placed in contact with the PANI films. Ohmic contact was made to the copper foil strips through copper wires embedded in the rubber stopper. To ensure that reproducible contact was made with the electrodes and polymer films, a 2 kg weight was placed on top of the probe assembly while measurements were taken. Resistance measurements were performed on eight PANI samples at each of the three protonation states. The reported values were the average resistances over 10 minutes under ambient conditions after a brief equilibration period.

### **5.3.6. Linear Spectroscopy**

UV-visible measurements were performed on a Cary-14 spectrophotometer (modified by On-Line Instrument Systems, Inc), and IR absorbance spectra were collected on a Nicolet 6700 FTIR spectrometer (Thermo Scientific) as an average of 16 scans with a resolution of  $2\text{ cm}^{-1}$ .

### **5.3.7. 2D-IR VES**

The 2D-IR VES technique employed in this work has been described previously (refer to Section 3.3.4.).

## **5.4. Results and Discussion**

### **5.4.1. UV-vis of thin films during treatment cycle**

The UV-visible and FTIR spectra, as well as the 2D-IR VES and resistance measurements, were collected for PANI thin films at three points during a post-processing treatment cycle (Figure 5.1). Initially, data were measured on as-cast CSA-doped PANI-ES films that are categorized as emeraldine salt I (ES-I), as defined by MacDiarmid and coworkers for samples that are cast in the protonated form (whereas

ES-II PANI is cast as EB and then converted to ES).<sup>238</sup> Films of this type are reported to be semi-crystalline with crystallinities reaching up to 50% for certain preparation conditions.<sup>225,238</sup> After being exposed to  $\text{NH}_3$  gas and converted to the PANI-EB-I form, data were again collected on the films. At this stage of the cycle, the polymer had been deprotonated and the film was semiconducting, despite the continued presence of CSA. Lastly, following exposure to humid and dry air the films were returned to the PANI-ES state, where the final measurements were made.

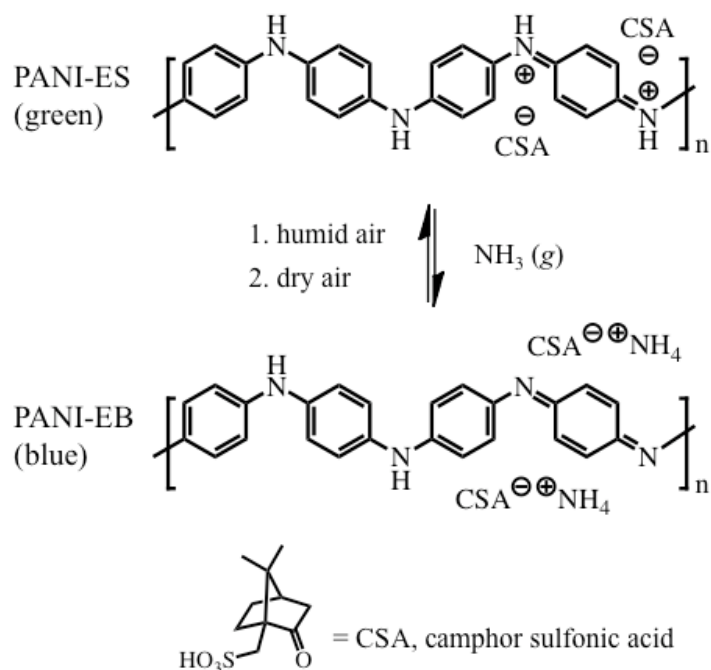


Figure 5.1: Protonation cycle of CSA-doped emeraldine PANI.

The UV-visible spectrum of an as-cast PANI-ES film is shown in Figure 5.2 (black trace), and has the characteristic broad PANI absorbances near 400 nm (polaron to  $\pi^*$  transition) and 800 nm ( $\pi$  to polaron transition).<sup>220</sup> This trace and each of the other traces in this figure also show narrow peaks at 395, 518, and 550 nm. These bands are due to the RuOEP that was incorporated into the films for the vibrational dynamics

measurements described below, which, despite a low concentration, has a large extinction coefficient relative to PANI.<sup>218,219</sup> The position and width of the as-cast PANI-ES localized polaron absorption band at 805 nm suggests a primary doping mechanism in which the benzenoid and quinoid rings on adjacent polymer chains interact in a non-planar fashion due to an abundance of ring-ring torsional defects along the polymer backbone.<sup>221-223</sup> Zheng and coworkers have described the structural arrangements associated with the primary doping mechanism as a ‘tight-coil’ molecular configuration.<sup>223</sup> In this work, the presence of primary doping in our polymer samples was expected due to the fact that a volatile solvent was used to cast the films.

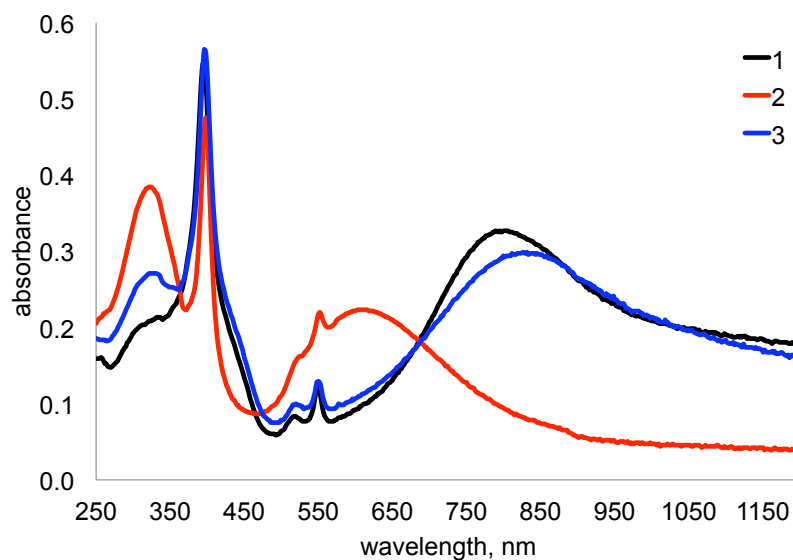


Figure 5.2: UV-visible spectra of as-cast CSA-doped PANI-ES (1), PANI-EB dedoped with  $\text{NH}_3$  gas (2), and recovered PANI-ES (3).

Upon treatment of the as-cast PANI-ES film with  $\text{NH}_3$  gas, the polymer was deprotonated (Figure 5.1) and notable changes occurred in the UV-visible spectrum (Figure 5.2). The lowest energy absorption band in the  $\text{NH}_3$  treated PANI-EB spectrum is centered at 610 nm ( $\pi$ - $\pi^*$  transition of quinoid rings), while the higher energy band is



centered at 325 nm ( $\pi$ - $\pi^*$  transition of benzenoid rings).<sup>220</sup> It has been noted that the conversion of ES-I type PANI to EB-I results in a nearly amorphous material,<sup>225</sup> thus it is expected that the  $\text{NH}_3$  treatment induced morphological adjustments and a loss of crystallinity that contributed to the observed spectral changes.

After humid and then dry air treatments to recover the PANI-ES state, the UV-visible spectrum of the recovered sample (Figure 5.2) shows similar, but not identical, absorption bands to those of the original as-cast PANI-ES. The lowest energy absorption in the recovered PANI-ES film is red-shifted to 830 nm. This is still reflective of a primary doped ‘tight-coil’ morphology, but indicates a more relaxed structure (moving towards the ‘expanded-coil’ limit) with increased ring planarity and a more delocalized excited state.<sup>221-223</sup> It is also noteworthy that the higher energy absorbance in the recovered PANI-ES sample appears to have a mix of the 400 nm band that is associated primarily with PANI-ES and the 325 nm band that is associated predominantly with PANI-EB. The changes in the higher energy absorption bands (300-400 nm) demonstrate that portions of the recovered PANI-ES films are chemically intermediate to the as-cast PANI-ES and  $\text{NH}_3$ -treated PANI-EB films, whereas the changes in the low energy polaron absorbance near 800 nm show that the recovered PANI-ES is in other ways structurally different and unique from either of the other forms.

#### **5.4.2. FTIR of thin films during treatment cycle**

The FTIR spectra of the PANI samples in Figure 5.3 provide additional information about the time-averaged structures and morphologies in these films. Similar to the electronic absorption spectra in Figure 5.2, certain features of the FTIR

spectra indicate that the PANI film structures after the dedoping-redoping cycle are partially reversed, while others suggest a monotonic change of the film microstructure to one that is unlike that of the starting PANI-ES material. The full range FTIR spectra in Figure 5.3A show a broad free electron absorbance in both the initial and recovered PANI-ES traces (black and blue lines, respectively) that is absent in the undoped PANI-EB spectrum (red line). The intensity of this delocalized polaron band has been correlated with charge carrier mobilities,<sup>239-242</sup> and thus was expected to be absent in the NH<sub>3</sub> treated PANI-EB film. For the recovered PANI-ES film, the magnitude of this absorbance is less than that of the as-cast PANI-ES, suggesting that the recovered film is not as conductive as the original film.

The spectral region that encompasses the C=C stretching vibrations of the benzenoid ( $\sim 1500\text{ cm}^{-1}$ ) and quinoid ( $\sim 1600\text{ cm}^{-1}$ ) ring moieties (Figure 5.3B)<sup>239-242</sup> also indicates that the PANI structure after the dedoping-redoping cycle is not completely reversed. The quinoid region in the initial PANI-ES spectrum consists of a broad structured band, which provides evidence for heterogeneous chemical environments and non-uniform doping. After dedoping to PANI-EB with NH<sub>3</sub>, these bands convert to a single narrow Gaussian peak, suggesting a more homogeneous environment. As shown in Figure 5.1, the EB form has electron density that is localized on either benzenoid or quinoid rings, while the electron density of the protonated ES form may delocalize over several rings to stabilize the polaron. As a result, the PANI-ES films have a distribution of ring structures that causes the multiple peaks in the as-cast PANI-ES spectrum. In the recovered PANI-ES spectrum (Figure 5.3B), the quinoid region again consists of

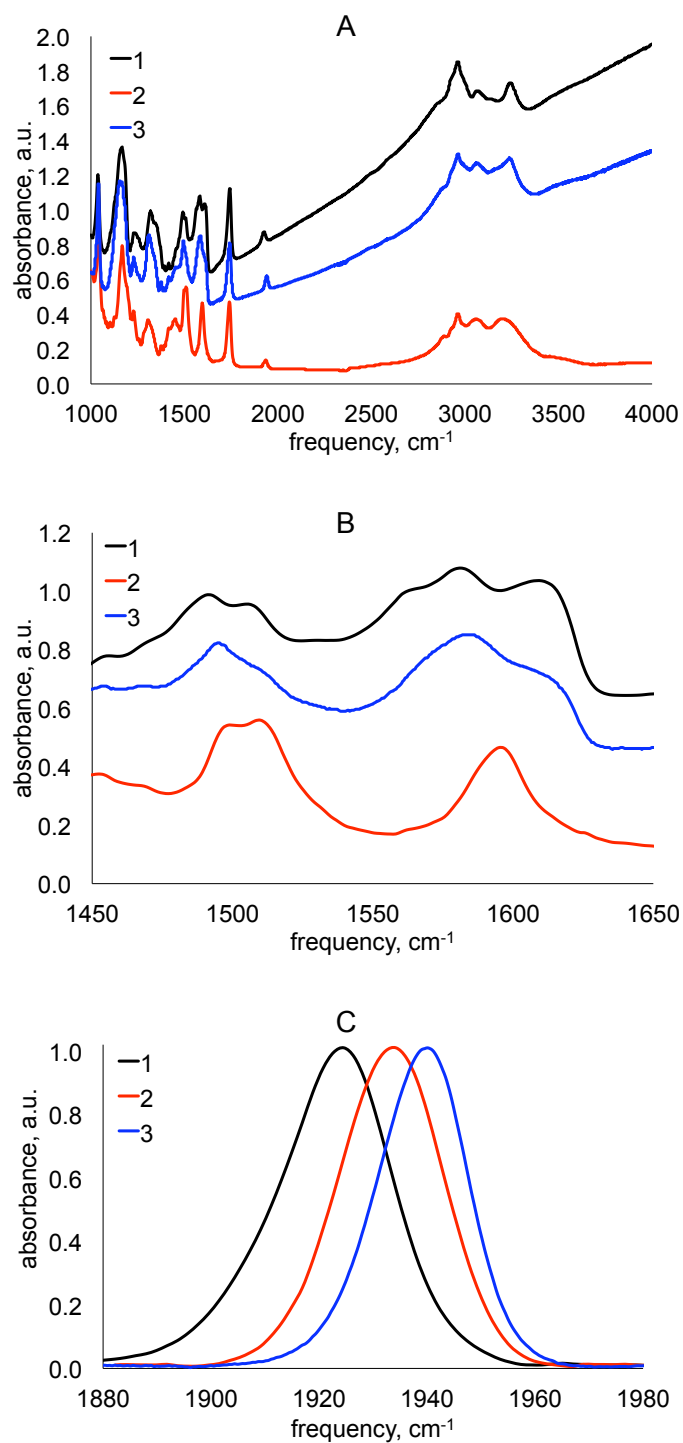


Figure 5.3: (A) Full scale FTIR spectra of as-cast PANI-ES [1], NH<sub>3</sub>-dedoped PANI-EB [2], and recovered PANI-ES [3]. (B) Same spectra as in (A) but focused on the C=C vibrational frequencies, and (C) the RuOEP-bound CO (baselined and normalized).

of broad structured peaks; however, the distribution and spectral fine-structure are different than in the initial PANI-ES spectrum. In the benzenoid region, there are two peaks ( $1496$  and  $1510\text{ cm}^{-1}$ ) that vary in intensity with respect to one another in the three sample types. The higher energy peak in the initial ES film is more intense than the lower energy peak while the reversed trend is observed in the EB film. The recovered PANI-ES film shows an intensity ratio for the two peaks that more closely resembles the as-cast PANI-ES, implying a final structure that is somewhat like that of the starting material. Similar to what is observed in the quinoid C=C bands, the benzenoid C=C absorbances in the recovered PANI-ES films are generally more narrow than those of the as-cast films, showing a decrease in the distribution of chemical environments.

The UV-visible and FTIR spectroscopic data shown thus far present a scenario in which the polymer morphology undergoes dramatic changes during the dedoping-redoping cycle. Certain metrics examined, such as the polymer electronic transitions and delocalized polaron absorbances, reflect partially reversible changes that result in a recovered system that is intermediate to the ES and EB endpoints. In contrast, the C=C FTIR peak widths and fine structure and the localized polaron absorption band ( $805\text{ nm}$ ) suggest a material that is monotonically altered from its original form in a way that makes it distinct from either of the parent forms. A structural memory effect is well-documented for PANI films.<sup>221,225,238,243</sup> In particular it is known that PANI films prepared in either of the two morphological categories (I or II) tend to not interconvert, even with repeated cycling of the polymer protonation state (EB to ES, or vice versa).<sup>225,238</sup> Hence there is a structural memory of the conditions that were used to

prepare PANI materials. X-ray studies by Maron and coworkers have also shown that the structural history in some PANI films is not completely preserved; often the *intrachain* structure is reversibly altered while *interchain* ordering is irreversible.<sup>226</sup> The presence of both reversible and monotonic changes in the spectra presented thus far corroborates this model, and implies that these categories may be associated with the intra- and interchain structures, respectively.

A comparison of the ruthenium-bound CO vibrational mode of the incorporated RuOEP in each of the three samples is shown in Figure 2c. The CO peak in the as-cast sample is centered at  $1924\text{ cm}^{-1}$  with a FWHM of  $22\text{ cm}^{-1}$ . The peak center shifts to  $1934\text{ cm}^{-1}$  with a FWHM of  $21\text{ cm}^{-1}$  after treatment with  $\text{NH}_3$ , and then shifts further to  $1940\text{ cm}^{-1}$  with a FWHM of  $18\text{ cm}^{-1}$  after recovering the PANI-ES polymer. The behavior of this CO band, which is sensitive to its local solvation environment, is consistent with the spectroscopic features described above in which the final molecular configurations around the CO are not intermediate to either the as-cast PANI-ES or the PANI-EB samples. The frequency shifting of this CO absorption is unidirectional and there is a slight but progressive narrowing of the inhomogeneous lineshape, which implies that the chemistry in the vicinity of the CO oscillators has become increasingly homogeneous during the dedoping-redoping cycle. For a given polymer configuration solvating the RuOEP-bound CO, the collection of partial atomic charges results in a net electrostatic field that induces a solvation shift in the IR absorption frequencies of the CO oscillators through the vibrational Stark effect.<sup>132</sup> The instantaneous normal modes ( $1\text{-}300\text{ cm}^{-1}$ ) in the room temperature PANI film cause this net electric field to fluctuate, thereby modulating the CO vibrational frequencies with time. These dynamics cannot

be extracted from the FTIR spectra alone due to inhomogeneous broadening, however nonlinear spectroscopic approaches, such as the 2D-IR VES measurements used in this study, are able to recover these dynamics. Since this CO vibration serves as a handle for both the static and dynamic structure of the PANI films, it is reasonable to predict from the FTIR spectra in Figure 2c that the polymer should have some dynamics that are also changed in a monotonic manner. However, it is also known that metal-bound CO oscillators can serve as global dynamical probes, sensing solvation dynamics in heme proteins as far as 2-3 nm away.<sup>164,229</sup> Thus, the partially reversible changes in the data in Figures 1 and 2 could also lead to dynamic components reported by the ruthenium-bound CO that are intermediate to the as-cast PANI-ES and NH<sub>3</sub>-dedoped PANI-EB.

#### 5.4.3. 2D-IR VES of thin films during treatment cycle

Figures 5.4, 5.5, and 5.6 show the full 2D-IR VES data sets. For comparison, 5.7A shows the spectrally-resolved vibrational echo decays collected at  $T_w = 0.5$  ps for the as-cast PANI-ES (1), the NH<sub>3</sub> treated PANI-EB (2), and the recovered PANI-ES (3) films, each measured at its respective center FTIR absorption frequency. The rates of the vibrational echo decays for the three films are noticeably different, becoming progressively slower as the sample is dedoped with NH<sub>3</sub> and then recovered to PANI-ES. Qualitatively, it can be said that with each step in the dedoping-redoping cycle, the dephasing of the CO oscillators becomes slower. Control studies that included injection of only ambient air (no NH<sub>3</sub>) and brief exposures to humid air without exposure to NH<sub>3</sub> gas were found to have no effect on the vibrational echo decay times (Figure 5.8). In Figure 5.8, “initial” represents the vibrational echo decay taken at 1925 cm<sup>-1</sup> for as-cast

CSA-doped PANI-ES. A volume of ambient air, equal to the volume of  $\text{NH}_3$  gas plus air that was injected to dedoped samples, was injected to test for changes in the decays due to pressure increases (labeled “pressure”). An as-cast PANI-ES sample also was exposed to the humid air followed by dry air treatment, the same treatment used to recover the dedoped samples, to test for changes in dynamics caused by the humidity treatment alone (labeled “humid”). It is clear that the progressive slowing of the vibrational echo decays during the dedoping-redoping cycle (Figures 5.7A and 5.7B) does not occur with these control experiments. However, the connection between the dephasing rate and the system dynamics is not always intuitive, as will be explained in more detail below. All of the decays in Figure 5.7 have accidental degeneracy beats, which result from strongly coupled anharmonic energy levels.<sup>189</sup> In systems in which the inhomogeneous linewidths are comparable to the vibrational anharmonicity, vibrational echo signals emitted from higher transitions (i.e.  $v = 1-2$ ) may have frequencies that coincide with those of lower transitions (i.e.  $v = 0-1$ ) causing a modulation in the spectrally-resolved echo intensity at the difference in their frequencies (anharmonicity). Since the anharmonicities and the FTIR linewidths in Figure 5.3C are only slightly different (see Table 5.1), the oscillation depths on the decays of the three samples are similar.

The vibrational echo signals reach their maximum intensities at  $\tau = 0.65$  ps for the initial and  $\text{NH}_3$  treated films, and at  $\tau = 0.8$  ps for the recovered PANI-ES film at  $T_w = 0.5$  ps (Figure 5.7A). The shift of the vibrational echo peak away from  $\tau = 0$  is an indication of molecular dynamics that occur on time scales that are either too fast or too slow to be resolved at a given  $T_w$ . For solid-state films like those examined in this

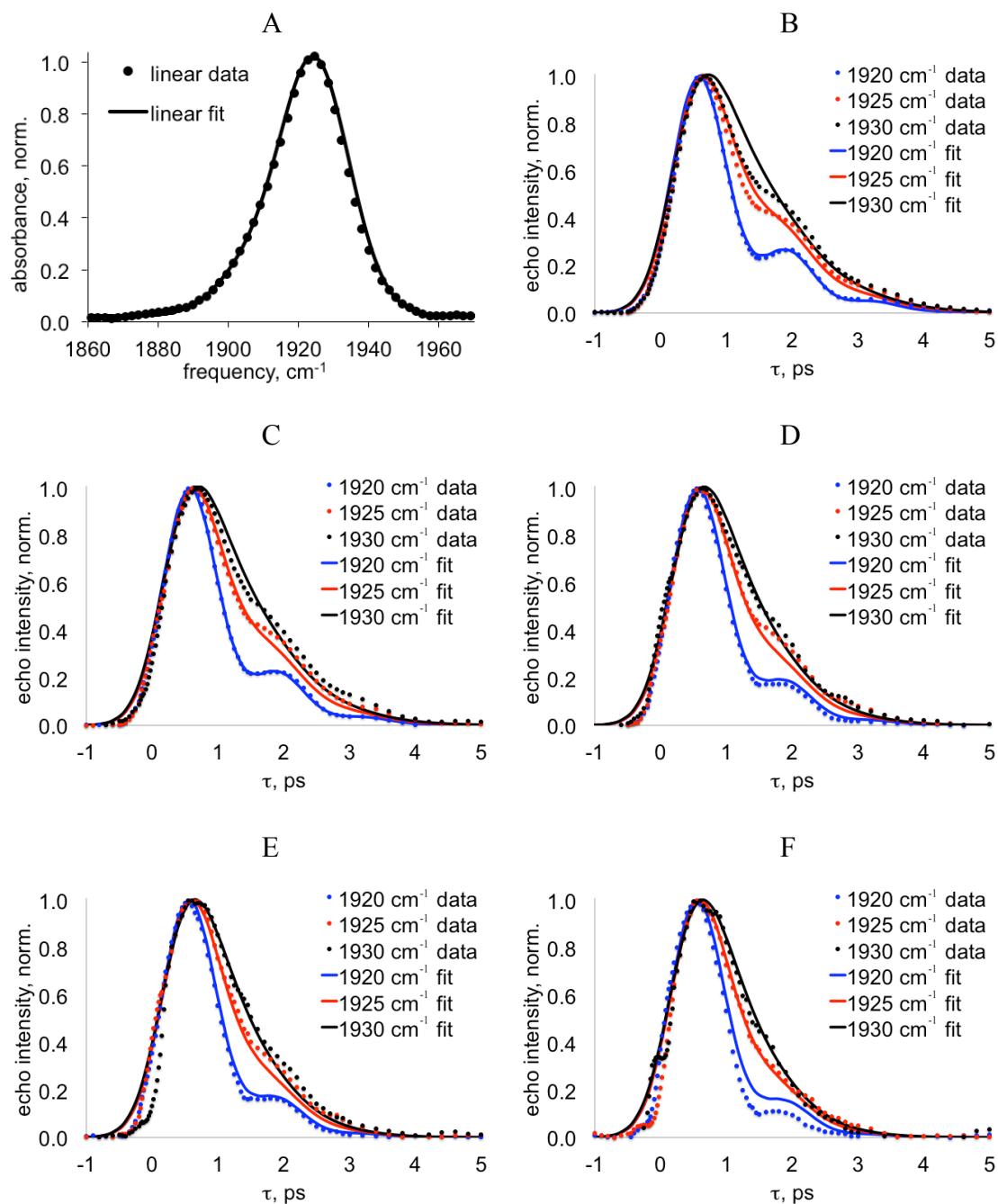


Figure 5.4: Full 1D- and 2D-IR VES data sets for RuOEP in as-cast PANI-ES. Data are shown as points and fits are shown as solid lines for the (A) linear, (B)  $T_w = 0.5$ , (C)  $T_w = 2$ , (D)  $T_w = 5$ , (E)  $T_w = 10$ , and (F)  $T_w = 15$ . The parameters used to generate these fit curves are those shown in Table 5.1.



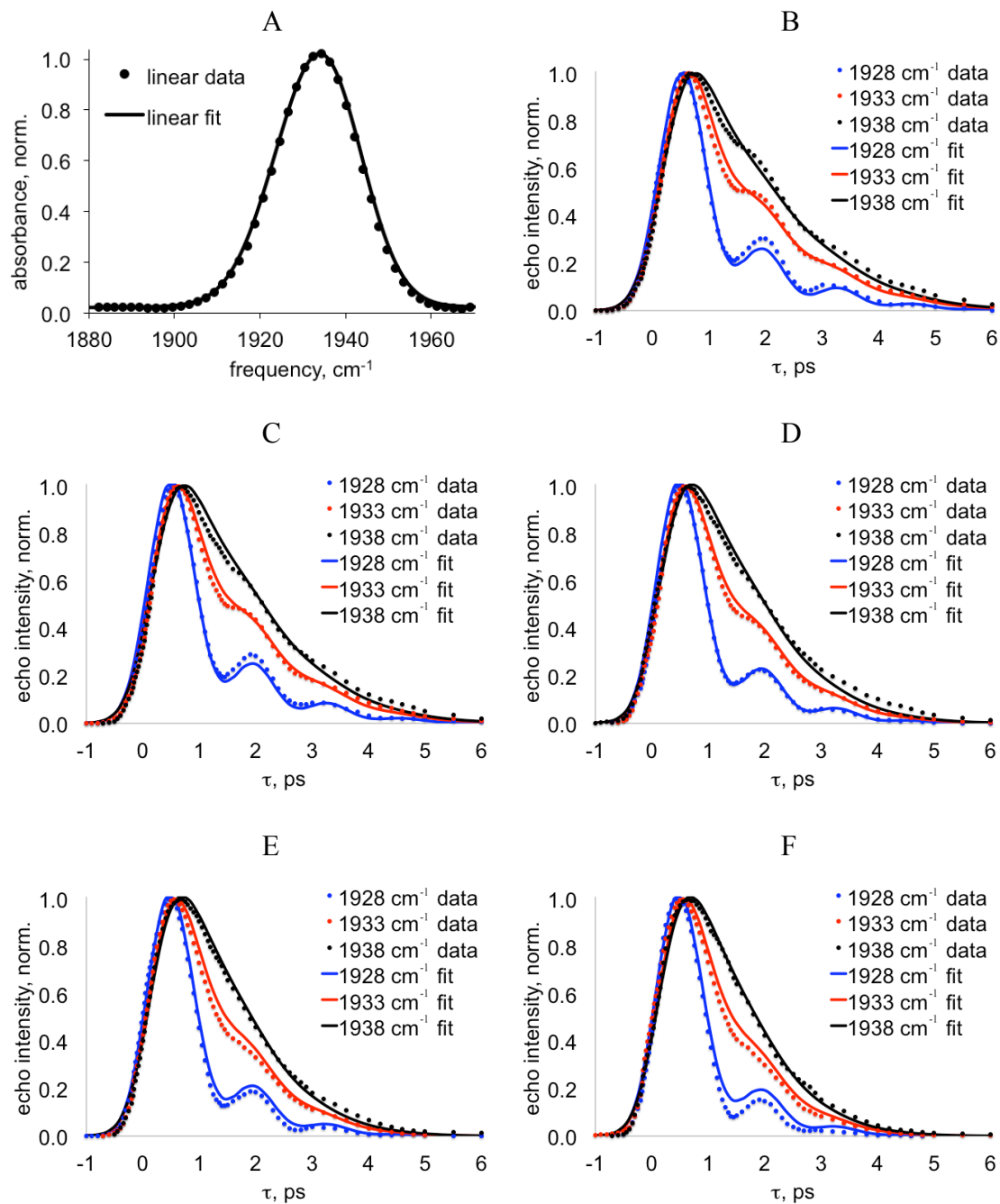


Figure 5.5: Full 1D- and 2D-IR VES data sets for RuOEP in PANI-EB. Data are shown as points and fits are shown as solid lines for the (A) linear, (B)  $T_w = 0.5$ , (C)  $T_w = 2$ , (D)  $T_w = 5$ , (E)  $T_w = 10$ , and (F)  $T_w = 15$ . The parameters used to generate these fit curves are those shown in Table 5.1.

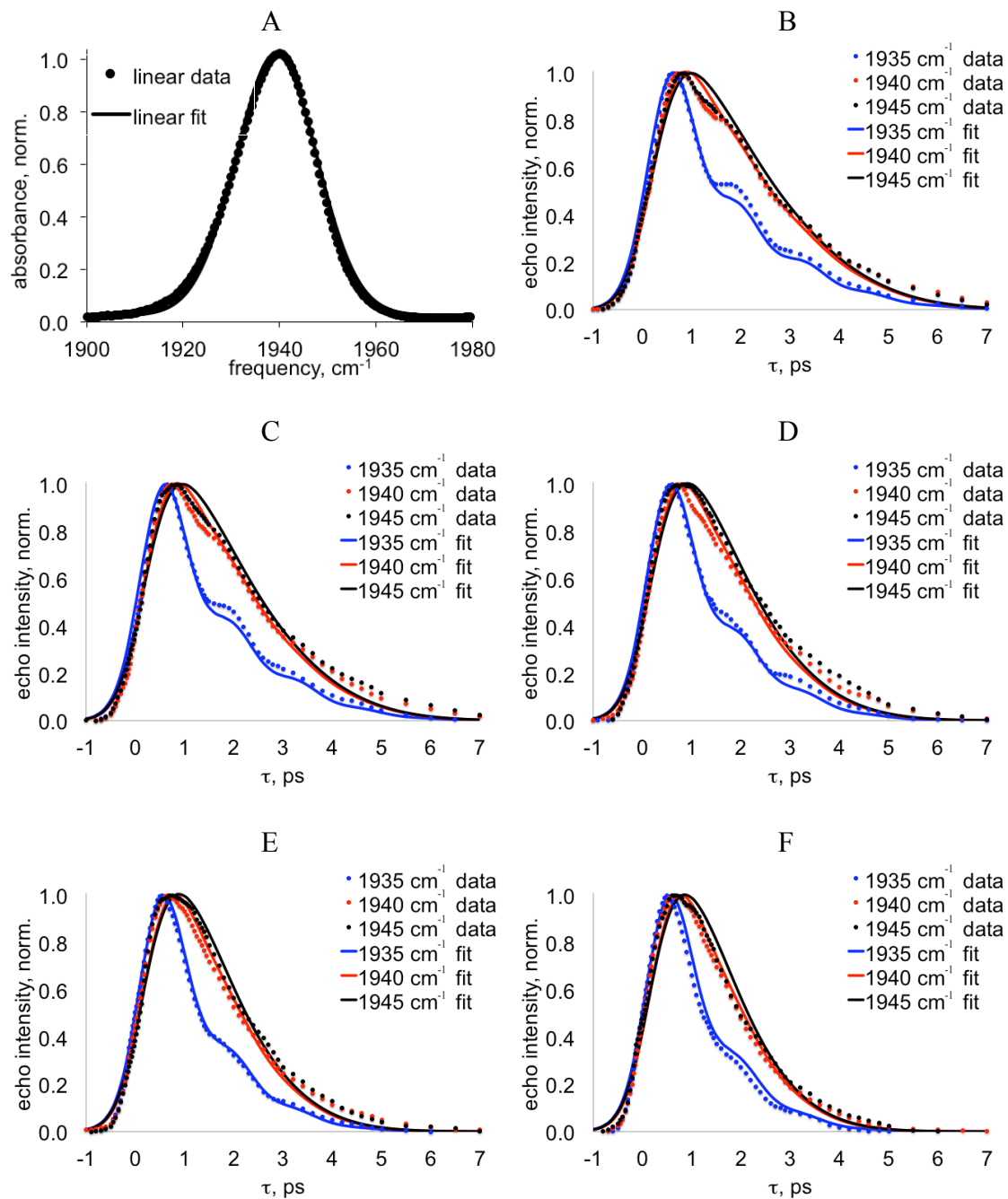


Figure 5.6: Full 1D- and 2D-IR VES data sets for RuOEP in recovered PANI-ES. Data are shown as points and fits are shown as solid lines for the (A) linear, (B)  $T_w = 0.5$ , (C)  $T_w = 2$ , (D)  $T_w = 5$ , (E)  $T_w = 10$ , and (F)  $T_w = 15$ . The parameters used to generate these fit curves are those shown in Table 5.1.

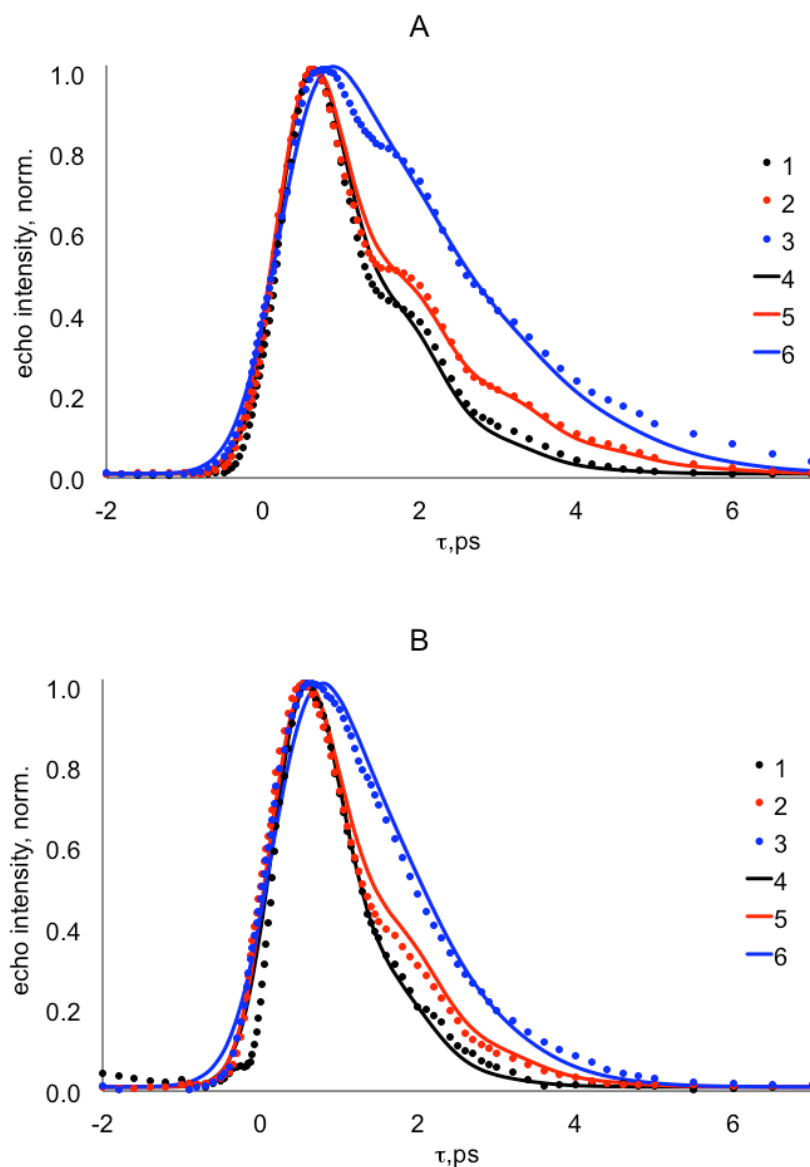


Figure 5.7: Spectrally-resolved vibrational echo decays collected for as-cast PANI-ES [1], PANI-EB [2], and recovered PANI-ES [3] measured at the CO vibration center frequencies of 1925, 1933, and 1940  $\text{cm}^{-1}$ , respectively, and at (A)  $T_w = 0.5$  ps and (B)  $T_w = 10$  ps. Experimental data are shown as markers and calculated fits to the data based on FFCF parameters in Table 5.1 are shown as solid lines of the same color.

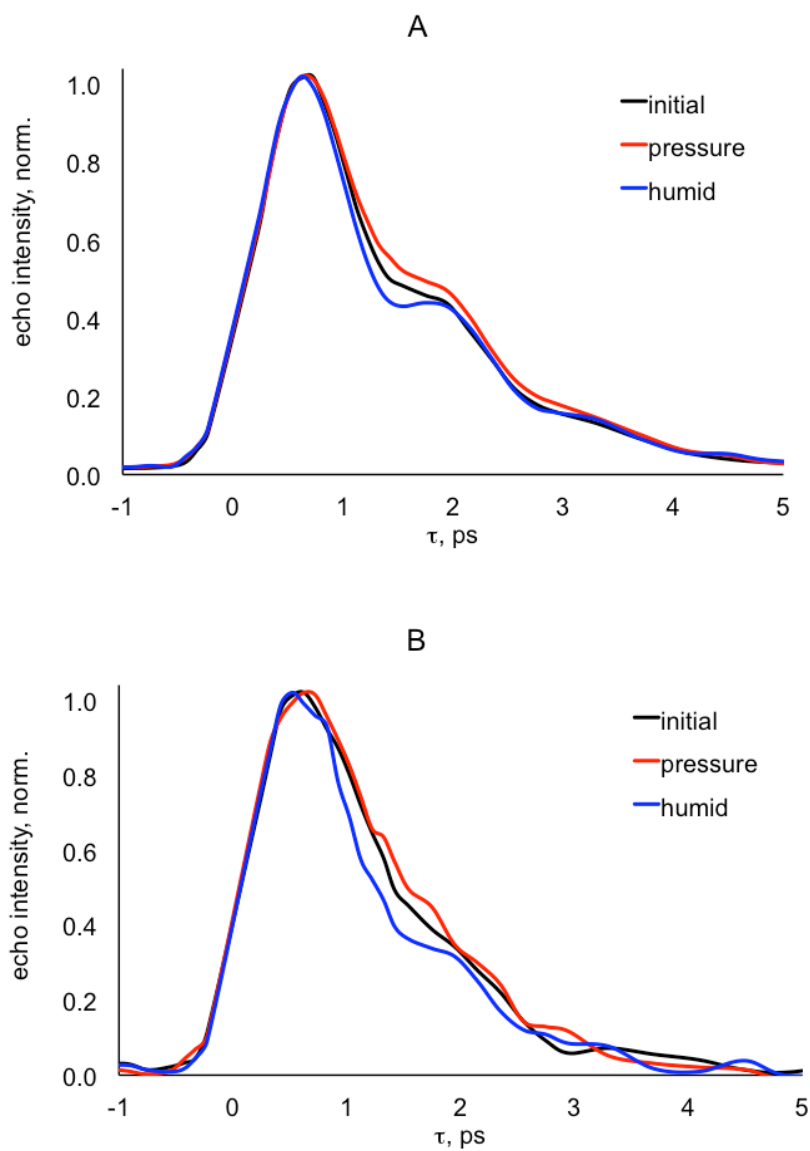


Figure 5.8: 2D-IR VES data at  $T_w = 0.5$  (A) and 7.5 ps (B) from control studies showing vibrational echo decays for samples treated with ambient air (labeled pressure) and humid then dry air (labeled humid).

work, the presence of slow structural motions ( $> 100$  ps) is expected as the molecules in these films have much less freedom to move than solution phase systems. Such dynamics are usually manifest in a more inhomogeneously broadened FTIR lineshape. However, the FTIR linewidths in Figure 5.3C show slight decreases during the dedoping-redoping cycle, which is not consistent with the increasing peak shifts in Figure 5.7A. Therefore, it is unlikely that the increased peak shift during the dedoping-redoping cycle is due to an increase in the unsampled slow structural dynamics. An alternate explanation for the increased peak-shift is a redistribution of the dynamics towards exceptionally fast time scales. When the product of the magnitude of these frequency perturbations ( $\Delta_i$ , in units of rad/ps) with their corresponding time scale ( $\tau_i$ , in units of ps) is much less than unity ( $\Delta_i * \tau_i \ll 1$ ), the dynamics are motionally narrowed and their impacts on the vibrational echo decays are minimized.<sup>190,191</sup> As a result, very fast ( $\tau_i$  is small) or very small amplitude ( $\Delta_i$  is small) frequency fluctuations in the metal-bound CO have diminishing contributions to the vibrational echo decays. If some of the dynamics that were present in the as-cast PANI-ES sample were to be converted to motionally narrowed dynamics in the recovered PANI-ES sample, then the vibrational echo decays would indeed become slower and the peak shifts would increase. As shown in section 5.4.5, fitting the 2D-IR VES data reveals that this is the case for these PANI films.

To access longer time scale dynamics (up to tens of ps), the  $T_w$  period is increased, thereby allowing the coherent collection of oscillators a longer window during which spectral diffusion can occur. The decreased dephasing over the dedoping-redoping cycle that is observed in the  $T_w = 0.5$  ps data is preserved in the echo decays at

$T_w = 10$  ps (Figure 5.7B), although each trace decays more quickly than it did at  $T_w = 0.5$  ps. The increased decay rates with  $T_w$  for all three samples demonstrate that spectral diffusion is occurring on the time scale of tens of ps as the result of slower structural motions. As these slower dynamics participate in the dephasing processes that produce the echo decay, a shifting of the echo peak towards the origin is expected. In the limit that all dynamics that perturb the CO oscillator frequencies have been sampled during a  $T_w$  period, the peak shift will be zero. Figure 5.9 shows the vibrational echo peak shifts as a function of  $T_w$  extracted from the decays collected at the center FTIR frequencies for the three PANI samples in this work. Here it is apparent that the early  $T_w$  peak shifts for the as-cast PANI-ES and  $\text{NH}_3$ -dedoped PANI-EB are significantly smaller than the recovered PANI-ES. It is clear that all three samples undergo spectral diffusion leading to peak shifts with  $T_w$  as the result of structural dynamics that perturb the CO frequencies on the time scale of tens of ps. The slowest spectral diffusion is found in the as-cast PANI-ES film (black markers). Dedoping these samples with  $\text{NH}_3$  leads to a noticeable increase in the peak shift by  $T_w = 10$  ps despite starting at similar peak shifts at early  $T_w$ s. It is interesting to note that the change in the peak shift over 10 ps is more similar between the  $\text{NH}_3$ -dedoped PANI-EB and the recovered PANI-ES. This implies that some characteristics of the dynamics on these longer time scales for these two samples are similar. This is surprising since the steady-state spectroscopy in Figures 5.2 and 5.3 shows that the as-cast and recovered PANI-ES spectra are more similar to each other than to the PANI-EB spectra. Thus, it is possible that the monotonic changes that have been tentatively associated with interchain structures are also connected to the dynamical changes that lead to spectral diffusion in these samples.

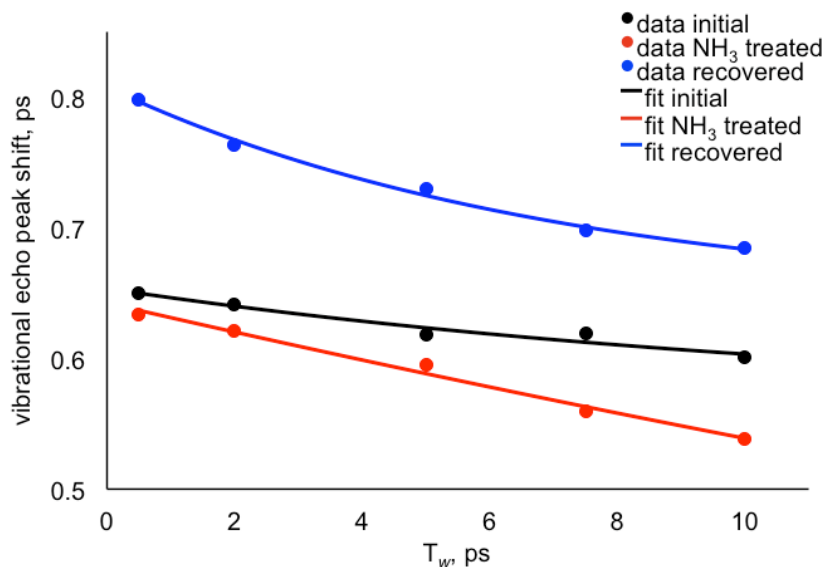


Figure 5.9: Vibrational echo peak shifts extracted from the vibrational echo decays for as-cast PANI-ES (black), NH<sub>3</sub>-dedoped PANI-EB, and recovered PANI-ES measured at 1925, 1933, and 1940 cm<sup>-1</sup>, respectively. The solid lines are single exponential fits to the data and are provided as an aid to the eye.

#### 5.4.4. Transient Grating Measurements

In order to quantify the vibrational dephasing processes measured in Figures 5.7 and 5.9, it was necessary to measure the impact of the dedoping-redoping cycle on vibrational energy relaxation (VER), which also contributes to the decay of the vibrational echo signals. Spectrally resolved transient grating measurements were performed on each of the three samples (Figure 5.10) at their center FTIR frequencies to measure the vibrational lifetimes ( $T_1$ ) of the ruthenium-bound CO.<sup>113,146,172</sup> The transient grating decay of the CO vibration in the as-cast PANI-ES film (black markers) is faster than the decay of the NH<sub>3</sub> treated film (red markers), while the recovered PANI-ES film (blue markers) is intermediate. The solid lines overlaid with these decays are single exponential fits to the data to determine the  $T_1$  values (time constants are multiplied by a factor of two in Table 5.1 due to the homodyne nature of the

transient grating measurement). The measured  $T_1$  values for the CO vibrations in the as-cast PANI-ES,  $\text{NH}_3$ -dedoped PANI-EB, and recovered PANI-ES were 9.0, 15.8, and 14.6 ps, respectively.

The VER of high frequency vibrations is facilitated by the excitation of lower energy vibrations and some number of low frequency phonon modes ( $< 200 \text{ cm}^{-1}$ ) in the matrix of PANI, CSA, and RuOEP.<sup>244,245</sup> For polyatomic liquids and organic solids, this process has been shown to depend upon parameters strongly related to the sample density. Since it is likely that the dedoping and redoping steps result in changes in the PANI film density, it is not surprising that the VER changes during the PANI cycling.<sup>246,247</sup> Based on the increases in PANI film crystallinity that have been reported upon protonation cycling, it is expected that the recovered PANI-ES film is more dense and has a greater degree of ordering.<sup>226</sup> It is likely that some of the morphological changes that occur in the PANI films upon dedoping with  $\text{NH}_3$  gas decrease the efficiency with which vibrational energy is coupled out of the ruthenium-bound CO. This change is partially reversed but persists to a large extent in the vicinity of the CO after the sample has been returned to the PANI-ES form. The behavior of the  $T_1$  is similar to the spectral diffusion in Figure 5.9, where the recovered film more closely resembles the  $\text{NH}_3$  treated film and not the initial PANI-ES film, despite their different chemical structures. It should also be noted that the  $T_1$  for the recovered PANI-ES sample is still somewhat faster than the PANI-EB, and therefore the progressive decrease in the vibrational echo decay times in Figure 5.7 must be due to differences in dephasing dynamics rather than VER.



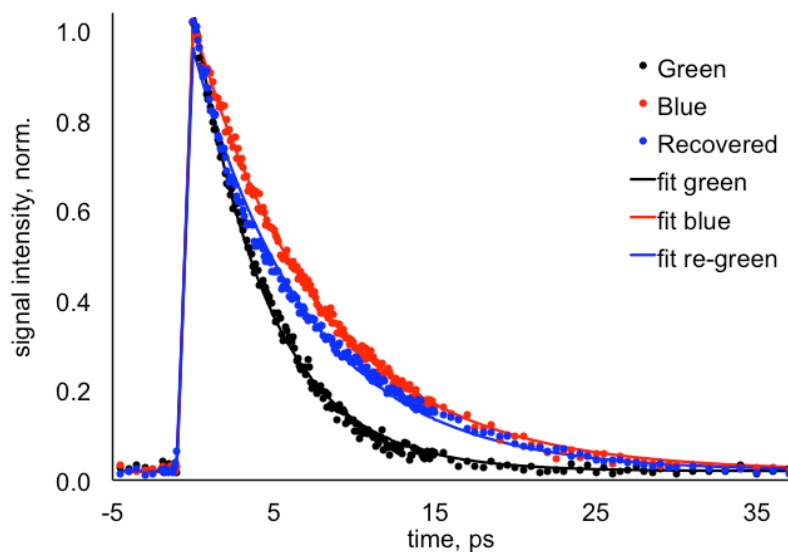


Figure 5.10. Normalized transient grating decays for the CO vibration in as-cast PANI-ES,  $\text{NH}_3$ -dedoped PANI-ES, and recovered PANI-ES measured at the center FTIR frequencies of 1925, 1933, and 1940  $\text{cm}^{-1}$ , respectively. The data are shown as markers and the overlaid solid lines are single exponential (convolved with a Gaussian pulse) fits to the data. The time constants of these fits are found in Table 5.1 multiplied by a factor of two.

#### 5.4.5. Description of FFCF parameters

A bi-exponential (plus a constant offset) form of the FFCF was used for the major transition of all three samples (as-cast = 1924.5  $\text{cm}^{-1}$ ,  $\text{NH}_3$ -dedoped = 1935.2  $\text{cm}^{-1}$ , recovered = 1939.1  $\text{cm}^{-1}$ ). An additional inhomogeneous broadening  $\Delta_0$  term was used for the FFCF of the minor transition of the initial sample (1905.2  $\text{cm}^{-1}$ ), and an additional single exponential was used for the FFCF of the minor transition of the  $\text{NH}_3$  treated sample (1921.9  $\text{cm}^{-1}$ ). The constant offset in each FFCF,  $\Delta_0$ , contains the static and slow molecular dynamics that contribute to inhomogeneous broadening. Over the course of the dedoping-redoping cycle, the  $\Delta_0$  terms decrease for all three samples. This suggests that a more homogeneous solvation environment has developed around the CO modes during the treatment cycle, which agrees with the slight decrease in the FTIR

linewidths for the CO in Figure 5.3C.

The fastest dynamic components for each of the three samples have identical amplitudes ( $\Delta_{1, tr.1}$ ) within the uncertainties of the fits (*tr.1* indicates transition 1). The exponential time constants ( $\tau_{1, tr.1}$ ) become progressively faster with values of 500, 240, and 200 fs for the as-cast PANI-ES, NH<sub>3</sub>-dedoped PANI-EB, and recovered PANI-ES samples, respectively. These parameters are shown in red in Table 5.1 for each FFCF. Although the low frequency dynamics that occur on these time scales are heavily overdamped and are not local vibrational modes in the usual sense, one can still say that the frequencies of motion that correspond to these time scales are 67, 139, and 167 cm<sup>-1</sup>. If the molecular origin of these dynamics were the same, this would imply that there is a general shifting of these dynamics to higher frequencies during the dedoping-redoping cycle. While there are assumptions involved in this interpretation that cannot be fully tested by the experiments presented here, a general increase in material density that would produce a shift of the instantaneous normal modes to higher frequencies is consistent with x-ray scattering studies of PANI films before and after protonation cycling.<sup>209,224,226</sup> Taking the product of  $\Delta_{1, tr.1}$  and  $\tau_{1, tr.1}$  yields 0.27, 0.15, and 0.10 for the PANI sequence, showing that this dynamic component also becomes motionally narrowed as the sample is cycled. As hypothesized above, this is the likely explanation for the progressive slowing of the vibrational echo decays in Figure 5.7 from the as-cast PANI-ES to the recovered PANI-ES. It can be concluded that the molecular dynamics that are perturbing the CO frequency on this time scale appear to become faster upon dedoping with NH<sub>3</sub>, and then further evolve in a unidirectional manner towards the motionally narrowed limit.

Table 5.1: FFCF parameters used to fit 2D-IR VES data.

FFCF parameters	as-cast PANI-ES		NH <sub>3</sub> -dedoped PANI-EB		recovered PANI-ES
	<i>transition 1</i>	<i>transition 2</i>	<i>transition 1</i>	<i>transition 2</i>	<i>transition 1</i>
center frequency (cm <sup>-1</sup> )	1924.5	1905.2	1935.2	1921.9	1939.1
relative concentration	1	0.14	1	0.22	1
anharmonicity (cm <sup>-1</sup> )	25	25	25.3	25.3	25
vibrational lifetime (ps)	9	9	15.8	15.8	14.6
$\Delta_0$ (cm <sup>-1</sup> )	9.2 (+0.2/-0.2) <sup>a</sup>	9.3 (+1.4/-1.2)	8.3 (+0.2/-0.1)	---	7.0 (+0.5/-0.3)
$\Delta_1$ (cm <sup>-1</sup> )	2.9 (+0.3/-0.3)	---	3.4 (+0.9/-0.3)	8.4 (+0.5/-0.4)	2.5 (+1.5/-0.5)
$\tau_1$ (ps)	0.5 (+0.2/-0.1)	---	0.24 (+0.08/-0.09)	2.6 (+2.4/-0.5)	0.2 (+0.1/-0.2)
$\Delta_2$ (cm <sup>-1</sup> )	2.7 (+0.5/-0.5)	---	2.2 (+0.3/-0.3)	---	2.5 (+0.6/-1.1)
$\tau_2$ (ps)	27 (+1/-13)	---	26 (+8/-10)	---	34 (+30/-26)

a. Values in parenthesis demonstrate positive and negative uncertainties as defined in the text.

In contrast to the trends observed in the higher frequency dynamics, the slowest exponential dynamic components (blue text in Table 5.1) in each sample are effectively unchanged by the dedoping-redoping cycle. Again, the  $\Delta_{2, tr.1}$  values are the same within the fit uncertainties, but the  $\tau_{2, tr.1}$  terms are also found to be identical having values between 26 and 34 ps. The uncertainties are admittedly larger than the shorter time scale exponentials due to the fact that the data were only collected out to  $T_w = 10$  ps (limited by the vibrational lifetime of the CO in these samples). Nonetheless, the best fit parameters do not exhibit any dramatic changes on these time scales of tens of ps regardless of the protonation state of the polymer. On the other hand, fitting the  $\text{NH}_3$ -dedoped PANI-EB data required a third exponential component (green text in Table 5.1) that has significant amplitude and a  $\tau_{1, tr.2}$  of 2.6 ps. Neither the as-cast nor the recovered PANI-ES sample required a dynamical term with this time constant, demonstrating that the structural dynamics that generate CO dephasing on this time scale are fundamentally unique to the EB form of PANI. Furthermore, these dynamics are reversible, appearing with the  $\text{NH}_3$ -dedoping treatment and vanishing from the FFCFs after recovery to the PANI-ES.

It is interesting to note, the similarities and differences between the dynamics that were observed in Chapter 4 and Chapter 5. For the initial PANI-ES in this chapter and the comparable PANI-ES that was doped with CSA in Chapter 4, the center frequencies of the transitions used to fit the linear lineshape are not the same. This observation is most likely a result of the additional procedure that was used in this chapter to ensure that the  $\text{NH}_3$  did not bind to the 6<sup>th</sup> coordination site of the RuOEP. Here, pyridine was bound to the free site of the ruthenium prior to use in the PANI films, an action that

could result in a static shift of the vibrational center of the CO mode. The incorporation of pyridine does not, however, appear to have resulted in strikingly different dynamics between the two PANI-ES films. In Chapter 4, the dynamics of the PANI-ES doped with CSA were characterized by 0.5 and 27 ps time components, which are similar to the time components observed for the initial PANI-ES in this chapter (1.2 and 41 ps).

In contrast, the time scales of the dynamics of the two PANI-EB samples are less similar. The PANI-EB sample in Chapter 4 was characterized by 0.3 and 229 ps time components, while the dedoped PANI-EB in Chapter 5 was characterized by 0.24, 2.6 and 26 ps time components. The dynamics of the two samples are alike in that the fastest time components (0.3 and 0.24 ps) are on the same order of magnitude and the longest time components (26 and 229 ps) are not well defined. However, the dynamics are different in that the dedoped PANI-EB required an additional 2.6 ps component. This difference can perhaps be explained by the molecular history of the samples. In Chapter 4, the PANI-EB sample was cast directly from NMP, while in Chapter 5 the PANI-EB sample was obtained from a PANI-ES sample cast from chloroform and treated with ammonia gas. Having been cast directly in the emeraldine base form the polymer chains in the film in Chapter 4 would be disorganized as seen in Figure 4.8A. In the PANI-EB film in Chapter 5, the extent of disorganization would be less since polymer chains would originally start in an ordered configuration like that shown in Figure 4.8B. Upon exposure to ammonia this structure would relax, but due to thermodynamic considerations the extent of this relaxation would be minimal. Thus, the dedoped PANI-EB films would consist of more ordered polymer structures than the PANI-EB film in Chapter 4. This additional order, and also the presence of CSA

molecules, may therefore cause a restriction of the polymer chains resulting in the appearance of this additional timescale component in the FFCF.

#### **5.4.6. Characterization of Resistance Measurements during Treatment Cycle**

X-ray measurements have reported that the structural memory effects in PANI films during protonation cycling are only partially reversible.<sup>226</sup> Specifically, it is believed that the intrachain morphologies are recovered, whereas the process irreversibly changes the interchain structures. The steady-state and time resolved spectroscopic studies presented here reflect this mixture of partially reversible and monotonically altered features. It is an ongoing goal of the field of organic electronics to determine which observables are correlated with enhancements in electrical performance. Thus, in order to correlate some of the static and dynamic structural trends for these samples with their electrical characteristics, two-point probe resistance measurements were performed on numerous samples processed through the same dedoping-redoping cycle. The resistances are shown on a logarithmic scale in Figure 5.11. The average resistance of the as-cast PANI-EB films was 500 k $\Omega$ . As expected, dedoping with NH<sub>3</sub> resulted in a large increase in the average sample resistance to 400 M $\Omega$  (nearly three orders of magnitude). Upon recovering the PANI-ES form, the resistances were consistently higher than for the as-cast samples, which is also consistent with the incompletely recovered intensity of the delocalized polaron absorption in Figure 5.3A. It is true that the error bars of these measurements overlap, however, the uncertainty on the recovered PANI-ES resistances is due to the spread in the as-cast PANI-ES resistances; the samples with somewhat higher starting resistances generally ended with higher resistances. Based on these data, the sample conductivities

can be characterized as being partially reversible over the dedoping-redoping cycle, rather than evolving in a monotonic manner.

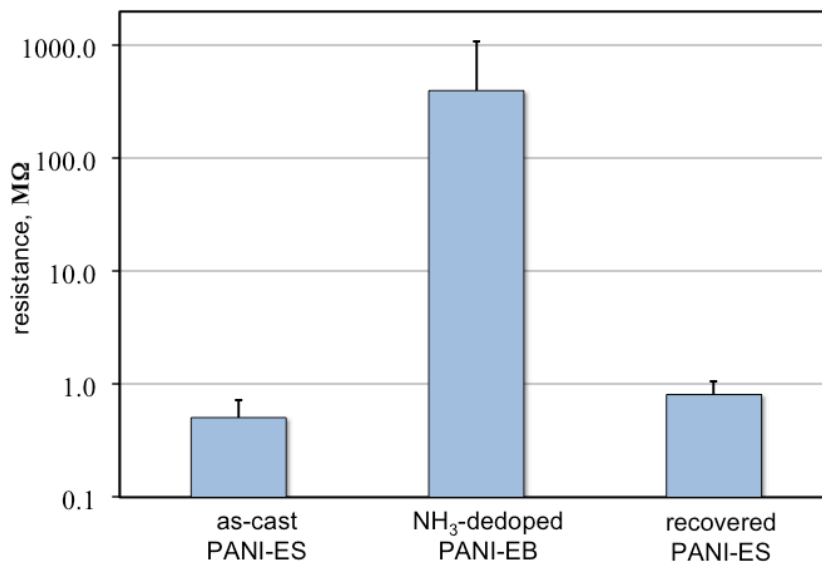


Figure 5.11. Two-point probe sample resistances measured for as-cast PANI-ES, NH<sub>3</sub>-dedoped PANI-EB, and recovered PANI-ES.

#### 5.4.7. Collective Interpretation of Results

Although the microscopic origins of the vibrational dephasing in the 2D-IR VES studies cannot be conclusively determined by this technique alone, there are clear correlations between the evolution of the FFCFs, the steady-state spectroscopy, and the PANI conductivities over the dedoping-redoping cycle. One interpretation of these correlations is that the features that evolve in the same manner should have similar molecular bases. Throughout this work, the measured quantities have been categorized as either partially reversible or monotonically varying, and it has been noted that these characteristics are likely related to intra- and interchain morphologies, respectively.<sup>226</sup> Under this interpretation, the observables that are partially reversible (i.e. the delocalized polaron absorption, ultrafast dynamics on the time scale of a few ps, and

film resistances) may be closely related to intrachain static and dynamic structures. Likewise, those that vary unidirectionally (i.e. the localized polaron absorption and ultrafast dynamics on the time scale of hundreds of fs) may be most closely associated with interchain static and dynamic structures.

## 5.5. Conclusions

The results of this study demonstrate that the static morphologies reported by UV-visible and FTIR spectroscopies are notably different for as-cast PANI-ES,  $\text{NH}_3$ -dedoped PANI-EB, and recovered PANI-ES thin films. Despite the expected similarities in chemical structures of the beginning and ending states in this cycle, only some of the spectral features are partially reversed while others appear to change monotonically towards new molecular configurations. Upon completing the dedoping-redoping cycle, we find that the PANI films retain some memory of the post-processing history in their static structure. This is consistent with the body of knowledge about PANI that has been accumulated from x-ray scattering studies. The 2D-IR VES measurements provide new information by demonstrating that there are also changes that occur in the structural dynamics in these films that are reversible and others that persist even after the polymer has been returned to its original protonation state.

There are intriguing parallels that can be drawn between the behavior of the film resistances, the ultrafast dynamics in this study, and the theoretical predictions of the role of structural motions in charge conduction. Theoretical work by Troisi and Orlandi predicted that low frequency vibrations at 1.1 THz ( $37 \text{ cm}^{-1}$ ) should be particularly detrimental to carrier mobilities.<sup>83</sup> This has been corroborated to some extent by experimental measurements by Laarhoven and coworkers, who reported that structural



motions in pentacene thin films in this frequency regime were highly correlated to charge carrier mobilities.<sup>35,83</sup> It is potentially significant that the dynamics revealed by the FFCFs in Table 5.1 that most closely track the behavior of the film resistances are those that occur in the time regime of a few ps, as predicted by theory. Yet, the resistances in the PANI films were not fully recovered after the dedoping-redoping cycle, suggesting that the fastest dynamics (hundreds of fs), which varied monotonically, may also play a role in the final carrier mobilities. Based on these results, it is possible that developing approaches to tune the structural dynamics on these fast time scales may provide new avenues to improve the carrier mobilities in amorphous organic thin films.<sup>d</sup>

---

<sup>d</sup> The authors gratefully acknowledge funding from the National Science Foundation under CHE-0847356. The authors thank Prof. Ken Leopold for providing the NH<sub>3</sub> (g) for the dedoping procedures.

## Bibliography

- [1] Anthony, J. E.; Brooks, J. S.; Eaton, D. L.; Parkin, S. R. *J. Am. Chem. Soc.* 2001, *123*, 9482.
- [2] Bendikov, M.; Wudl, F.; Perepichka, D. F. *Chemical Reviews* 2004, *104*, 4891.
- [3] Curtis, M. D.; Cao, J.; Kampf, J. W. *Journal of the American Chemical Society* 2004, *126*, 4318.
- [4] Huang, W. S.; Humphrey, B. D.; Macdiarmid, A. G. *Journal of the Chemical Society-Faraday Transactions I* 1986, *82*, 2385.
- [5] Macdiarmid, A. G.; Chiang, J. C.; Halpern, M.; Huang, W. S.; Mu, S. L.; Somasiri, N. L. D.; Wu, W. Q.; Yaniger, S. I. *Molecular Crystals and Liquid Crystals* 1985, *121*, 173.
- [6] Macinnes, D.; Druy, M. A.; Nigrey, P. J.; Nairns, D. P.; MacDiarmid, A. G.; Heeger, A. J. *J. Chem. Soc.-Chem. Comm.* 1981, 317.
- [7] Wang, R. S.; Wang, L. M.; Fu, Y. J.; Su, Z. M. *Synth. Met.* 1995, *69*, 713.
- [8] Sirringhaus, H. *Advanced Materials* 2005, *17*, 2411.
- [9] Rui Zhang, B. L., Mihaeka C. Ivou, Malika Jefferies-EL, Genevieve Sauve, Jessica Cooper, Shijun Jia, Stephanie Tristram-Nagle, Detlef M. Smilgies, David N. Lambeth, Richard D. McCullough, Tomasz Kowaleski. *Journal of the American Chemical Society* 2006, *128*, 3480.
- [10] Verma, D.; Dutta, V. *Sensors and Actuators B-Chemical* 2008, *134*, 373.
- [11] Kukla, A. L.; Shirshov, Y. M.; Piletsky, S. A. *Sensors and Actuators B-Chemical* 1996, *37*, 135.
- [12] Dominique Nicolas-Debarnot, F. P.-E. *Analytica Chimica Acta* 2003, *475*, 1.
- [13] Yim, K.; Zheng, Z.; Friend, R. H.; Huck, T. S. W.; Kim, J. *Adv. Funct. Mater.* 2008, *18*, 2897.
- [14] Ma, B.; Kim, J. B.; Deng, L.; Poulsen, D. A.; Thompson, M. E.; Frechet, J. M. *J. Macromolecules* 2007, *40*, 8156.
- [15] Takahashi, K.; Takano, Y.; Yamaguchi, T.; Nakamura, J.; Yokoe, C.; Murata, K. *Synthetic Metals* 2005, *155*, 51.
- [16] Thompson, B. C.; Frechet, J. M. J. *Angewandte Chemie-International Edition* 2008, *47*, 58.
- [17] Ayzner, A. L.; Wanger, D. D.; Tassone, C. J.; Tolbert, S. H.; Schwartz, B. J. *Journal of Physical Chemistry C* 2008, *112*, 18711.
- [18] Campoy-Quiles, M.; Ferenczi, T.; Agostinelli, T.; Etchegoin, P. G.; Kim, Y.; Anthopoulos, T. D.; Stavrinou, P. N.; Bradley, D. D. C.; Nelson, J. *Nature Materials* 2008, *7*, 158.
- [19] Forrest, S. R. *Nature* 2004, *428*, 911.
- [20] Darling, S. B. *Journal of Physical Chemistry B* 2008, *112*, 8891.
- [21] Heeger, A. J. *Angewandte Chemie-International Edition* 2001, *40*, 2591.
- [22] Bredas, J. L.; Beljonne, D.; Coropceanu, V.; Cornil, J. *Chemical Reviews* 2004, *104*, 4971.
- [23] McCulloch, I.; Heeney, M.; Bailey, C.; Genevicius, K.; Macdonald, I.; Shkunov, M.; Sparrowe, D.; Tierney, S.; Wagner, R.; Zhang, W. M.;

- Chabynyc, M. L.; Kline, R. J.; McGehee, M. D.; Toney, M. F. *Nature Materials* 2006, 5, 328.
- [24] Cheung, D. L.; McMahon, D. P.; Troisi, A. *Journal of the American Chemical Society* 2009, 131, 11179.
- [25] Della Valle, R. G.; Venuti, E.; Farina, L.; Brillante, A.; Masino, M.; Girlando, A. *Journal of Physical Chemistry B* 2004, 108, 1822.
- [26] Hutchison, G. R.; Ratner, M. A.; Marks, T. J. *J. Am. Chem. Soc.* 2005, 127, 2339.
- [27] Troisi, A.; Orlandi, G.; Anthony, J. E. *Chemistry of Materials* 2005, 17, 5024.
- [28] Troisi, A.; Orlandi, G. *Journal of Physical Chemistry B* 2005, 109, 1849.
- [29] Vukmirovic, N.; Wang, L. W. *Nano Letters* 2009, 9, 3996.
- [30] Vukmirovic, N.; Wang, L. W. *Journal of Physical Chemistry B* 2009, 113, 409.
- [31] Fratini, S.; Ciuchi, S. *Physical Review Letters* 2009, 103.
- [32] Eigner, A. A.; Anglin, T. C.; Massari, A. M. *Journal of Physical Chemistry C* 2010, 114, 12308.
- [33] Eigner, A. A.; Jones, B. H.; Koprucki, B. W.; Massari, A. M. *Journal of Physical Chemistry B* 2011, *in press*.
- [34] Eigner, A. A.; Jones, B. H.; Koprucki, B. W.; Massari, A. M. *Journal of Physical Chemistry B* 2011, 115, 8686.
- [35] Laarhoven, H. A. V.; Flipse, C. F. J.; Koeberg, M.; Bonn, M.; Hendry, E.; Orlandi, G.; Jurchescu, O. D.; Palstra, T. T. M.; Troisi, A. *Journal of Chemical Physics* 2008, 129.
- [36] Xiao, D. Q.; Skourtis, S. S.; Rubtsov, I. V.; Beratan, D. N. *Nano Letters* 2009, 9, 1818.
- [37] Barbara, P. F.; Meyer, T. J.; Ratner, M. A. *J. Phys. Chem.* 1996, 100, 13148.
- [38] Park, S. M.; Lee, H. J. *Bulletin of the Chemical Society of Korea* 2005, 26, 697.
- [39] Rector, K. D.; Fayer, M. D. *Ultrafast Infrared and Raman Spectroscopy*; Marcel Dekker, Inc.: New York, 2001; Vol. 26.
- [40] Fayer, M. D. *Ann. Rev. Phys. Chem.* 2001, 52, 315.
- [41] Zheng, J.; Kwak, K.; Fayer, M. D. *Accounts of Chemical Research* 2007, 40, 75.
- [42] Khalil, M.; Demirdoven, N.; Tokmakoff, A. *Journal of Physical Chemistry A* 2003, 107, 5258.
- [43] Elsaesser, T. *Accounts of Chemical Research* 2009, 42, 1220.
- [44] Mukherjee, P.; Kass, I.; Arkin, I.; Zanni, M. T. *Proceedings of the National Academy of Sciences of the United States of America* 2006, 103, 3528.
- [45] Park, J.; Ha, J. H.; Hochstrasser, R. M. *Journal of Chemical Physics* 2004, 121, 7281.
- [46] Asbury, J. B.; Steinel, T.; Stromberg, C.; Corcelli, S. A.; Lawrence, C. P.; Skinner, J. L.; Fayer, M. D. *Journal of Physical Chemistry A* 2004, 108, 1107.
- [47] Woutersen, S.; Mu, Y.; Stock, G.; Hamm, P. *Chemical Physics* 2001, 266, 137.
- [48] Baiz, C. R.; McRobbie, P. L.; Anna, J. M.; Geva, E.; Kubarych, K. J. *Accounts of Chemical Research* 2009, 42, 1395.

- [49] Massari, A. M.; McClain, B. L.; Finkelstein, I. J.; Lee, A. P.; Reynolds, H. L.; Bren, K. L.; Fayer, M. D. *J. Phys. Chem. B* 2006, *110*, 18803.
- [50] Sando, G. M.; Dahl, K.; Owrutsky, J. C. *Journal of Physical Chemistry A* 2004, *108*, 11209.
- [51] King, J. T.; Baiz, C. R.; Kubarych, K. J. *Journal of Physical Chemistry A* 2010, *114*, 10590.
- [52] Finkelstein, I. J.; Massari, A. M.; Fayer, M. D. *Biophysical Journal* 2007, *92*, 3652.
- [53] Xu, Q. H.; Fayer, M. D. *Laser Physics* 2002, *12*, 1104.
- [54] Rector, K. D.; Jiang, J. W.; Berg, M. A.; Fayer, M. D. *Journal of Physical Chemistry B* 2001, *105*, 1081.
- [55] Vehoff, T.; Baumeier, B.; Troisi, A.; Andrienko, D. *Journal of the American Chemical Society* 2010, *132*, 11702.
- [56] Coropceanu, V.; Cornil, J.; da Silva, D. A.; Olivier, Y.; Silbey, R.; Bredas, J. L. *Chemical Reviews* 2007, *107*, 926.
- [57] Sirringhaus, H.; Brown, P. J.; Friend, R. H.; Nielsen, M. M.; Bechgaard, K.; Langeveld-Voss, B. M. W.; Spiering, A. J. H.; Janssen, R. A. J.; Meijer, E. W.; Herwig, P.; de Leeuw, D. M. *Nature* 1999, *401*, 685.
- [58] Fritz, S. E.; Martin, S. M.; Frisbie, C. D.; Ward, M. D.; Toney, M. F. *Journal of the American Chemical Society* 2004, *126*, 4084.
- [59] Horowitz, G. *Adv. Mater.* 1998, *10*, 365.
- [60] Zeis, R.; Besnard, C.; Siegrist, T.; Schlockermann, C.; Chi, X. L.; Kloc, C. *Chem. Mater.* 2006, *18*, 244.
- [61] Karl, N.; Kraft, K. H.; Marktanner, J.; Munch, M.; Schatz, F.; Stehle, R.; Uhde, H. M. *J. Vac. Sci. Technol. A* 1999, *17*, 2318.
- [62] Pasveer, W. F.; Cottaar, J.; Tanase, C.; Coehoorn, R.; Bobbert, P.; Blom, P. W. M. *Phys. Rev. Lett.* 2005, *94*, 206601.
- [63] Kline, R. J.; McGehee, M. D.; Toney, M. F. *Nature Materials* 2006, *5*, 222.
- [64] Osterbacka, R.; An, C. P.; Jiang, X. M.; Vardeny, Z. V. *Science* 2000, *287*, 839.
- [65] Bao, Z.; Dodabalapur, A.; Lovinger, A. J. *Appl. Phys. Lett.* 1996, *69*, 4108.
- [66] Cheung, D. L.; McMahan, D. P.; Troisi, A. *Journal of Physical Chemistry B* 2009, *113*, 9393.
- [67] Kline, R. J.; McGehee, M. D.; Kadnikova, E. N.; Liu, J.; Frechet, J. M. J. *Advanced Materials* 2003, *15*, 1519.
- [68] Kline, R. J.; McGehee, M. D.; Kadnikova, E. N.; Liu, J.; Frechet, J. M. J.; Toney, M. F. *Macromolecules* 2005, *38*, 3312.
- [69] Mozer, A. J.; Denk, P.; Scharber, M. C.; Neugebauer, H.; Sariciftci, N. S. *Journal of Physical Chemistry B* 2004, *108*, 5235.
- [70] Warta, W.; Karl, N. *Phys. Rev. B* 1985, *32*, 1172.
- [71] Zen, A.; Pflaum, J.; Hirschmann, S.; Zhuang, W.; Jaiser, F.; Asawapirom, U.; Rabe, J. P.; Scherf, U.; Neher, D. *Adv. Funct. Mater.* 2004, *14*, 757.
- [72] Jurchescu, O. D.; Bass, J.; Palstra, T. T. M. *Appl. Phys. Lett.* 2004, *84*, 3061.
- [73] Liu, C. Y.; Bard, A. J. *Nature* 2002, *418*, 162.

- [74] Chandrasekhar, M.; Guha, S.; Graupner, W. *Advanced Materials* 2001, *13*, 613.
- [75] Rang, Z.; Haraldsson, A.; Kim, D. M.; Ruden, P. P.; Nathan, M. I.; Chesterfield, R. J.; Frisbie, C. D. *Appl. Phys. Lett.* 2001, 2731.
- [76] Munn, R. W.; Silbey, R. *Journal of Chemical Physics* 1985, *83*, 1854.
- [77] Munn, R. W.; Silbey, R. *Journal of Chemical Physics* 1985, *83*, 1843.
- [78] Holstein, T. *Annals of Physics* 1959, *8*, 343.
- [79] Holstein, T. *Annals of Physics* 1959, *8*, 325.
- [80] Friedman, L. *Phys. Rev. A* 1964, *135*, A233.
- [81] Emin, D. *Adv. Phys.* 1975, *24*, 305.
- [82] Silbey, R.; Munn, R. W. *J. Chem. Phys.* 1980, *72*, 2763.
- [83] Troisi, A.; Orlandi, G. *Journal of Physical Chemistry A* 2006, *110*, 4065.
- [84] Pedron, D.; Speghini, A.; Mulloni, V.; Bozio, R. *Journal of Chemical Physics* 1995, *103*, 2795.
- [85] Binstead, R. A.; Reimers, J. R.; Hush, N. S. *Chemical Physics Letters* 2003, *378*, 654.
- [86] Coropceanu, V.; Andre, J. M.; Malagoli, M.; Bredas, J. L. *Theoretical Chemistry Accounts* 2003, *110*, 59.
- [87] Coropceanu, V.; Nakano, T.; Gruhn, N. E.; Kwon, O.; Yade, T.; Katsukawa, K.; Bredas, J. L. *Journal of Physical Chemistry B* 2006, *110*, 9482.
- [88] Loparo, J. J.; Roberts, S. T.; Tokmakoff, A. *Journal of Chemical Physics* 2006, *125*, 194521.
- [89] Loparo, J. J.; Roberts, S. T.; Tokmakoff, A. *Journal of Chemical Physics* 2006, *125*, 194522.
- [90] Cowan, M. L.; Bruner, B. D.; Huse, N.; Dwyer, J. R.; Chugh, B.; Nibbering, E. T. J.; Elsaesser, T.; Miller, J. R. *Nature* 2005, *434*, 199.
- [91] Fecko, C. J.; Loparo, J. J.; Roberts, S. T.; Tokmakoff, A. *Journal of Chemical Physics* 2005, *112*, 054506.
- [92] Roberts, S. T.; Ramasesha, K.; Tokmakoff, A. *Accounts of Chemical Research* 2009, *42*, 1239.
- [93] Steinel, T.; Asbury, J. B.; Corcelli, S. A.; Lawrence, C. P.; Skinner, J. L.; Fayer, M. D. *Chemical Physics Letters* 2004, *386*, 295.
- [94] Cringus, D.; Yeremenko, S.; Pshenichnikov, M. S.; Weirma, D. A. *Journal of Physical Chemistry B* 2004, *108*, 10376.
- [95] Tang, H.; Piletic, I. R.; Riter, R. E.; Levinger, N. E.; Fayer, M. D. *Physical Review Letters* 2005, *94*, 057405.
- [96] Piletic, I. R.; Tan, H. S.; Fayer, M. D. *Journal of Physical Chemistry B* 2005, *109*, 21273.
- [97] Rector, K. D.; Fayer, M. D. *International Reviews in Physical Chemistry* 1998, *17*, 261.
- [98] Asbury, J. B.; Steinel, T.; Fayer, M. D. *Chem. Phys. Lett.* 2003, *381*, 139.
- [99] Golonzka, O.; Khalil, M.; Demirdoven, N.; Tokmakoff, A. *Journal of Chemical Physics* 2001, *115*, 10814.
- [100] Rector, K. D.; Fayer, M. D. *J. Chem. Phys.* 1998, *108*, 1794.

- [101] Demirdoven, N.; Cheatum, C. M.; Chung, M.; Khalil, M.; Knoester, J.; Tokmakoff, A. *Journal of the American Chemical Society* 2004, *109*, 7511.
- [102] Zanni, M. T.; Hochstrasser, R. M. *Curr. Opin. Struct. Biol.* 2001, *11*, 516.
- [103] Finkelstein, I. J.; Goj, A.; McClain, B. L.; Massari, A. M.; Merchant, K. A.; Loring, R. F.; Fayer, M. D. *J. Phys. Chem. B* 2005, *109*, 16959.
- [104] Kim, Y. S.; Liu, L.; Axelsen, P. H.; Hochstrasser, R. M. *Proceedings of the National Academy of Sciences of the United States of America* 2008, *105*, 7720.
- [105] Massari, A. M.; Finkelstein, I. J.; McClain, B. L.; Goj, A.; Wen, X.; Bren, K. L.; Loring, R. F.; Fayer, M. D. *J. Am. Chem. Soc.* 2005, *127*, 14279.
- [106] Mukherjee, P.; Kass, I.; Arkin, I.; Zanni, M. T. *J. Phys. Chem. B* 2006, *110*, 24740.
- [107] Zheng, J.; Kwak, K.; Chen, X.; Asbury, J. B.; Fayer, M. D. *Journal of the American Chemical Society* 2006, *128*, 2977.
- [108] Thompson, D. E.; Merchant, K. A.; Fayer, M. D. *J. Chem. Phys.* 2001, *115*, 317.
- [109] Roberts, S. T.; Ramasesha, K.; Petersen, P. B.; Mandal, A.; Tokmakoff, A. *J. Phys. Chem. A* 2011, *115*, 3957.
- [110] Fayer, M. D. *Annual Review of Physical Chemistry* 2009, *60*, 21.
- [111] Chattopadhyay, A.; Boxer, S. G. *Journal of the American Chemical Society* 1994, *117*, 1449.
- [112] Finkelstein, I. J.; Zheng, J.; Ishikawa, H.; Kim, S.; Kwak, K.; Fayer, M. D. *Physical Chemistry Chemical Physics* 2007, *9*, 1533.
- [113] Salcedo, J. R.; Siegman, A. E.; Dlott, D. D.; Fayer, M. D. *Physical Review Letters* 1978, *41*, 131.
- [114] Mukamel, S. *Principles of Nonlinear Optical Spectroscopy*; Oxford University Press: New York, 1995.
- [115] Hamm, P.; Hochstrasser, R. M. Structure and dynamics of proteins and peptides: Femtosecond two-dimensional infrared spectroscopy. In *Ultrafast Infrared and Raman Spectroscopy*; Fayer, M. D., Ed.; Marcel Dekker, Inc.: New York, 2001; Vol. 26; pp 273.
- [116] Ruzette, A. V.; Leibler, L. *Nature Materials* 2005, *4*, 19.
- [117] Lodge, T. P.; Pudil, B.; Hanley, K. J. *Macromolecules* 2002, *35*, 4707.
- [118] Kato, T. *Science* 2002, *295*, 2414.
- [119] Bates, F. S. *Science* 1991, *251*, 898.
- [120] Keivanidis, P. E.; Howard, I. A.; Friend, R. H. *Advanced Functional Materials* 2008, *18*, 3189.
- [121] Schmidt-Mende, L.; Fechtenkotter, A.; Mullen, K.; Friend, R. H.; MacKenzie, J. D. *Physica E-Low-Dimensional Systems & Nanostructures* 2002, *14*, 263.
- [122] Schmidt-Mende, L.; Fechtenkotter, A.; Mullen, K.; Moons, E.; Friend, R. H.; MacKenzie, J. D. *Science* 2001, *293*, 1119.
- [123] Chirvase, D.; Parisi, J.; Hummelen, J. C.; Dyakonov, V. *Nanotechnology* 2004, *15*, 1317.

- [124] Gust, D.; Moore, T. A.; Moore, A. L. *Accounts of Chemical Research* 2001, 34, 40.
- [125] Wohrle, D.; Meissner, D. *Advanced Materials* 1991, 3, 129.
- [126] Campbell, W. M.; Jolley, K. W.; Wagner, P.; Wagner, K.; Walsh, P. J.; Gordon, K. C.; Schmidt-Mende, L.; Nazeeruddin, M. K.; Wang, Q.; Gratzel, M.; Officer, D. L. *Journal of Physical Chemistry C* 2007, 111, 11760.
- [127] Kay, A.; Gratzel, M. *Journal of Physical Chemistry* 1993, 97, 6272.
- [128] Belcher, W. J.; Wagner, K. I.; Dastoor, P. C. *Solar Energy Materials and Solar Cells* 2007, 91, 447.
- [129] Ohno, O.; Kaizu, Y.; Kobayashi, H. *Journal of Chemical Physics* 1993, 99, 4128.
- [130] Maiti, N. C.; Mazumdar, S.; Periasamy, N. *Journal of Physical Chemistry B* 1998, 102, 1528.
- [131] Brown, S. B.; Shillcock, M.; Jones, P. *Biochemical Journal* 1976, 153, 279.
- [132] Suydam, I. T.; Boxer, S. G. *Biochemistry* 2003, 42, 12050.
- [133] Zhao, Y.; Xie, Z. Y.; Qu, Y.; Geng, Y. H.; Wang, L. X. *Applied Physics Letters* 2007, 90, 043504.
- [134] Kwak, K.; Rosenfeld, D. E.; Fayer, M. D. *Journal of Chemical Physics* 2008, 128.
- [135] Kim, Y. S.; Hochstrasser, R. M. *Proceedings of the National Academy of Sciences of the United States of America* 2005, 102, 11185.
- [136] Kasha, M. *Radiation Research* 1963, 20, 55.
- [137] BOHN, P. W. ASPECTS OF STRUCTURE AND ENERGY-TRANSPORT IN ARTIFICIAL MOLECULAR ASSEMBLIES. In *Annu Rev Phys Chem*, 1993; Vol. 44; pp 37.
- [138] Hochstrasser, R. M.; Kasha, M. *Photochem. Photobiol.* 1964, 3, 317.
- [139] Shediach, R.; Gray, M. H. B.; Uyeda, H. T.; Johnson, R. C.; Hupp, J. T.; Angiolillo, P. J.; Therien, M. J. *Journal of the American Chemical Society* 2000, 122, 7017.
- [140] Kumble, R.; Palese, S.; Lin, V. S. Y.; Therien, M. J.; Hochstrasser, R. M. *Journal of the American Chemical Society* 1998, 120, 11489.
- [141] Holdcroft, S.; Xu, B. *Macromolecules* 1993, 26, 4457.
- [142] Barbara, P. F.; Adachi, T.; Traub, M. C.; Bolinger, J. C. *Science* 2011, 331, 565.
- [143] Purrello, R.; Bellacchico, E.; Gurrieri, S.; Lauceri, R.; Raudino, A.; Scolaro, L. M.; Santoro, A. M. *J. Phys. Chem. B* 1998, 102, 8852.
- [144] van Esch, J. H.; Feiters, M. C.; Peters, A. M.; Nolte, R. J. M. *Journal of Physical Chemistry* 1994, 98, 5541.
- [145] Choudhury, B.; Weedon, A. C.; Bolton, J. R. *Langmuir* 1998, 14, 6192.
- [146] Garrity, D. K.; Skinner, J. L. *Journal of Chemical Physics* 1985, 82, 260.
- [147] Abram, II; Hochstrasser, R. M.; Kohl, J. E.; Semack, M. G.; White, D. *Journal of Chemical Physics* 1979, 71, 153.
- [148] Burland, D. M.; Cooper, D. E.; Fayer, M. D.; Gochanour, C. R. *Chemical Physics Letters* 1977, 52, 279.

- [149] Liu, S. M.; Plecnik, C. E.; Shore, S. G. *Comptes Rendus Chimie* 2005, 8, 1827.
- [150] Vrtis, R. N.; Bott, S. G.; Lippard, S. J. *Organometallics* 1992, 11, 270.
- [151] Delacruz, C.; Sheppard, N. *Journal of Molecular Structure* 1990, 224, 141.
- [152] Osborne, J. H.; Rheingold, A. L.; Trogler, W. C. *Journal of the American Chemical Society* 1985, 107, 6292.
- [153] Chang, J. F.; Sun, B. Q.; Breiby, D. W.; Nielsen, M. M.; Solling, T. I.; Giles, M.; McCulloch, I.; Sirringhaus, H. *Chemistry of Materials* 2004, 16, 4772.
- [154] Savenije, T. J.; Kroeze, J. E.; Yang, X. N.; Loos, J. *Advanced Functional Materials* 2005, 15, 1260.
- [155] Fu, Y.; Lin, C.; Tsai, F. *Organic Electronics* 2009, 10, 883.
- [156] Miller, S.; Fanchini, G.; Lin, Y.; Li, C.; Chen, C.; Su, W.; Chhowalla, M. *J. Mater. Chem.* 2008, 18, 306.
- [157] Zhokhavets, U.; Erb, T.; Gobsch, G.; Al-Ibrahim, M.; Ambacher, O. *Chemical Physics Letters* 2006, 418, 347.
- [158] Li, G.; Yao, Y.; Yang, H.; Shrotriya, V.; Yang, G.; Yang, Y. *Advanced Functional Materials* 2007, 17, 1636.
- [159] Bredas, J. L.; Calbert, J. P.; da Silva, D. A.; Cornil, J. *Proc. Natl. Acad. Sci. USA* 2002, 99, 5804.
- [160] Hutchison, G. R.; Ratner, M. A.; Marks, T. J. *Journal of the American Chemical Society* 2005, 127, 16866.
- [161] Kwon, O.; Coropceanu, V.; Gruhn, N. E.; Durivage, J. C.; Laquindanum, J. G.; Katz, H. E.; Cornil, J.; Bredas, J. L. *Journal of Chemical Physics* 2004, 120, 8186.
- [162] Hamm, P.; Lim, M. H.; Hochstrasser, R. M. *Journal of Physical Chemistry B* 1998, 102, 6123.
- [163] Zimdars, D.; Tokmakoff, A.; Chen, S.; Greenfield, S. R.; Fayer, M. D.; Smith, T. I.; Schwettman, H. A. *Phys. Rev. Lett.* 1993, 70, 2718.
- [164] Massari, A. M.; Finkelstein, I. J.; Fayer, M. D. *J. Am. Chem. Soc.* 2006, 128, 3990.
- [165] Shim, S. H.; Strasfeld, D. B.; Ling, Y. L.; Zanni, M. T. *Proceedings of the National Academy of Sciences of the United States of America* 2007, 104, 14197.
- [166] Khalil, M.; Tokmakoff, A. *Chem. Phys.* 2001, 266, 213.
- [167] Eigner, A. A.; Konold, P. E.; Massari, A. M. *Journal of Physical Chemistry B* 2009, 113, 14549.
- [168] Grecu, S.; Roggenbuck, A.; Opitz, A.; Brutting, W. *Organic Electronics* 2006, 7, 276.
- [169] Zen, A.; Neher, D.; Silmy, K.; Hollander, A.; Asawapirom, U.; Scherf, U. *Japanese Journal of Applied Physics Part 1-Regular Papers Short Notes & Review Papers* 2005, 44, 3721.
- [170] Eckbreth, A. C. *Applied Physics Letters* 1978, 32, 421.
- [171] Asbury, J. B.; Steinel, T.; Stromberg, C.; Gaffney, K. J.; Piletic, I. R.; Goun, A.; Fayer, M. D. *Chem. Phys. Lett.* 2003, 374, 362.
- [172] Joo, T. H.; Jia, Y. W.; Yu, J. Y.; Lang, M. J.; Fleming, G. R. *Journal of Chemical Physics* 1996, 104, 6089.



- [173] Chung, H. S.; Tokmakoff, A. *J. Phys. Chem. B* 2006, *110*, 2888.
- [174] Shim, S. H.; Gupta, R.; Ling, Y. L.; Strasfeld, D. B.; Raleigh, D. P.; Zanni, M. T. *Proceedings of the National Academy of Sciences of the United States of America* 2009, *106*, 6614.
- [175] Asbury, J. B.; Steinel, T.; Fayer, M. D. *J. Phys. Chem. B* 2004, *108*, 6544.
- [176] Fayer, M. D.; Moilanen, D. E.; Wong, D.; Rosenfeld, D. E.; Fenn, E. E.; Park, S. *Accounts of Chemical Research* 2009, *42*, 1210.
- [177] Li, S. Z.; Schmidt, J. R.; Piryatinski, A.; Lawrence, C. P.; Skinner, J. L. *Journal of Physical Chemistry B* 2006, *110*, 18933.
- [178] Ohta, K.; Maekawa, H.; Saito, S.; Tominaga, K. *Journal of Physical Chemistry A* 2003, *107*, 5643.
- [179] Tokmakoff, A.; Fayer, M. D. *Accounts of Chemical Research* 1995, *28*, 437.
- [180] Berg, M. A.; Hubble, H. W. *Chemical Physics* 1998, *233*, 257.
- [181] Blum, G.; Mullins, S. R.; Keren, K.; Fonovic, M.; Jedeszko, C.; Rice, M. J.; Sloane, B. F.; Bogyo, M. *Nature Chemical Biology* 2005, *1*, 203.
- [182] Hennig, A.; Bakirci, H.; Nau, W. M. *Nature Methods* 2007, *4*, 629.
- [183] Chithrani, B. D.; Ghazani, A. A.; Chan, W. C. W. *Nano Letters* 2006, *6*, 662.
- [184] Mornet, S.; Vasseur, S.; Grasset, F.; Duguet, E. *Journal of Materials Chemistry* 2004, *14*, 2161.
- [185] Kim, S.; Lim, Y. T.; Soltesz, E. G.; De Grand, A. M.; Lee, J.; Nakayama, A.; Parker, J. A.; Mihaljevic, T.; Laurence, R. G.; Dor, D. M.; Cohn, L. H.; Bawendi, M. G.; Frangioni, J. V. *Nature Biotechnology* 2004, *22*, 93.
- [186] Chesterfield, R. J.; McKeen, J. C.; Newman, C. R.; Ewbank, P. C.; da Silva, D. A.; Bredas, J. L.; Miller, L. L.; Mann, K. R.; Frisbie, C. D. *J. Phys. Chem. B* 2004, *108*, 19281.
- [187] Puntambekar, K.; Dong, J. P.; Haugstad, G.; Frisbie, C. D. *Advanced Functional Materials* 2006, *16*, 879.
- [188] Chang, P. C.; Lee, J.; Huang, D.; Subramanian, V.; Murphy, A. R.; Frechet, J. M. J. *Chemistry of Materials* 2004, *16*, 4783.
- [189] Merchant, K. A.; Thompson, D. E.; Fayer, M. D. *Physical Review A* 2002, *65*, 023817.
- [190] Berg, M. A.; Rector, K. D.; Fayer, M. D. *J. Chem. Phys.* 2000, *113*, 3233.
- [191] Schmidt, J. R.; Sundlass, N.; Skinner, J. L. *Chemical Physics Letters* 2003, *378*, 559.
- [192] Hu, Z. H.; Huang, X. H.; Annapureddy, H. V. R.; Margulis, C. J. *Journal of Physical Chemistry B* 2008, *112*, 7837.
- [193] Castner, E. W.; Wishart, J. F.; Shirota, H. *Accounts of Chemical Research* 2007, *40*, 1217.
- [194] Farrer, R. A.; Loughnane, B. J.; Deschenes, L. A.; Fourkas, J. T. *Journal of Chemical Physics* 1997, *106*, 6901.
- [195] Marti, J.; Padro, J. A.; Guardia, E. *Journal of Chemical Physics* 1996, *105*, 639.
- [196] Wells, N. P.; Blank, D. A. *Physical Review Letters* 2008, *100*, 086403.

- [197] Heimel, G.; Daghofer, M.; Gierschner, J.; List, E. J. W.; Grimsdale, A. C.; Mullen, K.; Beljonne, D.; Bredas, J. L.; Zojer, E. *Journal of Chemical Physics* 2005, *122*, 054501.
- [198] Karabunarliev, S.; Bittner, E. R.; Baumgarten, M. *Journal of Chemical Physics* 2001, *114*, 5863.
- [199] de Brito, A. N.; Silva, G. M. E. *International Journal of Quantum Chemistry* 2005, *103*, 604.
- [200] Macdiarmid, A. G.; Chiang, J. C.; Richter, A. F.; Epstein, A. J. *Synthetic Metals* 1987, *18*, 285.
- [201] Genies, E. M.; Boyle, A.; Lapkowski, M.; Tsintavis, C. *Synthetic Metals* 1990, *36*, 139.
- [202] Moon, H. S.; Park, J. K. *Synthetic Metals* 1998, *92*, 223.
- [203] Chiang, J. C.; Macdiarmid, A. G. *Synthetic Metals* 1986, *13*, 193.
- [204] Wang, Y. D.; Rubner, M. F. *Synthetic Metals* 1992, *47*, 255.
- [205] Lee, K.; Cho, S.; Park, S. H.; Heeger, A. J.; Lee, C. W.; Lee, S. H. *Nature* 2006, *441*, 65.
- [206] Dufour, B.; Rannou, P.; Fedorko, P.; Djurado, D.; Travers, J. P.; Pron, A. *Chemistry of Materials* 2001, *13*, 4032.
- [207] Jana, T.; Nandi, A. K. *Langmuir* 2000, *16*, 3141.
- [208] Jayakannan, M.; Annu, S.; Ramalekshmi, S. *Journal of Polymer Science Part B-Polymer Physics* 2005, *43*, 1321.
- [209] Winokur, M. J.; Guo, H. L.; Kaner, R. B. *Synthetic Metals* 2001, *119*, 403.
- [210] Luzny, W.; Banka, E. *Macromolecules* 2000, *33*, 425.
- [211] Lanzani, G.; Cerullo, G.; Brabec, C.; Sariciftci, N. S. *Physical Review Letters* 2003, *90*.
- [212] Sperling, J.; Nemeth, A.; Baum, P.; Sanda, F.; Riedle, E.; Kauffmann, H. F.; Mukamel, S.; Milota, F. *Chemical Physics* 2008, *349*, 244.
- [213] Schwartz, B. J.; Nguyen, T. Q.; Wu, J. J.; Tolbert, S. H. *Synth. Met.* 2001, *116*, 35.
- [214] Osterbacka, R.; An, C. P.; Jiang, X. M.; Vardeny, Z. V. *Synth. Met.* 2001, *116*, 317.
- [215] Kim, J.; Park, S.; Scherer, N. F. *Journal of Physical Chemistry B* 2008, *112*, 15576.
- [216] Kim, J.; Unterreiner, A. N.; Rane, S.; Park, S.; Jureller, J.; Book, L.; Liao, Y. H.; Scherer, N. F. *J. Phys. Chem. B* 2002, *106*, 12866.
- [217] Jana, T.; Chatterjee, J.; Nandi, A. K. *Langmuir* 2002, *18*, 5720.
- [218] Cheung, J. H.; Stockton, W. B.; Rubner, M. F. *Macromolecules* 1997, *30*, 2712.
- [219] Fonda, H. N.; Gilbert, J. V.; Cormier, R. A.; Sprague, J. R.; Kamioka, K.; Connolly, J. S. *Journal of Physical Chemistry* 1993, *97*, 7024.
- [220] Huang, W. S.; Macdiarmid, A. G. *Polymer* 1993, *34*, 1833.
- [221] Dominis, A. J.; Spinks, G. M.; Kane-Maguire, L. A. P.; Wallace, G. G. *Synthetic Metals* 2002, *129*, 165.
- [222] da Silva, J. E. P.; Temperini, M. L. A.; de Torresi, S. I. C. *Electrochimica Acta* 1999, *44*, 1887.

- [223] Zheng, W.; Min, Y.; MacDiarmid, A. G.; Angelopoulos, M.; Liao, Y. H.; Epstein, A. J. *Synthetic Metals* 1997, 84, 63.
- [224] Chaudhari, H. K.; Kelkar, D. S. *Polymer International* 1997, 42, 380.
- [225] Laridjani, M.; Pouget, J. P.; Scherr, E. M.; Macdiarmid, A. G.; Jozefowicz, M. E.; Epstein, A. J. *Macromolecules* 1992, 25, 4106.
- [226] Maron, J.; Winokur, M. J.; Mattes, B. R. *Macromolecules* 1995, 28, 4475.
- [227] Minto, C. D. G.; Vaughan, A. S. *Polymer* 1997, 38, 2683.
- [228] Castner, E. W.; Maroncelli, M. *Journal of Molecular Liquids* 1998, 77, 1.
- [229] Merchant, K. A.; Noid, W. G.; Akiyama, R.; Finkelstein, I. J.; Goun, A.; McClain, B. L.; Loring, R. F.; Fayer, M. D. *J. Am. Chem. Soc.* 2003, 125, 13804.
- [230] Williams, R. B.; Loring, R. F. *Chemical Physics* 2001, 266, 167.
- [231] Sauvajol, J. L.; Djurado, D.; Dianoux, A. J.; Fischer, J. E.; Scherr, E. M.; Macdiarmid, A. G. *Physical Review B* 1993, 47, 4959.
- [232] Zheng, G.; Clark, S. J.; Brand, S.; Abram, R. A. *Physical Review B* 2006, 74.
- [233] Athawale, A. A.; Chabukswar, V. V. *Journal of Applied Polymer Science* 2001, 79, 1994.
- [234] Banerji, S.; Peng, W.; Kim, Y. C.; Menegazzo, N.; Booksh, K. S. *Sensors and Actuators B-Chemical*, 147, 255.
- [235] Nicolas-Debarnot, D.; Poncin-Epaillard, F. *Analytica Chimica Acta* 2003, 475, 1.
- [236] Lubentsov, B. Z.; Timofeeva, O. N.; Khidekel, M. L. *Synthetic Metals* 1991, 45, 235.
- [237] Lubentsov, B.; Timofeeva, O.; Saratovskikh, S.; Krinichnyi, V.; Pelekh, A.; Dmitrenko, V.; Khidekel, M. *Synthetic Metals* 1992, 47, 187.
- [238] Pouget, J. P.; Jozefowicz, M. E.; Epstein, A. J.; Tang, X.; MacDiarmid, A. G. *Macromolecules* 1991, 24, 779.
- [239] Zeng, X. R.; Ko, T. M. *Polymer* 1998, 39, 1187.
- [240] Chen, S. A.; Lin, L. C. *Macromolecules* 1995, 28, 1239.
- [241] Quillard, S.; Louarn, G.; Lefrant, S.; Macdiarmid, A. G. *Physical Review B* 1994, 50, 12496.
- [242] McCall, R. P.; Roe, M. G.; Ginder, J. M.; Kusumoto, T.; Epstein, A. J.; Asturias, G. E.; Scherr, E. M.; Macdiarmid, A. G. *Synthetic Metals* 1989, 29, E433.
- [243] Colomban, P.; Folch, S.; Gruger, A. *Macromolecules* 1999, 32, 3080.
- [244] Kenkre, V. M.; Tokmakoff, A.; Fayer, M. D. *Journal of Chemical Physics* 1994, 101, 10618.
- [245] Tokmakoff, A.; Sauter, B.; Fayer, M. D. *Journal of Chemical Physics* 1994, 100, 9035.
- [246] Lizarraga, L.; Andrade, E. M.; Molina, F. V. *Electrochimica Acta* 2007, 53, 538.
- [247] Nyffenegger, R.; Ammann, E.; Siegenthaler, H.; Kotz, R.; Haas, O. *Electrochimica Acta* 1995, 40, 1411.